

**NONLINEAR OPTICAL PROPERTIES OF INDIUM
ARSENIDE WITH ULTRAFAST FEMTOSECOND RADIATION
AT MID-INFRARED WAVELENGTHS**

Mark Allan Corbett

**A Thesis Submitted for the Degree of PhD
at the
University of St Andrews**



2005

**Full metadata for this item is available in
St Andrews Research Repository
at:**

<http://research-repository.st-andrews.ac.uk/>

Please use this identifier to cite or link to this item:

<http://hdl.handle.net/10023/9726>

This item is protected by original copyright

Nonlinear optical properties of indium arsenide
with ultrafast femtosecond radiation
at mid-infrared wavelengths



University
of
St Andrews

A thesis presented in application for the
degree of Doctor of Philosophy
to the University of St Andrews by

Mark Allan Corbett

*J.F. Allen Physics Research Laboratories
School of Physics and Astronomy
University of St Andrews
Fife, Scotland*

March 2005



I, Mark Allan Corbett, hereby certify that this thesis, which is approximately 32,000 words in length, has been written by me, that it is the record of work carried out by me and that it has not been submitted in any previous application for a higher degree.

Date 27/04/05 Signature of candidate

I was admitted as a research student in January, 1997 and as a candidate for the degree of Doctor of Philosophy in January, 1997; the higher study for which this is a record was carried out in the University of St Andrews between 1997 and 2005.

Date 27/04/05 Signature of candidate

I hereby certify that the candidate has fulfilled the conditions of the Resolution and Regulations appropriate for the degree of Doctor of Philosophy in the University of St Andrews and that the candidate is qualified to submit this thesis in application for that degree.

Date 27/04/05 Signature of supervisor

In submitting this thesis to the University of St Andrews I understand that I am giving permission for it to be made available for use in accordance with the regulations of the University Library for the time being in force, subject to any copyright vested in the work not being affected thereby. I also understand that the title and abstract will be published, and that a copy of the work may be made and supplied to any *bona fide* library or research worker.

Date 27/04/05 Signature of candidate

Abstract

Nonlinear optical properties of the narrow band-gap semiconductor InAs have been studied using ultrashort femtosecond infrared pulses from a regeneratively amplified Ti:Sapphire pumped optical parametric amplifier (OPA) and difference frequency mixing (DFM) system.

Characterisation of the laser showed good stability with 1.5 μJ pulse energy in a Gaussian spatial distribution. Wavelength spectra were broad Gaussian distributions consistent with dispersion of ultrashort femtosecond duration pulses. Sub-200 fs pulse lengths were measured with a two-photon detector based autocorrelation.

The measured two-photon absorption coefficient agreed well with perturbation theory from 4 to 5.5 μm . At longer wavelengths the coefficient was smaller than expected. This was attributed to the broad, polychromatic wavelength and uncertainty in the pulse length.

No additional free carrier absorption was observed, even at very high irradiance. It is hypothesized that this was due to the carriers having insufficient time to undergo intra-band relaxation on the timescale of the pulses. Beam spreading and saturation effects may also have been occurring.

Nonlinear refraction was measured using the z-scan technique. A strong defocusing component dominated which was consistent with free carrier plasma effects. A weaker component was also observed that was defocusing at 4 μm and self-focusing at 5.5 μm .

This was in agreement with predictions of an ultrafast, n_2 contribution, corresponding to the real part of the third order susceptibility $\chi^{(3)}$.

Pump-probe measurements showed that the nonlinear refraction was instantaneous but the absorption had a build up time of ~ 100 ps. This was attributed to hot-phonon screened intra-band relaxation. Fitting of the pump-probe data produced Shockley-Read-Hall and Auger recombination lifetimes consistent with prior literature data.

Contents

Chapter 1 - Introduction.....	1
1.1 Aims of the work.....	1
1.2 Indium Arsenide.....	5
1.3 Outline of thesis	8
1.4 References	9
Chapter 2 - Femtosecond infrared OPA	12
2.1 Introduction.....	12
2.2 Seed laser	14
2.2.1 Modelocking	14
2.3 Chirped pulse regenerative amplification.....	17
2.3.1 Regenerative amplification	18
2.4 Optical parametric amplifier	20
2.5 Difference frequency mixing	25
2.6 Alternative ultrafast infrared sources	26
2.7 Summary of chapter	30
2.8 References	30
Chapter 3 - OPA characterisation	32
3.1 Introduction.....	32
3.2 Spatial profile.....	32
3.3 Output pulse energy	37
3.4 Attenuation of output energy.....	38
3.5 Output wavelength	42
3.6 Temporal pulse length.....	44
3.6.1 Introduction	44
3.6.2 Experimental arrangement	48
3.6.3 Results and discussion	52

3.7	Day to day operation	53
3.8	Summary of chapter	54
3.9	References.....	55
Chapter 4 - Two-photon absorption		57
4.1	Introduction.....	57
4.2	Multi-photon absorption theories	58
4.3	Two-photon absorption coefficient calculation for InAs	61
4.4	Measurement of 2PA coefficient.....	64
4.4.1	<i>Historical trends</i>	64
4.4.2	<i>Review of measurement in narrow bandgap materials</i>	66
4.5	Summary of chapter	68
4.6	References.....	68
Chapter 5 - Nonlinear absorption measurements		71
5.1	Two photon absorption	71
5.1.1	<i>Experimental set-up</i>	73
5.1.2	<i>Beam transmission model</i>	74
5.1.3	<i>Results and discussion</i>	76
5.1.4	<i>Temporal broadening</i>	79
5.2	Free carrier absorption	81
5.2.1	<i>Experimental arrangement</i>	82
5.2.2	<i>Results and discussion</i>	85
5.3	Summary of Chapter	90
5.4	References.....	90
Chapter 6 - Nonlinear refraction		92
6.1	Introduction.....	92
6.1.1	<i>Free carrier effects</i>	93
6.1.2	<i>Ultrafast effects</i>	96
6.2	Review of narrow-gap nonlinear refraction measurements.....	98

6.3	Simple experimental observation of nonlinear refraction	102
6.4	z-scan experiments	104
6.4.1	<i>Introduction</i>	104
6.4.2	<i>Thick samples</i>	107
6.4.3	<i>Experimental arrangement</i>	109
6.4.4	<i>Results and discussion</i>	109
6.4.5	<i>Free-carrier refractive cross-sections</i>	115
6.5	Summary of chapter	116
6.6	References	117
Chapter 7 - Pump-probe experiment.....		120
7.1	Introduction.....	120
7.2	Relaxation processes	121
7.3	Recombination processes	123
7.3.1	<i>Auger recombination</i>	123
7.3.2	<i>Shockley-Read-Hall recombination</i>	124
7.3.3	<i>Radiative recombination</i>	126
7.3.4	<i>Carrier rate equation</i>	127
7.4	Pump-probe measurements	129
7.4.1	<i>Experimental arrangement</i>	131
7.4.2	<i>Results and discussion</i>	133
7.5	Summary of chapter	139
7.6	References	139
Chapter 8 - Conclusions.....		143
8.1	Summary of thesis.....	143
8.2	Conclusions	145
8.3	Further work.....	146
8.4	References	148

Quotations

"Science is the best way of satisfying the curiosity of individuals at government expense"

- Lev Artsimovich, 1909-1973, Russian physicist

"By three methods we may learn wisdom: First, by reflection, which is noblest; second, by imitation, which is easiest; and third by experience, which is the bitterest"

- Confucius, 551-479 BC, Chinese philosopher

"The trees that are slow to grow bear the best fruit"

- Moliere, 1622-1673, French playwright

"Basic research is what I am doing when I don't know what I am doing."

- Werner von Braun, 1912-77, German-born American rocket engineer

"It is a good thing for an uneducated man to read books of quotations"

- Winston Churchill, 1874-1965

Acknowledgements

I am grateful to Dstl and its predecessor, DERA who supported my studentship, and to the UK MoD for funding the research.

At St Andrews thank you to my supervisor Prof. Alan Miller for his guidance and support through the research. The A-team Semiconductor Physics group past and present – Jonathan, Michael, Steve, Andy, Dawn, Jean-Francois, Julia, Alvaro, Mat and Charis, were always accommodating, helpful and entertaining during my sometimes infrequent visits to Bonnie Scotland. Arvydas Ruseckas willingly gave time on instruction and support with the OPA. Mary upstairs for keeping the department running.

At Malvern thank you to my internal supervisor Dr Richard Hollins for reviewing this thesis and providing useful comments and alternative ideas. Dr John Robertson was company as an office-mate and motivation by getting there first, by several years. Dr Phil Milsom really provided the foundation for this work and gave many useful discussions from the modelling perspective. Drs Ken McEwan and Dave James gave help and advice. Graham Balmer for his continued support within projects.

In the United States, Mitch Haeri at Raytheon for additional discussions and direction. Thank you to Paul Fleitz, Shekhar Guha and especially Leo Gonzalez for my time out there.

Massive thanks and my love to Susie for encouragement, motivation, fun times and putting up with my two year absence.

Finally, to my parents who have always supported and encouraged me.

Chapter 1 - Introduction

1.1 Aims of the work

Nonlinear optical properties of semiconductors have been studied extensively over the past four decades. Two-photon absorption in a semiconductor was first observed by Braunstein in 1964 [1] and measurements have continued over a wide range of materials and wavelengths [2-4]. Perturbation theory has been developed with good agreement to the experimental results [5,6]. Third order nonlinearities arising from conduction band non-parabolicity were observed by Patel in 1966 [7] and several other transitions have also been identified [8].

A key development was the observation of large refractive nonlinearities arising from the cumulative effect of optically generated free carrier populations. This was first reported at bandgap resonant wavelengths by Miller et al in 1978 [9]. The defocusing was attributed to band-filling where the injected carriers saturate the available conduction band states blocking band-to-band transitions. Similar results were achieved with two-photon excitation where the defocusing was also enhanced by the electron-hole plasma [10]. Operation at photon energies below the bandgap gives the advantages of inherently better transmission in the linear, or inactive state and wider waveband of response.

Characterisation of nonlinear effects has improved with the advent of better laser sources and experimental techniques. Ultrashort duration pulses from mode-locked lasers enable multi-photon absorption to be studied at high intensities and in isolation from other effects such as free carrier absorption and recombination. The widely adopted “z-scan” method has provided a standardised, sensitive procedure for the determination of nonlinear absorptive and refractive coefficients [11]. As shorter pulse lengths are achieved, the

resolution of pump-probe type measurements improves accordingly. Femtosecond timescale relaxation and recombination phenomena are now commonly reported allowing device performance to be optimised through tailoring of carrier dynamics [12].

The nonlinear optical properties shown by semiconductors have been applied to a variety of applications. Band-filling was quickly used to demonstrate hysteretic bistability and the optical equivalent of a transistor [13]. Saturable absorption has been used to achieve mode-locking and q-switched operation of lasers [14,15] and provides a useful technique for probing the evolution carrier distributions [16]. Nonlinear transmission and fluence limiting arises from two-photon absorption coupled with absorption and refraction by the photo-generated carriers [17,18]. This passive optical limiting can be used protect sensitive optical components from damage. The nonlinear response can equally be a hindrance, posing limitations on optical devices particularly at high operating intensities [19,20].

This thesis describes a study of two-photon induced nonlinear absorption (2PA) and accompanying refractive processes in the narrow-bandgap semiconductor material Indium Arsenide. The strength of the 2PA process will be shown to be inversely proportional to the bandgap cubed and hence greatly enhanced for narrow-gap materials. A further attraction is that the exciton binding energy decreases with narrower bandgap. The reduction of exciton effects simplifies the system.

The attraction of narrow-gap materials drives the laser requirements for 2PA to mid- and far-infrared wavelengths from 3 to 12 μm . Short, sub-picosecond pulse lengths are desirable because the multiphoton absorption process can be studied without additional complications from free-carrier absorption and recombination. The development of such short-pulse sources in the infrared has lagged behind the visible and near-infrared. Previous short pulse infrared sources have been highly specialised, large facilities such as free electron lasers, or with limited tuneability such as the optical-free-induction-decay

laser. Compact, reliable sources of ultrafast, femtosecond pulses with wide wavelength tuning range have recently become commercially available based on cascaded nonlinear optical generation processes.

The timeline below depicts the historical progress in both experimental and theoretical study of two-photon absorption and nonlinear transmission in semiconductors:

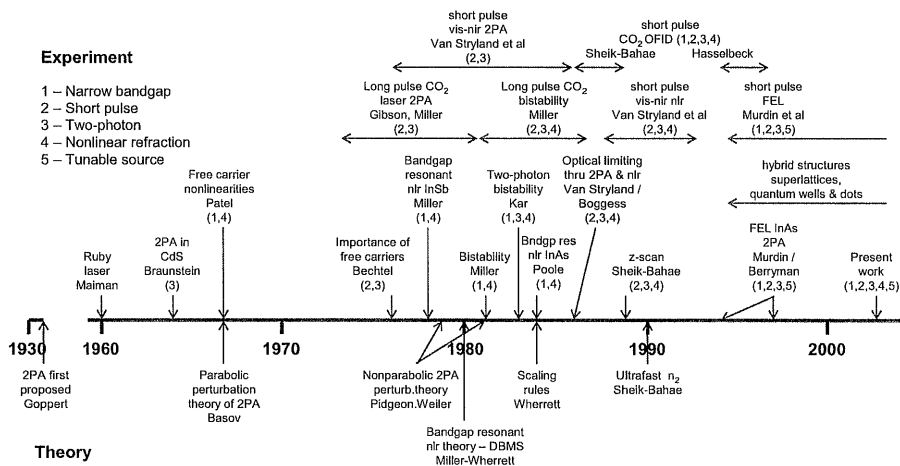


Figure 1-1: Timeline of two-photon absorption and nonlinear optics in semiconductors

The process of 2PA and refraction in a semiconductor is broken down in Figure 1-2:

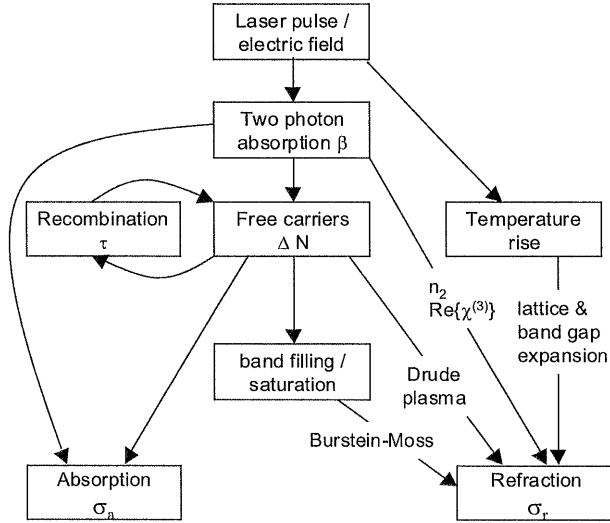


Figure 1-2: The processes involved in two-photon absorption and refraction

The aim of the work was to determine values for the following key parameters for InAs:

- two-photon absorption coefficient β
- free carrier absorption cross-section σ_a
- nonlinear refractive cross-section σ_r
- carrier recombination rate τ

A potentially suitable laser source for the measurements was identified in St. Andrews University ultrafast laser facility. An amplified Ti:Sapphire laser pumped an optical parametric amplifier (OPA). This generated signal and idler output with co-dependent wavelengths from 1.3 – 1.5 and 2.1 – 1.7 μm respectively. These pulses were combined in a AgGaS₂ crystal and difference frequency mixing (DFM) generated infrared output potentially tuneable from 3 to 12 μm . The ultrashort, ~ 100 fs pulses would enable the two-photon absorption coefficient to be isolated and measured unambiguously. From that

starting point the other parameters could be deduced by varying the experimental conditions.

1.2 Indium Arsenide

Indium arsenide is a well known semiconductor from the III-V group of compounds comprising binary mixtures of elements from groups IIIb (B, Al, Ga, In, Tl) and Vb (N, P, As, Sb, Bi). Other stable, useful III-V semiconductor alloys include GaP, GaAs, GaSb, InP, InSb and AlSb. The semiconductor properties of III-V compounds and their similarities to elemental group IV semiconductors such as Ge and Si were first demonstrated by Welker in 1952 [21].

InAs is used foremost as a photovoltaic infrared detector material typically sensitive to radiation wavelengths from 1 to 3 μm . Small thermo-electrically cooled packages have a wide range of applications from spectroscopy to laser warning receivers. More recently InAs has been applied to hybrid heterostructures such as quantum wells and dots. It shows good lattice matching to GaSb and AlSb but with large bandgap offset. Good affinity with metallic surface contacts and high mobility also make it suitable for high-speed electronics. The crystal structure of III-V semiconductors is described as zinc-blende after the compound ZnS [22]. An average of 4 valence electrons per atom gives a tetrahedral bonding structure. This in turn leads to a crystal lattice of two interpenetrating face-centred cubic cells as shown in Figure 1-3. Each unit cell contains two atoms. The arrangement is identical to the diamond lattice except that different elements occupy nearest neighbour points.

The light-hole (lh), heavy-hole (hh) bands, as characterised by their effective masses, are degenerate at the centre of the Brillouin zone. The spin orbit split off (so) band is a characteristic energy separation below them and has an intermediate effective mass. The single conduction band (cb) has the lowest effective mass and shows significant non-parabolicity for large k wave vectors. All the bands have two spin states.

The bandgap has been measured as a function of temperature resulting in the following empirical relation [25]:

$$E_g = 0.415 - 2.76 \times 10^{-4} \frac{T^2}{T + 83} \quad \text{Equation 1-1}$$

where the temperature, T , is in degrees K and the resultant energy gap in eV. This gives a bandgap of 0.35 eV at room temperature, equivalent to the photon energy at 3.5 μm . The gap increases to 0.4 eV (3.1 μm) at the liquid nitrogen temperature of 77 K. Good transmission and two-photon absorption should therefore be observed in room temperature InAs for wavelengths between 3.5 and 7 μm . In practice an absorption tail is present around the band-edge such that transmission only observed for wavelengths greater than $\sim 3.8 \mu\text{m}$.

The InAs samples used during the work described in this thesis were single crystals grown by the Czochralski technique and purchased from WaferTech (UK). The crystals were 1 mm thick, polished both sides and nominally undoped, though intrinsic carrier densities of $(1-3) \times 10^{16} \text{ cm}^{-3}$ were indicated. InAs has high refractive index of ~ 3.5 across the mid-infrared [24]. A plain sample therefore has a limited transmission of 50% due to Fresnel reflection losses. Anti-reflection coatings were applied to both surfaces by LaserOptik and the resultant improvement in transmission is shown in Figure 1-5.

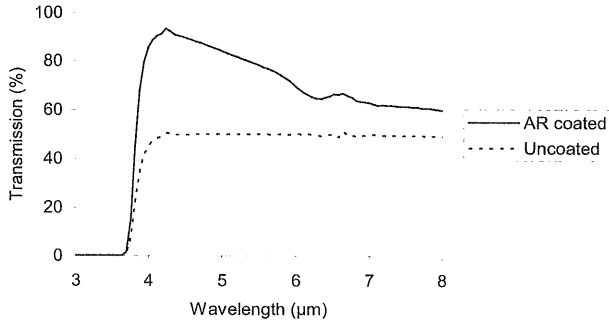


Figure 1-5: Transmission spectra of InAs samples

1.3 Outline of thesis

The OPA-DFM laser source is presented in more detail in Chapter 2. Each stage of the nonlinear generation process is covered. Details are also given of alternative short pulse infrared sources that have been previously used for nonlinear optical studies of narrow gap semiconductors.

Chapter 3 describes how the laser output from the OPA was characterised through a variety of techniques. This was the first use of the infrared DFM portion of the equipment. It is particularly important to measure the beam properly since the output intensity is critical in the subsequent deduction of nonlinear optical parameters. Working at infrared wavelengths requires alternative equipment and presents some different challenges to more standard measurements in the visible and near infrared.

Chapter 4 introduces two-photon absorption in narrow-gap semiconductors. Theoretical modelling of multi-photon absorption is reviewed and used to calculate the expected two-photon absorption coefficient for room temperature InAs. Prior measurements in narrow bandgap semiconductors are reviewed.

In Chapter 5 the nonlinear absorption of the OPA beam through InAs is studied. Refractive effects are eliminated by placing the sample close to the final detector ensuring that the entire transmitted beam is captured. An equation to describe beam propagation in the presence of two-photon absorption is derived. Two-photon absorption is then measured using an unfocused beam and compared to the theoretical predictions of the previous chapter. The beam is then focused and the nonlinear absorption measured at significantly higher intensities through the closed aperture z-scan technique.

Nonlinear refraction and phase shifts in the beam arising from the nonlinear processes are introduced in Chapter 6. Various mechanisms for nonlinear refraction are presented. Previous measurements of refraction in narrow-gap semiconductors are reviewed. The nonlinear refraction in InAs is studied using the z-scan technique.

In Chapter 7 the temporal behaviour of excess carriers generated by two-photon absorption is considered. Processes of carrier relaxation and recombination are described and lifetimes in InAs and related structures are reviewed. Time resolved nonlinear transmission in InAs is measured using a two-photon pump-probe technique. The observed behaviour arises from the combined effects of free carrier absorption and refraction. The carrier density rate equation is applied to the experimental results and the deduced lifetimes are compared with literature values.

Conclusions and suggestions for future research are presented in the final Chapter 8.

1.4 References

- 1 R Braunstein and N Ockman, "Optical Double-Photon Absorption in CdS," *Phys Rev* **134**, A499 (1964).
- 2 A. Miller, A. Johnston, J. Dempsey, J. Smith, C.R. Pidgeon, and G.D. Holah, "Two-photon absorption in InSb and $\text{Hg}_{1-x}\text{Cd}_x\text{Te}$," *J Phys C* **12**, 4839 (1979).
- 3 E.W. Van Stryland, H. Vanherzeele, M.A. Woodall, M.J. Soileau, A.L. Smirl, S. Guha, and Boggess T.F., "Two-photon absorption, nonlinear refraction, and optical limiting in semiconductors," *Opt Eng* **24**, 613 (1985).

- 4 J Burghoorn, VF Anderegg, TO Klaassen, WT Wenckebach, RJ Bakker, AFG van der Meer, D Oepts, and PW Amersfoot, "Free electron laser induced two-photon absorption in $\text{Hg}_{1-x}\text{Cd}_x\text{Te}$," *Appl Phys Lett* **61**, 2320 (1992).
- 5 MH Weiler, "Nonparabolicity and exciton effects in two-photon absorption in zincblende semiconductors," *Solid State Commun* **39**, 937 (1981).
- 6 B.S. Wherrett, "Scaling rules for multiphoton interband absorption in semiconductors," *J Opt Soc Am B* **1**, 67 (1984).
- 7 CKN Patel, R Slusher, and P Fluery, "Optical nonlinearities due to mobile carriers in semiconductors," *Phys Rev Lett* **17**, 1011 (1966).
- 8 SY Auyang and PA Wolff, "Free-carrier-induced third-order optical nonlinearities in semiconductors," *J Opt Soc Am B* **6**, 595 (1989).
- 9 DAB Miller, MH Mozolowski, A Miller, and SD Smith, "Nonlinear optical effects in InSb with a cw CO laser," *Opt Comm* **27** (1), 133 (1978).
- 10 AK Kar, JGH Mathew, SD Smith, B Davis, and W Prettl, "Optical bistability in InSb at room temperature with two-photon excitation," *Appl Phys Lett* **42**, 334 (1983).
- 11 M. Sheik-Bahae, A.A. Said, T.H. Wei, D.J. Hagan, and E.W. Van Stryland, "Sensitive measurement of optical nonlinearities using a single beam," *IEEE J Quant Elec* **26**, 760 (1989).
- 12 CM Ciesla, BN Murdin, CR Pidgeon, RA Stradling, CC Phillips, M Livingstone, I Galbraith, DA Jaroszynski, JGM Langerak C, PJP Tang, and MJ Pullin, "Suppression of auger recombination in arsenic-rich $\text{InAs}_{1-x}\text{Sb}_x$ strained layer superlattices," *J Appl Phys* **80**, 2994 (1996).
- 13 DAB Miller, SD Smith, and AM Johnston, "Optical bistability and signal amplification in a semiconductor crystal: applications of new low power nonlinear effects in InSb," *Appl Phys Lett* **35**, 658 (1979).
- 14 KL Vodopyanov, AV Lukashev, CC Phillips, and IT Ferguson, "Passive mode-locking and q-switching of an erbium 3 μm laser using thin InAs epilayers grown by molecular beam epitaxy," *Appl Phys Lett* **59**, 1991 (1991).
- 15 FX Kaetner, LR Brovelli, D Kopf, M Kamp, I Calasso, and U Keller, "Control of solid-state laser dynamics by semiconductor devices," *Opt Eng* **34**, 2024 (1995).
- 16 KL Vodopyanov, H Graener, CC Phillips, and TJ Tate, "Picosecond carrier dynamics and studies of Auger recombination processes in indium arsenide at room temperature," *Phys Rev B* **46**, 13194 (1992).
- 17 F Boggess, A.L. Smirl, S.C. Moss, I.W. Boyd, and E.W. Van Stryland, "Optical limiting in GaAs," *IEEE J Quant Elec* **QE-21**, 488 (1985).
- 18 E.W. Van Stryland, Y.Y. Wu, D.J. Hagan, M.J. Soileau, and K. Mansour, "Optical limiting with semiconductors," *J Opt Soc Am B* **5**, 1980 (1988).
- 19 KW DeLong, KB Rochford, and G Stegeman, "Effect of two-photon absorption on all-optical guided-wave devices," *Appl Phys Lett* **55**, 1823 (1989).
- 20 JU Kang, A Villeneuve, M. Sheik-Bahae, G Stegeman, K Al-hemyari, JS Aitchison, and C Ironside, "Limitation due to three-photon absorption on the useful spectral range for nonlinear optics in AlGaAs below half band gap," *Appl Phys Lett* **65**, 147 (1994).
- 21 H Welker, "On new semiconducting compounds," *Zeit fur Naturforsch* **7a** (1952).
- 22 O. Madelung, "Physics of III-V Compounds." (Wiley, 1964).
- 23 EO Kane, "Band structure of indium antimonide," *J Phys Chem Solids* **1**, 249 (1957).

- 24 MP Mikhailova, in *Handbook Series on Semiconductor Parameters (Ioffe Institute)*, edited by M Levinshstein, S Rumyantsev, and M Shur (World Scientific, 2000), Vol. 1 - Si, Ge, C (Diamond), GaAs, GaP, GaSb, InAs, InP, InSb, p. 147.
- 25 Z. M. Fang, K. Y. Ma, D. H. Jaw, R. M. Cohen, and G. B. Stringfellow, "Photoluminescence of InSb, InAs, and InAsSb grown by organometallic vapor phase epitaxy (w)," *J Appl Phys* **67**, 7034 (1990).

Chapter 2 - Femtosecond infrared OPA

2.1 Introduction

The ultrafast infrared pulses were generated by a commercially available Spectra-Physics optical parametric amplifier (OPA) in the St. Andrews ultrafast laser facility. The system comprised of a Hurricane regenerative amplified Ti:Sapphire laser pumping an OPA-800CF. This produced signal and idler output with co-dependent wavelengths from 1.3 – 1.5 and 2.1 – 1.7 μm respectively. These pulses were combined in a silver gallium sulphide (AgGaS_2) crystal where difference frequency mixing generated pulses of femtosecond duration infrared output potentially tuneable from 3 – 12 μm .

The generation process is depicted in the chart opposite. Each of the stages is described with more detail in the rest of the chapter.

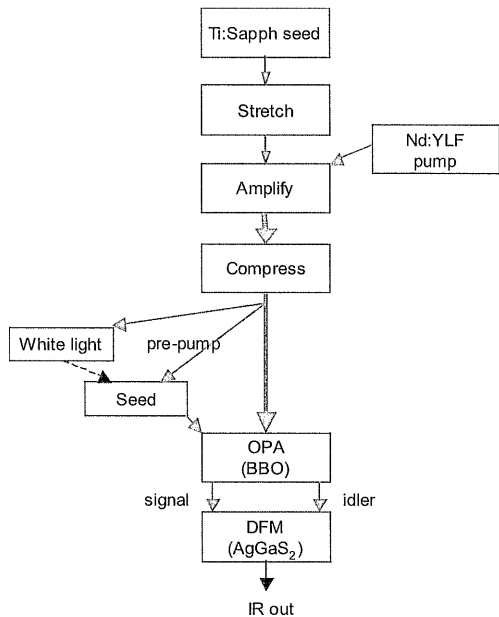


Figure 2-1: Flowchart depicting generation process and different stages of OPA

The overall physical layout of the system is shown in Figure 2-2.

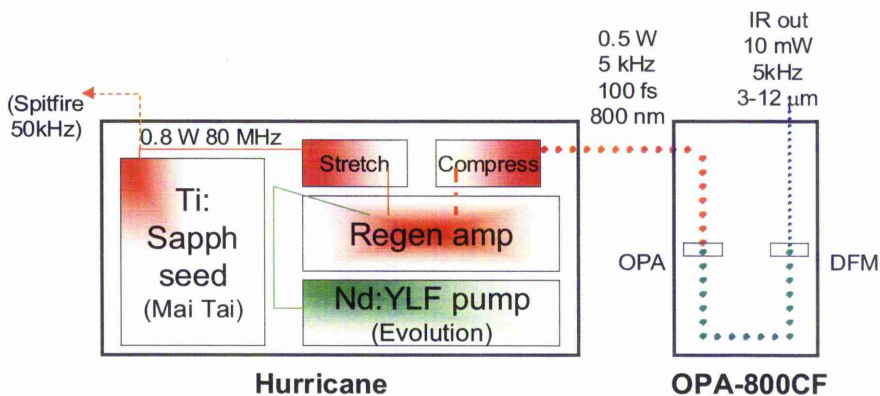


Figure 2-2: Layout of femtosecond infrared OPA system

There were several perceived benefits with this system for the measurement of nonlinear optical phenomena in narrow-gap semiconductors. The versatile tuning range of the infrared output was ideal for investigating the wavelength dependence of optical nonlinearities. The femtosecond pulses were capable of producing very high intensities in pulses of low integrated energy. This was important to minimise the effect of free carriers when measuring multiphoton absorption coefficients. The 5 kHz repetition rate meant a 200 μs interval between pulses which allowed the sample to completely recover between shots avoiding any possible cumulative effects.

The system was “compact”, easily accommodated on an optical table and could be run continuously throughout the day. A photograph of both units is shown below. Finally, although not completely turn-key, the operation and maintenance was less problematic than with a “home-built” system. The manufacturer gave good accompanying documentation and service support.

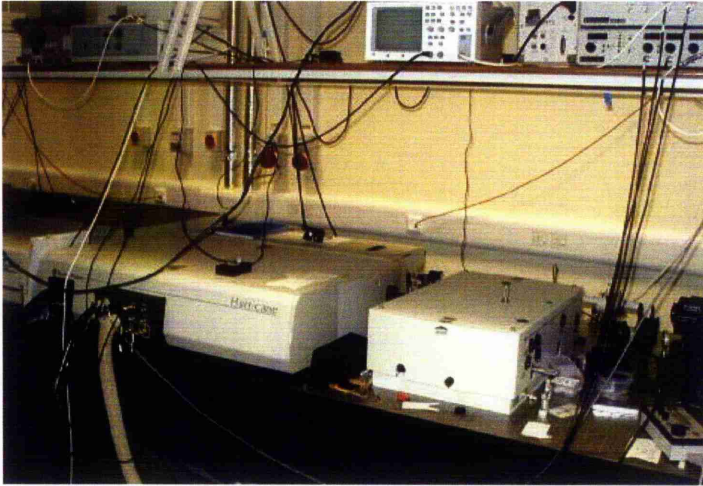


Figure 2-3: Photograph of Hurricane and OPA installation, Spitfire is visible to the rear

2.2 Seed laser

The starting point for the Hurricane source was a Mai Tai mode-locked Ti:Sapphire seed laser. The Mai Tai was in turn based on the Tsunami Ti:Sapphire cavity and Spectra-Physics Millennia pump laser [1].

The Millennia is a diode pumped neodymium yttrium vanadate (Nd:YVO₄) laser with intracavity frequency doubling giving several watts of cw output at 532 nm. This is used to pump a Ti³⁺ doped sapphire (Al₂O₃) crystal which exhibits broad absorption from 400 to 600 nm. Relaxation from the induced excited state back down to the ground state gives fluorescent emission in the near infrared from 670 to 1000 nm, creating a laser with very large potential bandwidth. The final wavelength is set using a prism sequence and slit.

2.2.1 Modelocking

Modelocking is a key technique for the production of ultra-short pulses. A laser cavity allows oscillation at discrete frequencies, or longitudinal modes, superimposed on the

overall gain profile of the laser medium. The frequency separation of the modes is determined by the length of the laser cavity:

$$\omega_{n+1} - \omega_n = \Delta\omega = \frac{2\pi}{T} = \frac{\pi c}{L} \quad \text{Equation 2-1}$$

where T is the cavity round trip time, L the cavity length and c the speed of light

Vibronic solid-state laser media typically exhibit broad gain profiles. Many modes exceed the lasing threshold and the emission has a broad bandwidth. If left free running the modes interfere with each other throughout the cavity giving random variation in output intensity. In mode-locking, the longitudinal modes are phase and amplitude correlated at the cavity round trip frequency so they interfere constructively.

The electric field at any arbitrary point in the cavity is given by:

$$E(t) = \sum_n E_n \exp[i((\omega_0 + n\Delta\omega)t + \phi_n)] \quad \text{Equation 2-2}$$

where ω_0 is a reference frequency, $\Delta\omega$ the separation of the longitudinal modes and ϕ_n the relative phase difference. Modelocking eliminates the phase difference. For N locked modes of equal amplitude, $E_n=1$, $\phi_n=0$ and Equation 2-2 becomes:

$$\begin{aligned} E(t) &= \sum_{-(N-1)/2}^{(N-1)/2} e^{i(\omega_0 + n\Delta\omega)t} & \text{Equation 2-3} \\ &= e^{i\omega_0 t} \frac{\sin(N\omega t / 2)}{\sin(\omega t / 2)} \end{aligned}$$

The output intensity is proportional to $E(t)E^*(t)$, thus:

$$I(t) \propto \frac{\sin^2(N\omega t / 2)}{\sin^2(\omega t / 2)} \quad \text{Equation 2-4}$$

This is plotted in Figure 2-4 and demonstrates a pulse train of high intensity mode-locked pulses. The repetition frequency is the inverse of cavity round trip time. The peak intensity is proportional to N^2 and the individual pulse duration proportional to T/N . A large number of modes are required to produce short, bright pulses. The number of modes is dependent

on the gain width making very short, intense pulses possible with vibronically broadened solid-state lasers.

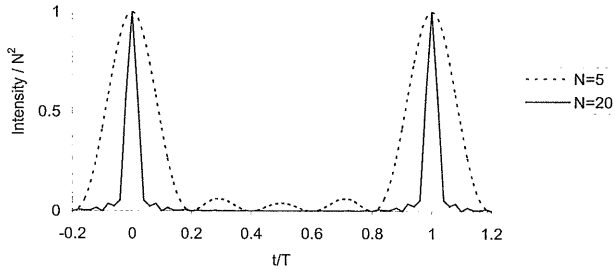


Figure 2-4: Mode-locked pulse trains for 5 and 20 modes

Several different techniques for modelocking have been devised. Active mode locking uses an external driving source linked to a phase, amplitude or gain modulator. Passive mode-locking relies on self-induced nonlinear optical effects such as absorption in a dye or refraction through Kerr-lensing.

The Tsunami laser uses an active intracavity acousto-optic modulator (AOM) to achieve mode-locked operation. The refractive index in a suitable optical crystal is varied by application of an rf frequency to generate a standing acoustic wave perpendicular to the optical path. The effect can be fast enough for the AOM to act as an optical shutter triggered to open at the same frequency as the pulse train. The long folded cavity length of ~ 1.9 m gives a roundtrip time of 12.5 ns and hence an output frequency of 80 MHz. A photodiode monitors the laser output providing a feedback mechanism to adjust the AOM driving frequency allowing for changes in cavity length.

The Mai Tai seed laser produced ~ 800 mW power with 100 fs duration pulses at a repetition frequency of 80 MHz. The wavelength was always set at 800 nm wavelength to maintain compatibility with the OPA.

2.3 Chirped pulse regenerative amplification

With ultra-short pulse durations, maximum achievable energy is limited by the onset of optical damage often initiated by nonlinear phenomena such as self-focusing. Chirped pulse amplification (CPA) is a technique originally developed for radar in which the pulse is first temporally stretched, or chirped, then amplified and finally recompressed. The peak intensity is greatly reduced within the amplification stage thus reducing the likelihood of damage.

CPA was first applied to laser amplification by Strickland and Maine [2,3] who amplified picosecond pulses from Nd:Glass lasers to terrawatt levels, approaching 1 J output. The pulse was stretched by propagation through a long (1.3 km) optical fibre. Self phase modulation and group velocity dispersion (GVD) within the fibre chirped the pulses from ~55 ps to 300 ps. Following amplification, recompression was achieved using the dispersive properties of a pair of diffraction gratings. The gratings can be arranged so that the blue light travels a shorter path, catching up with the red light and shortening the pulse length back to the original. This is demonstrated in Figure 2-5 where a double pass is used to give spatial reconstruction.

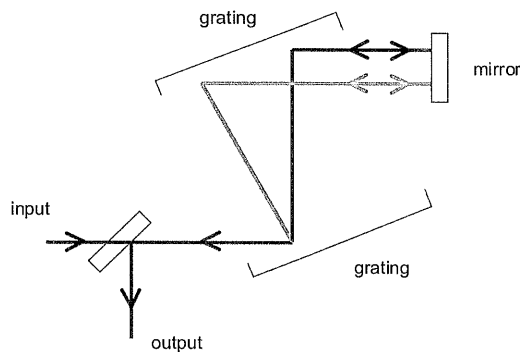


Figure 2-5: Simple design of grating based compressor

CPA starting with and returning to femtosecond pulse lengths was subsequently demonstrated with a solid-state Ti:Sapphire laser by Squier et al [4].

The Spectra-Physics Hurricane uses a single grating in each stretching and compression stage [5]. This provides the best performance since the dispersive characteristics of both stages can be conjugate matched. Spatial quality is maintained by using a configuration that gives four passes of each grating. The configuration for the stretcher is shown below.

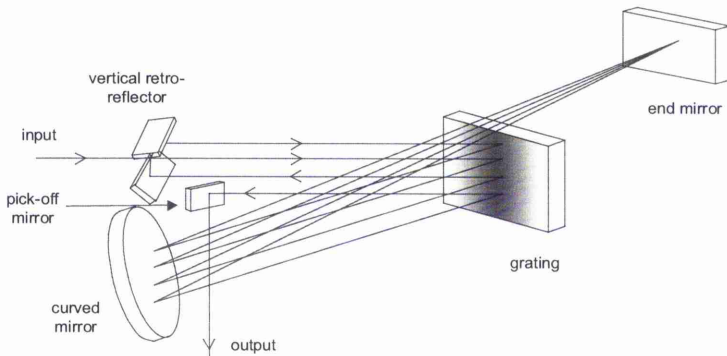


Figure 2-6: Pulse stretcher in the Hurricane

The curved mirror reverses the GVD so that the stretched beam is positively chirped. The compressor uses a similar folded four pass arrangement but without the curved mirror to reverse the chirp.

2.3.1 Regenerative amplification

In regenerative amplification, a cavity is used to pass the pulse several times through the amplifying medium. If a typical single pass gain is a modest $\times 4$, a series of only 10 consecutive passes is sufficient to amplify a pulse by a factor greater than 10^6 . The optical design of the amplifier cavity used in the Hurricane is shown below.

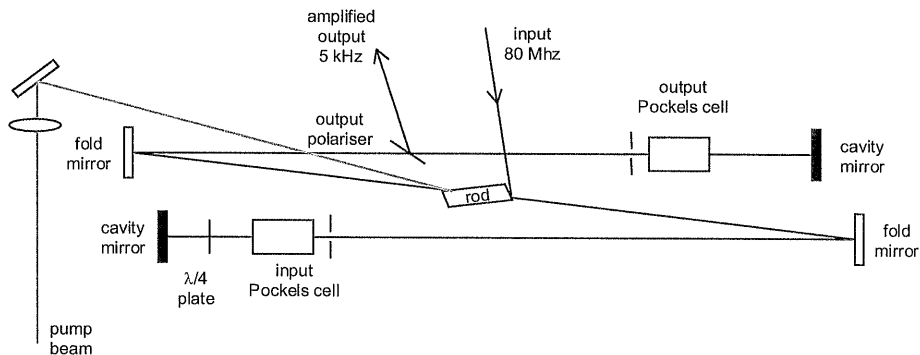


Figure 2-7: Hurricane regenerative amplifier cavity layout

The amplifier rod is another Ti:Sapphire crystal, pumped by a q-switched frequency-doubled Nd:YLF laser (Evolution). Control of pulses through the cavity is achieved through the use of Pockels cells. The Pockels effect alters the polarisation state of light through birefringence when voltage is applied to an optical crystal such as KDP.

Stretched pulses with vertical polarisation enter the cavity by reflection off the Brewster cut end of amplifier rod. With the lower input Pockels cell off, a double pass through the quarter wave-plate rotates the polarisation by 90° to horizontal. The pulses can then make a single round-trip of the cavity. On arrival back at the quarter wave-plate the polarisation is rotated again back to vertical. The pulse then exits by reflection off the end of the amplifier rod with little amplification.

A pulse selected for amplification is trapped in the cavity by the action of the input Pockels cell. The cell is activated with a quarter-wave voltage immediately after the first double pass of the wave-plate and Pockels cell. This negates the effect of wave-plate keeping the pulse polarisation horizontal so it can make several passes round the cavity undergoing amplification. The pulse is finally extracted by activating the top, output Pockels cell. A double pass with quarter-wave voltage rotates the polarisation to vertical and the pulse is reflected off the output Brewster polariser.

The input Pockels cell must be synchronised accurately with the mode-locked input pulses from the seed laser to ensure single pulses are cleanly accepted. The modelocking AOM is used as a reference. Fast driver electronics are required with adjustable delays of < 1ns. The output Pockels cell is delayed by ~70 ns with respect to the input and similar accuracy in timing is necessary.

Amplification of the initial seed laser output increased the individual seed pulse energy from 10 nJ at 80 MHz to 100 µJ at 5 kHz. With minimal change in pulse length this provided a large increase in pulse intensity. This in turn increased the efficiency of subsequent non-linear processes such as parametric amplification. The repetition rate was determined by the diode pumped Evolution pump laser. A higher frequency, 50 kHz flashlamp pumped capability was also available (Spitfire) but was not required for the measurements.

2.4 Optical parametric amplifier

Optical parametric generation and amplification splits a high photon energy pump beam into two lower energy beams, commonly referred to as the signal and idler. Energy is conserved such that:

$$\frac{1}{\lambda_{pump}} = \frac{1}{\lambda_{signal}} + \frac{1}{\lambda_{idler}} \quad \text{Equation 2-5}$$

The effect was first demonstrated in the optical domain by Giordmaine and Miller in 1965 who created resonant optical parametric oscillation in lithium niobate [6]. The underlying phenomena is the second order nonlinear response of the induced polarisation, $\chi^{(2)}$, and requires a non-centrosymmetric crystal. The opposite process is called sum frequency generation, of which second harmonic generation is a special case.

In the classical electric-dipole approximation, the induced dielectric polarisation of a medium is linearly related to the applied electric field:

$$\mathbf{P} = \varepsilon_0 \chi \mathbf{E} \quad \text{Equation 2-6}$$

where χ is the dielectric susceptibility and ε_0 the dielectric constant, or permittivity of free space. Under high electric fields, the linear relationship breaks down and further terms in \mathbf{P} are introduced through expanding the susceptibility with higher order powers of \mathbf{E} .

$$\mathbf{P} = \varepsilon_0 [\chi^{(1)} + \chi^{(2)}E + \chi^{(3)}E^2 \dots] \mathbf{E} \quad \text{Equation 2-7}$$

The physical origin is the oscillation of outer electrons of an atom in response to the electric field. An analogy can be made to the oscillation of a spring, where the linearity of Hooke's law breaks down at large extensions.

With a single beam present,

$$E(t) \propto E_0 \exp(i\omega t) + E_0^* \exp(-i\omega t) \quad \text{Equation 2-8}$$

The expansion of the E^2 arising from a non-zero $\chi^{(2)}$ leads to second harmonic generation terms:

$$E(t)^2 \propto E_0^2 \exp(2i\omega t) + E_0^{*2} \exp(-2i\omega t) + 2|E_0|^2 \quad \text{Equation 2-9}$$

When two beams of different frequency are present,

$$E(t) \propto E_1 \exp(i\omega_1 t) + E_1^* \exp(-i\omega_1 t) + E_2 \exp(i\omega_2 t) + E_2^* \exp(-i\omega_2 t) \quad \text{Equation 2-10}$$

The following terms and associated phenomena are observed:

$E(t)^2 \propto E_1^2 \exp(2i\omega_1 t) + E_1^{*2} \exp(-2i\omega_1 t)$	<i>second harmonic generation</i>
$E_2^2 \exp(2i\omega_2 t) + E_2^{*2} \exp(-2i\omega_2 t)$	<i>second harmonic generation</i>
$+2E_1 E_2 \exp(i[\omega_1 + \omega_2]t) + 2E_1^* E_2^* \exp(-i[\omega_1 + \omega_2]t)$	<i>sum frequency generation</i>
$+2E_1 E_2 \exp(i[\omega_1 - \omega_2]t) + 2E_1^* E_2^* \exp(-i[\omega_1 - \omega_2]t)$	<i>difference frequency generation</i>
$+2 E_1 ^2 + 2 E_2 ^2$	<i>dc rectification</i>

A phase matched condition equivalent to conservation of momentum is also required such that:

$$k_{pump} = k_{signal} + k_{idler} \quad \text{Equation 2-11}$$

where k represents the wavevectors of the different beams in the nonlinear crystal. One way to satisfy this is to use an optical crystal that exhibits birefringence where orthogonal polarisations experience different refractive indices. Tuning is then dependent on the crystal angle, which sets the phase matched condition. Alternatively materials can be periodically layered so that the nonlinear coefficient is modulated with twice coherence length to offset the accumulated phase mismatch. This is known as quasi-phase-matching. Periodically poled lithium niobate (PPLN) is probably the best known example of such a material [7]. The signal and idler wavelengths are then determined by the grating period with some dependence on crystal temperature.

The optical layout of the OPA-800C is shown in Figure 2-8 [8]. There are two conversion stages in the system. A seed beam is first produced by the white light and pre-pump paths through continuum seeded optical parametric generation (OPG). The seed is then combined collinear with the delayed main pump beam for the main optical parametric amplification (OPA).

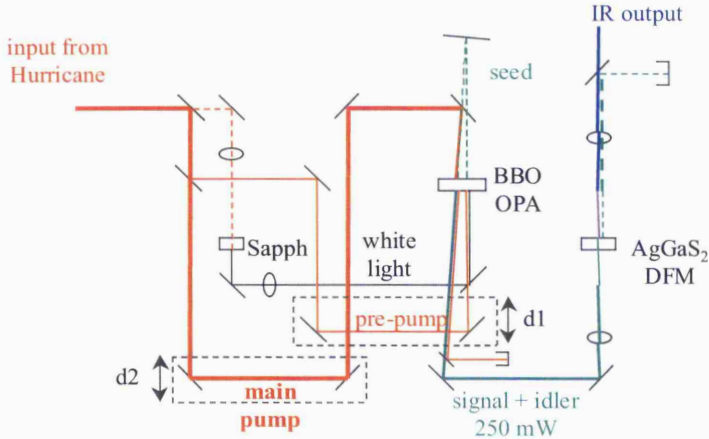


Figure 2-8: Optical layout of OPA

The nonlinear crystal is Beta-Barium Borate (BBO) in type II configuration with the signal of opposite polarisation to the pump and idler (o-e-o). The crystal thickness is kept to a few millimetres to minimise temporal walkoff.

A small portion of the input beam is split off and focused through a sapphire disc to produce a white light continuum. This provides a broadband excitation of the BBO crystal that is suitable for seed generation at any wavelength. White light generation is an extreme example of self-phase modulation. High beam intensities in suitable materials can create nonlinear refractive index changes, referred to as the optical Kerr effect. The index changes induce a linear chirp on the beam, broadening the wavelength spectrum. Femtosecond pulses are intense enough for the dispersion to cover a wide spectral range from 400 to 1400 nm, hence the description “white light”.

A second portion of the beam, the pre-pump, is delayed to arrive at the crystal at the same time as the white light. Together they generate a small amount of signal and idler at the wavelengths determined by the phase-matching angle of the BBO crystal. Only the idler portion is kept as the seed and then combined collinear through a dichroic mirror with the

main pump portion of the OPA input to pass through a different part of the same BBO crystal. The phase-matching angle is thus maintained between the seed OPG stage and main amplification stage. The depleted pump is separated off from signal and idler using another dichroic after which it can be dumped or used for further generation stages.

The theoretical tuning curve for the OPA signal and idler are shown in Figure 2-9, based on the fixed input wavelength of 800 nm from the Hurricane Ti:Sapphire pump laser. Crystal angles were determined using the SNLO software package from Sandia National Laboratories [9]. Typical conversion efficiency was ~50% giving around 200 mW signal and 50 mW idler. Output was maximised by optimising the overlap of the white light and pre-pump, then the resultant seed and main pump. Spatial overlap was adjusted through optical alignment of the seed and pump beam paths using the mirrors. Temporal overlap was achieved by adjusting the two delays stages, d1 and d2, which were designed to vary the path length without changing spatial alignment.

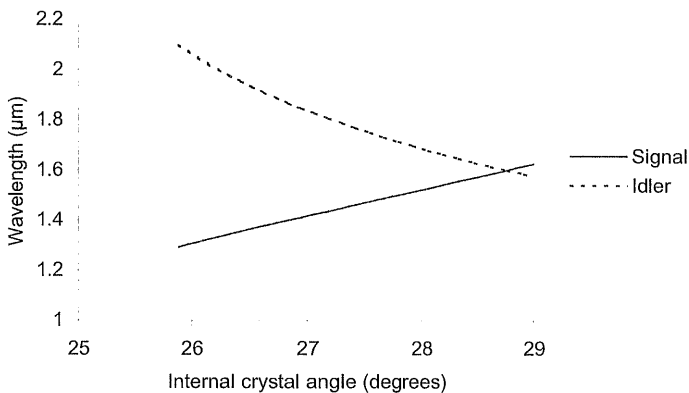


Figure 2-9: Tuning curves for OPA signal and idler

2.5 Difference frequency mixing

The final step was generation of infrared pulses through difference frequency mixing (DFM) in a suitable crystal. DFM uses the same fundamental $\chi^{(2)}$ mechanism as the OPA except that the output wavelength was determined by the difference in energy between the input wavelengths. Since the OPA pump wavelength was fixed at 800 nm, the chosen signal wavelength from the OPA pre-determined the infrared output wavelength:

$$\begin{aligned} \frac{1}{\lambda_{dfm}} &= \frac{1}{\lambda_{signal}(opa)} - \frac{1}{\lambda_{idler}(opa)} \\ &\equiv \frac{2}{\lambda_{signal}} - \frac{1}{\lambda_{pump}} \end{aligned} \quad \text{Equation 2-12}$$

The nonlinear crystal used was silver gallium sulphide (AgGaS_2). Although the nonlinear coefficient is slightly lower than other potential materials, good transmission from 550 nm to 12 μm makes AgGaS_2 a good choice for nonlinear infrared generation and frequency doubling of CO_2 laser pulses [10,11]. Phase matching was again achieved through angle tuning. DFM of femtosecond pulses in AgGaS_2 producing infrared output was briefly reported by de Barros and Becker [12] in 1991 who combined the output from a single cavity, two-colour Ti:Sapphire. The 780 and 855 nm wavelength pulses generated 9 μm radiation of low energy, ~ 0.03 pJ. Wider tuned DFM was seen by Hamm [13] who mixed the output from a regeneratively amplified Ti:Sapphire with the variable output from a dye laser, giving wavelengths from 4.5 to 11.5 μm .

The DFM tuning curve is shown below as a function of the available OPA signal wavelength and demonstrates the wide potential tuning range of the system:

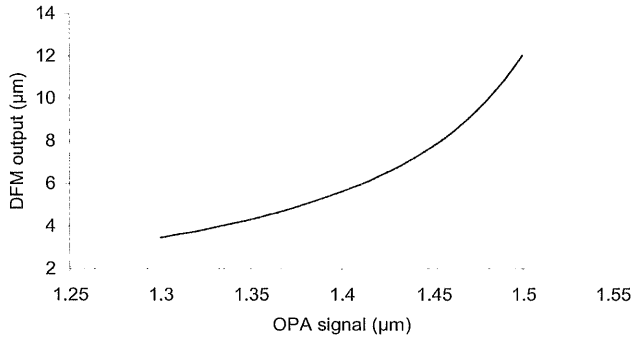


Figure 2-10: DFM tuning curve

Conversion was optimised by rotating the AgGaS₂ crystal to maximise the output energy. Efficiency was ~ 5% with typical output power of 10 mW, equivalent to 2 μJ per pulse. Some pulse stretching might be anticipated through the OPA and DFM processes though the pulse duration was still expected to be a few hundred femtoseconds.

2.6 Alternative ultrafast infrared sources

Several alternative optical sources with sub-nanosecond pulse duration have been used for measurement of nonlinear optical processes in narrow-gap semiconductors. Three are described here; Optical semiconductor switching, the Free Electron Laser and the Optical Free Induction Decay laser.

Optical switching uses fast modulation of the absorption and reflection coefficients of a wide bandgap semiconductor to shorten an infrared pulse [14]. A region of the semiconductor is excited by optical pumping at a wavelength above the bandgap, typically from a pulsed Nd:Glass laser at 1.064 μm. This creates a dense electron-hole plasma which abruptly increases the absorption and reflection at sub-bandgap infrared wavelengths. The technique has been demonstrated with Ge, Si and CdTe. A typical arrangement is shown below [15]:

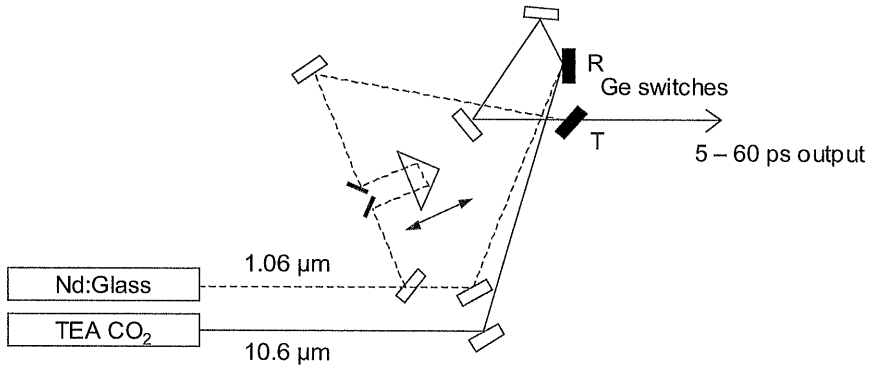


Figure 2-11: Schematic of optical semiconductor switched short pulse laser

The single-mode TEA (transverse-excitation-atmospheric) CO₂ laser produces pulses of ~200 ns duration. The 6 ps pulses from a Nd:Glass laser turn on the 'R' switch and turn off the 'T' switch which are Ge oriented at the Brewster angle for 10.6 μm. The output pulse length can therefore be adjusted through the variable delay.

Since the technique extracts a small portion of the started pulse, the output energy is low, sub μJ. Subsequent regenerative amplification has been used to increase pulse energies up to 15 mJ, equivalent to peak power of 10^{12} Wcm⁻² [16]. However such an arrangement is quite complicated. The output is still fixed to CO₂ wavelengths although it could in theory be extended to the mid-infrared with a suitable starting source, e.g. a DF laser.

In a Free Electron Laser (FEL) dipole radiation is emitted directly from oscillating electrons that are injected through an alternating magnetic field. A resonant optical cavity provides a feedback mechanism to induce coherent radiation emission and laser action. The output wavelength is dependent on the initial energy of the electrons and the physical design of the magnetic field generator, or undulator. In principle any wavelength can be produced, but operation in the infrared to far-infrared, up to 2000 μm, is most common since this allows convenient undulator period and electron energies.

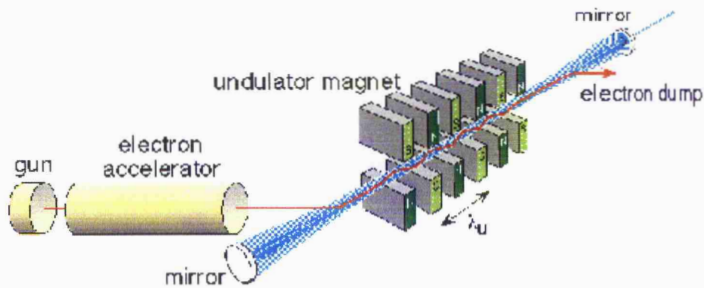


Figure 2-12: Free Electron Laser design (courtesy FELIX)

There are around 25 FELs currently operating around the world. Nonlinear optical measurements on narrow gap semiconductors have been performed at several of these [17-19]. The UK currently has a permanent station at the FELIX facility in the Netherlands primarily for semiconductor studies [20]. The output beam consists of $\sim 10 \mu\text{s}$ duration macropulses at a repetition rate of a few Hz. Within each macropulse are trains of micropulses of 1 – 10 ps duration separated at intervals of 1 or 40 ns. Micropulse energy is typically $\sim 10 \mu\text{J}$.

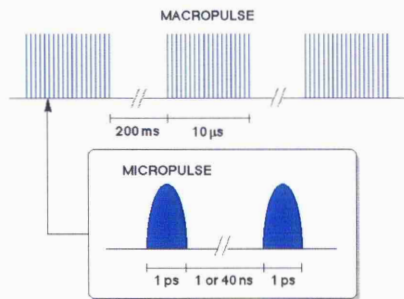


Figure 2-13: Temporal structure of typical Free Electron Laser output (courtesy FELIX)

The wide tuning range, picosecond pulse lengths and microjoule output energies make FELs attractive for narrow bandgap semiconductor studies. However they are large facilities with considerable infrastructure and associated operating costs, particularly when compared to the solid-state laser system used in this thesis. In addition, the separation of

the micropulses is not long enough to ensure complete free carrier recovery, so averaging effects and heating may occur.

The Optical Free Induction Decay (OFID) CO₂ laser was originally proposed and demonstrated by Yablonovich [21,22]. The output from a conventional, ns pulse duration single-mode TEA CO₂ laser is passed through a long path length gas cell containing hot CO₂ gas. Strong linear absorption within the hot gas can be regarded as destructive interference between the input field and the electric field from the induced polarisation of the gas molecules. Abrupt termination of the input beam results in continued emission from the polarised gas molecules with duration related to the relaxation time. Relaxation occurs through molecular collisions so the pulse length is mainly dependent on the gas pressure.

The rapid termination of the input beam is achieved with a plasma shutter based on laser induced breakdown in a gas [23]. Prior to the hot gas cell, the beam is focused tightly within a flowing stream of pure nitrogen gas. This prevents normal spontaneous gas breakdown arising from dust and other contaminants within unfiltered laboratory air. Breakdown is accurately controlled to occur at the peak of the pulse by triggering ultra-violet photoionisation from a dc spark-gap. The resultant plasma forms extremely rapidly with a velocity of $\sim 10^6$ ms⁻¹, attenuating the remaining beam through absorption, reflection and refraction.

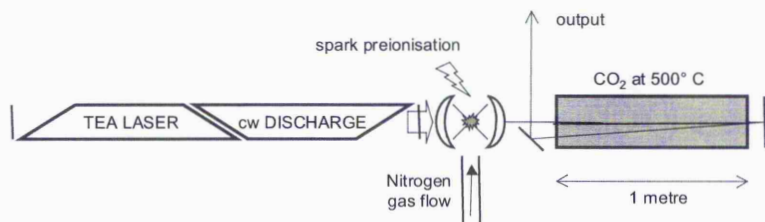


Figure 2-14: Schematic of optical free induction decay laser

Pulse lengths of between 20 and 200 ps have been observed by decreasing pressure in the absorber cell [24]. The lower limit is determined by the finite fall time of the plasma shutter. The upper limit is influenced by reduced absorption in the hot cell allowing more transmission of the original truncated TEA pre-pulse. Output energies of around 50 μJ are reported.

A CO_2 laser based OFID system has been used for non-linear optical measurements in narrow-gap semiconductors by Sheik-Bahae [25]. Since the generation mechanism of the pulses is a linear decay process, the output is generally described as predictable. However efficient performance and repeatability of the proceeding gas breakdown cell can be very dependent on contaminants. The OFID is also limited in output wavelength. Although the principle can in theory be extended to any wavelength, the breakdown cell must continue to operate and a suitable absorber gas must be identified. For mid-infrared generation a pulsed deuterium fluoride laser could be employed with output characteristics similar to a TEA CO_2 but at wavelengths from 3.6 – 4 μm .

2.7 Summary of chapter

In this chapter the ultrafast OPA-DFM system has been described. The design and underlying principles of each generation stage have been presented. A review of alternative, ultrafast infrared sources has been given.

2.8 References

- 1 Spectra-Physics, "Mai Tai - User's Manual, Rev F." (2002).
- 2 D Strickland and G Mourou, "Compression of amplified chirped optical pulses," *Opt Comm* **56**, 219 (1985).
- 3 P Maine, D Strickland, M Pessot, and G Mourou, "Generation of ultrahigh peak power pulses by chirped pulse amplification," *IEEE J. Quant. Elec.* **24**, 398 (1988).
- 4 J Squier, F Salin, G Mourou, and D Harter, "100-fs pulse generation and amplification in $\text{Ti:Al}_2\text{O}_3$," *Opt Lett* **16**, 324 (1991).
- 5 Spectra-Physics, "Hurricane - User's Manual, ver 1.00." (2000).

- 6 JA Giordmaine and RC Miller, "Tunable parametric oscillation in LiNbO₃ at optical frequencies," *Phys Rev Lett* **14**, 973 (1965).
- 7 LE Myers, RC Eckardt, MM Feer, and RC Byer, "Quasi-phase-matched optical parametric oscillators in bulk periodically poled LiNbO₃," *JOSA B* **12**, 2101 (1995).
- 8 Spectra-Physics, "OPA-800C - User's Manual, Rev D." (2001).
- 9 Arlee Smith, "SNLO - Software for the selection of nonlinear crystals," Sandia National Laboratories www.sandia.gov/imr1/XWEB1128/xxtal.htm (2004).
- 10 DC Hanna, VV Rampal, and RC Smith, "Tunable IR down-conversion in silver thiogallate," *Opt Comm* **8**, 151 (1973).
- 11 T Elsaesser, H Lobentzner, and A Seilmeier, "Generation of tunable picosecond pulses in the medium infrared by down-conversion in AgGaS₂," *Opt Comm* **52**, 355 (1985).
- 12 MRX de Barros and PC Becker, "Two-colour synchronously mode-locked femtosecond Ti:Sapphire laser," *Opt Lett* **18**, 631 (1993).
- 13 P Hamm, C Lauterwasser, and W Zinth, "Generation of tunable subpicosecond light pulses in the midinfrared between 4.5 and 11.5 μm ," *Opt Lett* **18**, 1943 (1993).
- 14 SA Jamison and A. Nurmikko, "Generation of picosecond pulses of variable duration at 10.6 μm ," *Appl Phys Lett* **33**, 598 (1978).
- 15 BD Schwartz, PM Fauchet, and A.V. Nurmikko, "Nonlinear transmission of picosecond 10.6 μm pulses in InSb," *Opt Lett* **5**, 371 (1980).
- 16 PB Corkum, "High power, sub-picosecond 10.6 μm pulse generation," *Opt Lett* **8**, 514 (1983).
- 17 J Burghoorn, VF Anderegg, TO Klaassen, WT Wenckebach, RJ Bakker, AFG van der Meer, D Oepts, and PW Amersfoort, "Free electron laser induced two-photon absorption in Hg_{1-x}Cd_xTe," *Appl Phys Lett* **61**, 2320 (1992).
- 18 BN Murdin, C Mervielle, AK Kar, C.R. Pidgeon, DA Jaroszynski, JM Ortega, R Prazeres, and F Glotin, "Infrared free-electron laser measurement of power limiting by two-photon absorption in InSb," *Opt Quant Electron* **25**, 171 (1993).
- 19 KW Berryman and CW Rella, "Nonlinear absorption in indium arsenide," *Phys Rev B* **55** (11), 7148 (1997).
- 20 D Oepts, AFG Van der Meer, and PW Amersfoort, "The free-electron-laser user facility FELIX," *Infrared Phys Technology* **36**, 297 (1995).
- 21 H.S. Kwok and E. Yablonovitch, "30-psec CO₂ laser pulses generated by optical free induction decay," *Appl. Phys. Lett.* **30**, 158 (1977).
- 22 E. Yablonovitch and J. Goldhar, "Short CO₂ laser pulse generation by optical free induction decay," *Appl. Phys. Lett.* **25**, 580 (1974).
- 23 I.P. Shkarofsky, "Review of gas-breakdown phenomena by high power lasers," *RCA Review* **35**, 48 (1974).
- 24 M. Sheik-Bahae and H.S. Kwok, "Characterization of a picosecond CO₂ laser system," *Appl Opt* **24**, 666 (1985).
- 25 M. Sheik-Bahae, T Rossi, and J Kwok, "Frequency dependence of the two-photon absorption coefficient in InSb: tunneling effects," *J Opt Soc Am B* **4**, 1964 (1987).

Chapter 3 - OPA characterisation

3.1 Introduction

Proper beam characterisation is a key requirement for laser-based optical measurements, however it is often neglected or badly reported. Knowledge of the peak intensity in the beam is essential for accurate deduction of nonlinear optical properties. This in turn requires accurate determination of the spatial distribution, pulse energy, output wavelength and pulse duration. During the present study, considerable time was spent measuring these parameters whilst also establishing confidence in using the system and gaining familiarity with its characteristics and stability.

The OPA-DFM was a remarkable piece of equipment that relied on some nine consecutive nonlinear optical generation processes. With so many steps it was with some trepidation and interest that the final infrared output of the system was measured and assessed to determine whether the beam quality and stability would be adequate for conducting nonlinear optical experiments.

3.2 Spatial profile

The spatial distribution of the OPA-DFM beam was viewed directly with an infrared sensitive camera and frame grabber. The camera was an Insight Series 80 pyroelectric vidicon. The vidicon tube was developed in the late 1970s and became the first widely available uncooled thermal imaging capability [1]. For many years it presented the best option for imaging infrared laser beams such as those from CO₂ lasers [2]. A tube schematic is shown in Figure 3-1.

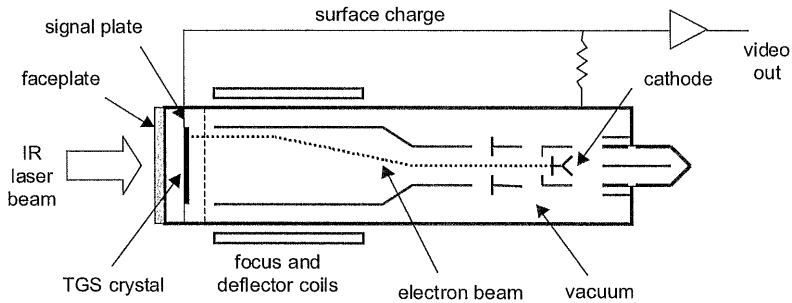


Figure 3-1: Schematic of pyroelectric vidicon tube

The faceplate is infrared transparent and allows the incident radiation to impinge on the pyroelectric element. The element is a single crystal disc of deuterated triglycine sulphate (TGS) around 20 μm thick and 20 mm in diameter. Absorption of the radiation causes local heating in the TGS that is converted to a surface charge through the pyroelectric effect. The charge is read out by systematically scanning, or rastering an electron beam across the crystal producing a temporally varying current off the surface plate. With reference to the electron scan pattern, this can be converted to a video signal representing the spatial distribution of the temperature across the detector element.

The vidicon has now been superseded by more advanced technologies such as microbolometers, which offer improved reliability and sensitivity [3]. However vidicons still offer some advantages for laser profiling. Firstly the ~ 18 mm diameter active area is large and can therefore measure bigger beams before resorting to indirect imaging. Secondly a ZnSe faceplate makes the vidicon tube sensitive to a broad wavelength range from 400 nm to beyond 12 μm . This is advantageous since it allows a visible laser, such as a HeNe or diode, to be aligned collinear with invisible IR. The HeNe can then be used to aid the safe setup of optical components.

The camera was interfaced to a Spiricon LBA300 PC card-based frame grabber and an accompanying software application. Beam sizes were computed real-time within the software based on a Gaussian fitting routine that produced full width $1/e^2$ diameters for both horizontal and vertical axes.

A typical profile for the OPA beam is shown in Figure 3-2 below. This was measured ~30 cm from the OPA output port with an attenuated incident power of ~100 μ W. The beam was deliberately offset to the left side to avoid a previously damaged region of reduced sensitivity located near the centre of the sensor.

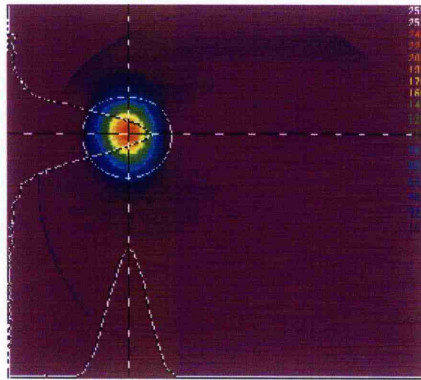


Figure 3-2: Spatial distribution of infrared OPA beam

The overall profile showed a good Gaussian, TEM_{00} appearance. The diameter was 3.3 mm, indicated by the superimposed aperture. The result gave confidence that the beam would be suitable for the planned non-linear optical measurements that often rely on favourable spatial distributions.

The accuracy of beam sizes determined by the software relied on correct spatial calibration of the camera pixel size. This was determined by mounting the camera on a calibrated x-y translation stage and using a 638 nm diode laser to produce a small spot. The camera was then translated a known distance and the new spot position recorded. This was

repeated to cover both the horizontal and vertical axes of the sensor. The resultant graph is shown below. Both data sets were linear with an average calibration factor of 33 $\mu\text{m}/\text{pixel}$ across the sensor.

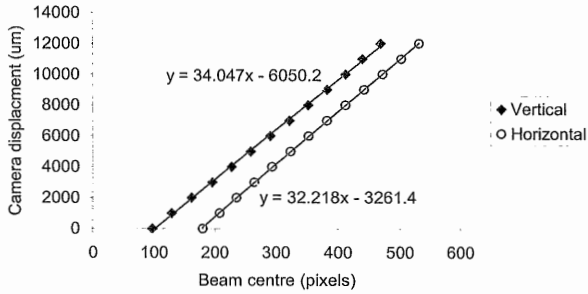


Figure 3-3: Spatial calibration of Insight vidicon camera

It was observed that the vidicon camera had a tendency to show a reduced background level along the horizontal lines where a beam was present. This was related to the rastering operation of the vidicon and possibly due to charge leakage along a line. The overall effect was to pinch horizontal spatial distributions so that they appeared smaller than the vertical. This is demonstrated in Figure 3-4 which first shows the uniform pedestal of the background as a blue colour. The same beam was sampled with the camera upright and physically rotated by 90 degrees. A dark band of purple is apparent in both profiles and the beam profile changes. If the camera were operating correctly both profiles would appear identical. It can be seen that the dark banding rotates with the camera and affects the observed beam diameter along the band. For this reason, whenever possible a beam diameter was measured with the camera upright for the vertical and at 90 degrees for the horizontal diameter.

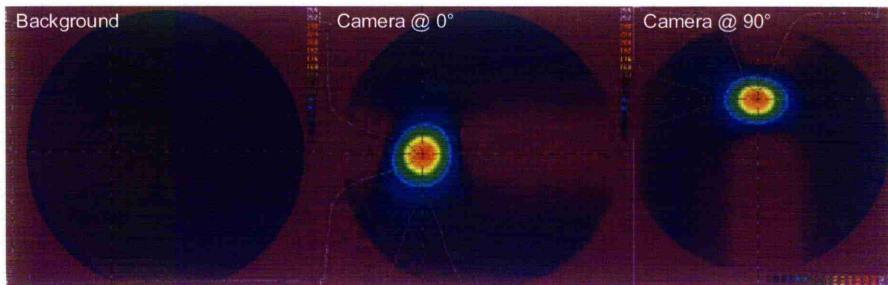


Figure 3-4: Uniform background and beam with camera rotation to show rastering artifacts with vidicon camera

An early problem encountered was the appearance of a spot obscuring part of the beam as shown in Figure 3-5. This was indicative of damage occurring to one of the optical components within the OPA. The source was eventually identified as a turning mirror after the final pass through nonlinear crystal. Initially the mirror was rotated to a new spot after which the beam quality improved and output power increased. However the damage re-occurred so the component was replaced with a gold-coated copper mirror which was more resilient with a higher damage threshold.

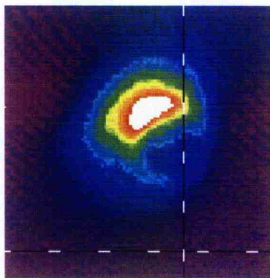


Figure 3-5: Beam profile arising from damaged optic in OPA

The output beam was dependent on the position of the final re-collimating lens after the DFM crystal. The beam size and collimation of the output was investigated as a function of the position of this lens and a best point determined at 295 mm from the DFM crystal. The divergence of the IR beam with this arrangement was measured to be ~ 1.5 mrad.

The beam size and divergence was found to increase with wavelength. This was due to dispersion in the final lens. At longer wavelengths the refractive index of BaF₂ was reduced and the lens no longer collimated the infrared output as effectively.

3.3 Output pulse energy

Output pulse energy was measured using Molelectron J3-09 pyroelectric detectors. Built-in battery driven amplifiers gave high responsivity (1.3 V/mJ) and good immunity to electrical RF noise pick-up. The 9 mm diameter elements were large enough to comfortably sample the entire beam and provide allowance for any refractive beam spreading. The chromed coating showed flat spectral response across the mid-infrared waveband. The temporal response of the pyroelectric was much too slow to resolve the temporal profile of the pulse but the amplitude of the detector output was a direct indication of the total energy absorbed from a pulse. High-speed circuitry enabled the J3-09 to measure pulse repetition frequencies up to 20 kHz, somewhat faster than most other pyroelectric detectors and making them suitable for use with the OPA. A typical oscilloscope signal is shown below:



Figure 3-6: Oscilloscope display of output from J3-09 pyroelectric energy detector
Timebase is 100 μ s per div, sensitivity is 1 mV per div

This was recorded with the full OPA output energy incident on the detector. The peak height of 1.3 mV implied pulse energy of $\sim 1 \mu$ J. With such small signals the oscilloscope

gave a limited range of resolvable energies. Instead Stanford Model 830 lock-in amplifiers were used with references synchronised to the OPA pockells cell driver at 5 kHz. This enabled much smaller signals to be discriminated. Pulse energies down to 1 nJ were detectable which was considerably below the normal range of a pyroelectric and standard energy meter. Calibration was also checked using a sensitive thermo-pile power meter type Spectra-Physics 407A. Dividing the power reading by the pulse repetition frequency of 5000 gave the pulse energy.

A calcium fluoride window was used as a beam splitter to reflect a small portion of the beam on to a reference J3-09. This provided a constant monitor of the OPA output and most results were normalised against this reference reading.

When greater sensitivity was required, liquid nitrogen-cooled, single-element HgCdTe photo-detectors from Cincinnati Electronics were used. Integrated electronics biased the detector elements and amplified the output. Two element sizes of 2x2mm and 100x100 μ m were used. The output was again monitored with a Stanford lock-in amplifier. Care was taken to keep the signal at levels where the amplifier response was still linear. This was typically at lock-in readings below 2 mV.

3.4 Attenuation of output energy

Ideal attenuation modulates the energy in a laser pulse without changing any other parameter. In practice this can be hard to achieve. Distortion of spatial, temporal or even spectral properties can be introduced unintentionally. A variety of attenuation techniques were explored for the OPA output.

Dielectric stack filters with nominally flat spectral response were found to work however the high index germanium substrates introduced significant variable beam walk-off. More successful was a Lasnix Model 102 step attenuator. Free standing wire grids are designed

to diffract a proportion of the beam out into higher order paths that are rejected [4]. The zeroth order propagates un-deviated and there is no polarisation sensitivity. A series of five grids were calibrated and found to give 50, 29, 11, 9.8 and 9.6 percent transmission steps, a combined optical density of ~ 4 . The wire grids were observed not to change any other parameter of the beam, however the fixed steps gave limited choice of attenuation values. It was decided to exploit the fixed horizontal polarisation output of the OPA to provide supplementary continuously variable attenuation.

The first attempt was with a ZnSe window variable attenuator (PAZ) manufactured by II-VI Inc. Two pairs of windows are mounted at opposing Brewster angles to cancel out beam walk off. As the unit is rotated the s and p orthogonal polarisation components of the incident beam are changed with respect to the windows. Only the p component, parallel to the plane of incidence, is transmitted and the transmission follows a $\cos^2\theta$ dependence. The measured transmission as a function of angle is shown below.

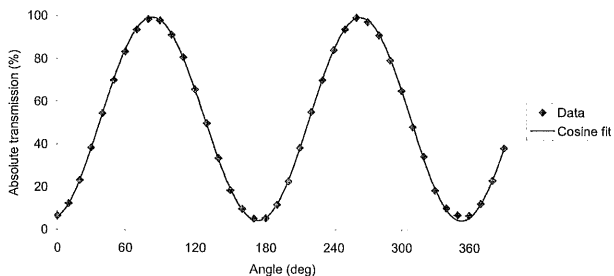


Figure 3-7: Transmission of ZnSe Brewster window attenuator

The maximum transmission was 100 % at 90° as expected from the horizontal polarisation output of the OPA. The minimum transmission was only 4 % which was higher than the manufacturer’s specification of 0.5 %. The device however was optimised for use at CO₂ laser wavelengths around 10 μm where the correct Brewster angle is around 67.4°.

Dispersion of the refractive index in the ZnSe meant that this angle was not optimal for wavelengths in the mid IR and as a consequence the extinction ratio suffered.

The Brewster window unit was found to offer repeatable variable attenuation complementary to the Lasnix step unit. However subsequent measurements revealed that the attenuator was also introducing undesirable additional changes into the beam. This was highlighted during two-photon absorption coefficient measurements made on indium arsenide. A limiting curve plot of input versus transmitted energy obtained with the variable attenuator is shown in Figure 3-8. Each colour series represents a fixed Lasnix step attenuation whilst the variable PAZ attenuator angle was varied from 80 to 140°.

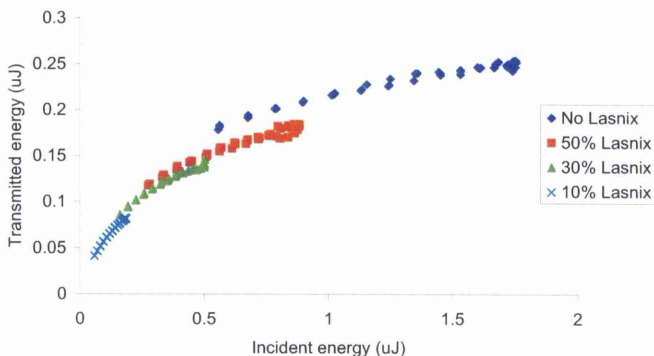


Figure 3-8: Anomalous InAs limiting curve observed with PAZ ZnSe attenuator

The data should have been on a smooth continuous curve. Instead the step pattern indicated the window attenuator was introducing a systematic error. It was deduced that the PAZ attenuator was changing the overall beam intensity in addition to the energy. The spatial profile of the transmitted beam was found to vary with angle and noticeable distortions were introduced especially near crossed polarisation angles, as shown in Figure 3-9.

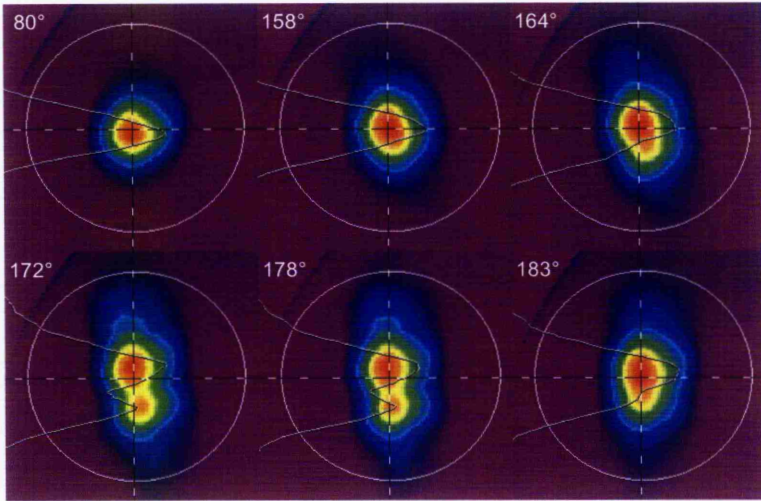


Figure 3-9: Beam distortion of PAZ ZnSe attenuator at various angles

An alternative polariser-attenuator, based on a free standing wire grid, was sourced from Infraspics. The pitch of the grid was considerably finer and more delicate than the Lasnix diffractive grids. The Infraspics polariser was found to give the desired variable attenuation and without any additional distortion of the beam. A typical calibration curve is shown in Figure 3-10. Disadvantages of this design were the intrinsic insertion loss of ~75% and tissue paper-like fragility of the fine grid.

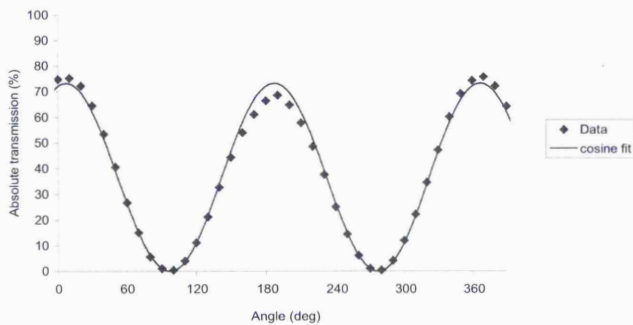


Figure 3-10: Transmission of wire grid polariser

3.5 Output wavelength

The wavelength of the infrared output of the OPA was measured using an Oriel 77250, $\frac{1}{8}$ m monochromator which was scanned manually. The experimental arrangement is shown in Figure 3-11. A calcium fluoride lens of 100 mm focal length focused the infrared beam through the 50 μm input slit of the monochromator. A similar slit was at the exit focal plane after which the 100 μm cooled HgCdTe detector was placed. The standard grating was replaced with a 150 lines/mm, times 8 multiplier grating giving an optimal wavelength scale of 2.5 to 8 μm . The monochromator was first calibrated by using the collinear 638 nm diode laser. Sufficient intensity was attainable in the visible diffracted beam off the grating for the 8th order to be observed out of the monochromator and confirmed to correspond to 638 nm on the wavelength scale.

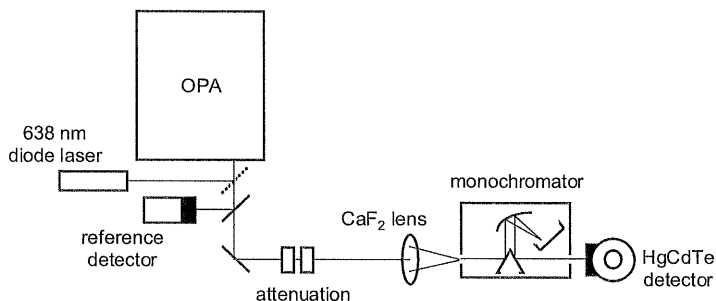


Figure 3-11: Experimental arrangement for wavelength measurement

A typical infrared spectrum from the OPA is shown in Figure 3-12. A least squares Gaussian fit gave a good fit with centre wavelength of 5 μm and full-width-half-maximum of 0.4 μm . This demonstrated one of the important characteristics of ultra-fast pulses in the infrared. The emission spectrum was very broad, and measurements could not be considered as monochromatic, single wavelength in the sense of a conventional laser source.

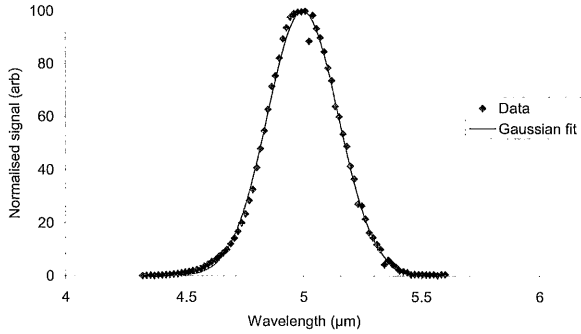


Figure 3-12: DFM output spectrum centred at 5 μm

A summary of output spectra and widths measured across the OPA tuning range is shown below:

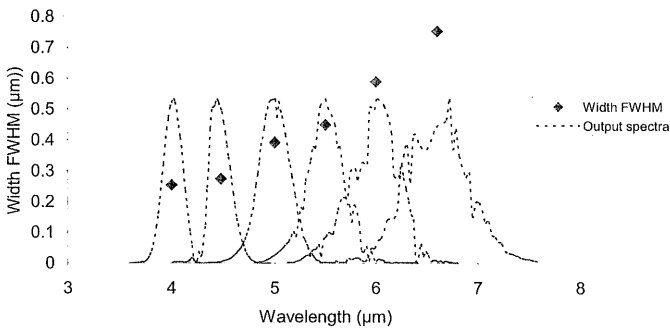


Figure 3-13: Summary of DFM output spectra and FWHM widths

The spectra deteriorated at wavelengths longer than 5 μm , with lower intensity at certain wavelengths. This was attributed to atmospheric water absorption and possibly some defects on the monochromator grating.

The OPA BBO and DFM AgGaS₂ crystal micrometer positions for each of the measured wavelengths are shown Figure 3-14.

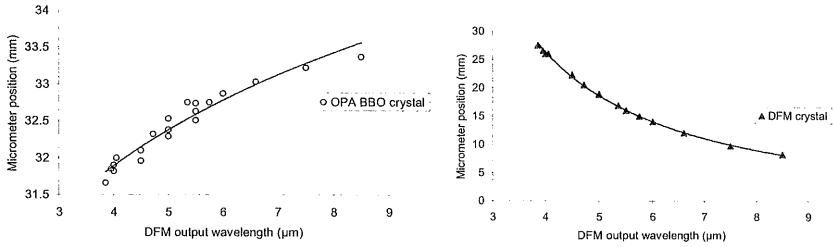


Figure 3-14: Crystal micrometer positions across tuning range of OPA

The BBO crystal data shows different positions for repeated measurements at the same wavelength. It was found that the crystal mount only held the crystal loosely and it was possible for the optic to move slightly if disturbed. The DFM crystal data shows better repeatability.

The micrometer positions were compared to the phase matched crystal angles predicted from the SNLO nonlinear crystal software package [5]. Linear fits showed similar calibration factors for both rotation stages.

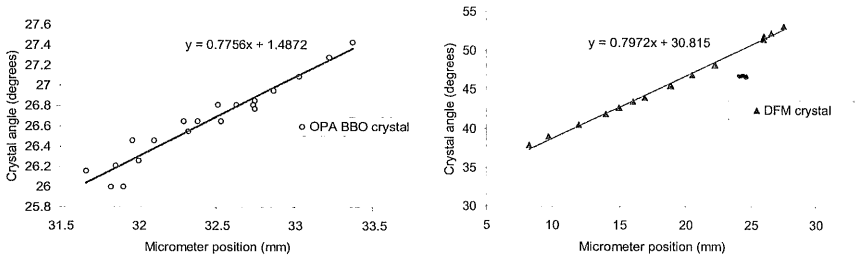


Figure 3-15: Calibration curves for OPA rotation stages

3.6 Temporal pulse length

3.6.1 Introduction

The infrared temporal pulse width was measured using a nonlinear autocorrelator arrangement based on a two-photon detector. Autocorrelation is a well-known technique

for measuring ultra-fast pico- or femto-second pulses that are too short to be resolved by conventional means. A small path difference is introduced between two pulses. The speed of the light travelling the extra path introduces a temporal delay between the pulses. A suitable nonlinear, typically intensity dependent process is then used where the detectable signal is strongly enhanced only when the pulses coincide. By varying the path length difference, the pulse overlap is changed and a correlation function is constructed that is a measure of the temporal width.

Early autocorrelation measurements used second harmonic generation (SHG) in suitable crystals to provide a second-order, intensity dependent signal for detection [6,7]. More recently, autocorrelation measurements using two-photon absorption in semiconductor devices have been demonstrated [8]. A single, inexpensive photodiode device can replace the more complicated arrangement required for SHG. The 2PA signal shows a quadratic dependence on the intensity of the incident light. For such a second-order process, the intensity autocorrelation function is given by:

$$G_2(\tau) = 1 + 2 \frac{\int_{-\infty}^{\infty} I(t)I(t-\tau)dt}{\int_{-\infty}^{\infty} I(t)^2 dt} \quad \text{Equation 3-1}$$

This function is plotted in Figure 3-16. Peak signal occurs at zero relative delay ($\tau=0$) and is normalised to three units. The background signal, where the pulses are completely separate ($\tau \gg t$) is one unit, giving an overall contrast ratio of 3:1. Any distortion or chirp present in the beam will reduce this contrast.

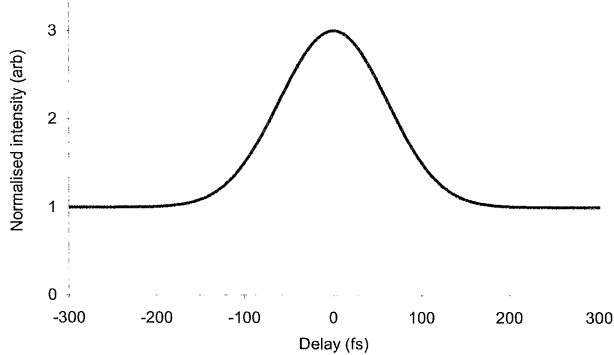


Figure 3-16: 2nd order intensity autocorrelation of a 100 fs (FWHM) Gaussian pulse at 5 μm wavelength

The autocorrelation width is measured at full width half maximum. This width is related to the actual pulse width by the expression:

$$\tau_{pulse} = \frac{\tau_{ac}}{k_f} \quad \text{Equation 3-2}$$

The k-factor is determined by the assumed pulse shape. For a transform-limited Gaussian pulse the bandwidth-duration product $\Delta\tau\Delta\nu=0.441$ and $k_f=1.414$.

If the bandwidth of the measurement is sufficiently high, a fringe pattern can be resolved that is a result of the interference of the two beams on the detector. This results in the second order interferometric autocorrelation function:

$$G_2(\tau) = \frac{\int_{-\infty}^{\infty} \left| \left\{ E(t)e^{i(\omega t + \phi)} + E(t-\tau)e^{i[\omega(t-\tau) + \phi(t-\tau)]} \right\}^2 \right|^2 dt}{2 \int_{-\infty}^{\infty} E(t)^4 dt} \quad \text{Equation 3-3}$$

The envelopes that define the upper and lower bounds of the fringes are given by:

$$G_{fu}(\tau) = \frac{\int_{-\infty}^{\infty} |E(t) + E(t-\tau)|^4 dt}{2 \int_{-\infty}^{\infty} E(t)^4 dt} \quad \text{and} \quad G_{fd}(\tau) = \frac{\int_{-\infty}^{\infty} |E(t) - E(t-\tau)|^4 dt}{2 \int_{-\infty}^{\infty} E(t)^4 dt}$$

The interferometric autocorrelation functions are shown in Figure 3-17:

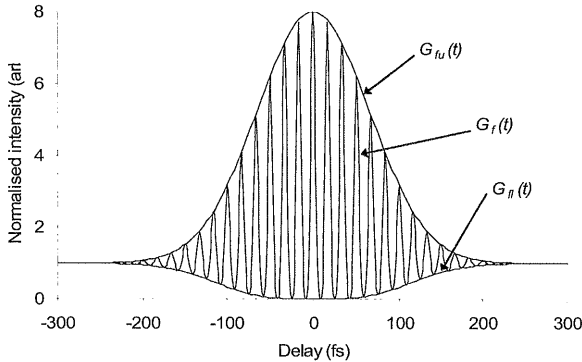


Figure 3-17: 2^{nd} order interferometric autocorrelation of 100 fs (FWHM) Gaussian pulse at $5 \mu\text{m}$

The function now depends quadratically on the electric field and the ideal contrast ratio increases to 8:1. Again, distortions or chirp present in the beam will affect the observed contrast. The interferometric autocorrelation width (FWHM) is related to the actual pulse width by a similar expression as before:

$$\tau_{pulse} = \frac{\tau_{ac}}{k_f} \quad \text{Equation 3-5}$$

For an assumed transform-limited Gaussian pulse the bandwidth-duration product is still $\Delta\tau\Delta\nu=0.441$ but now $k_f=1.697$.

Autocorrelation measurements of short infrared pulses have been reported using various techniques and materials. Kwok and Yablonovich used frequency doubling in GaAs to measure 32 ps pulses from a CO₂ OFID laser [9]. Thallium arsenic selenide (Tl₃AsSe) has also been used for the same purpose [10]. Free electron lasers have been characterised by

second harmonic generation in lithium niobate [11] and the photoconductivity signal arising from two-photon absorption in HgCdTe [12].

The use of a single, integrated two-photon detector for an infrared autocorrelation was reported by Zavriyev et al [13]. A GaAs/AlGaAs quantum well device was used with a normal cut-off of $\sim 8 \mu\text{m}$. Picosecond CO_2 laser pulses arising from free-carrier induced optical switching in CdTe and Si were characterised. Femtosecond mid-infrared pulses from a PPLN OPO were measured through the more straightforward use of a InAs photodiode detector by Burr et al [14]. Finally (and perhaps unexpectedly) Briggman et al observed multi-photon absorption signals from femtosecond mid- and far-infrared pulses with silicon CCD cameras and photodiodes [15]. The laser source was a Ti:Sapphire OPA-DFM virtually identical to the system used for this thesis. Detector signals were attributed to absorption processes involving between 3 and 7 photons. Both autocorrelation pulse lengths and beam profiles were presented.

3.6.2 Experimental arrangement

The experimental arrangement used for the autocorrelation is shown in Figure 3-18 and was based on a Michelson interferometer. A beam splitter, nominally 50:50, was used to split the beam into two paths. The paths were returned off corner cubes, recombined by the beam splitter then focused onto a detector. The position of one corner cube was adjustable and varied the delay between the two pulses. Careful alignment ensured that no beam walk-off occurred.

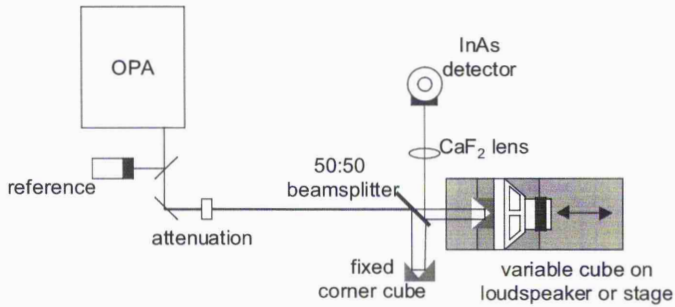


Figure 3-18: Two photon detector autocorrelator setup

For the OPA wavelengths from 4 – 6 μm a Judson J12 InAs detector was used similar to the femtosecond 5 μm OPO measurements by Burr et al [14]. At liquid nitrogen temperature the bandgap of InAs corresponds to 3.1 μm . The detector was used unbiased, operating purely as a diode junction. The signal from the detector was observed on an oscilloscope and is shown in below.

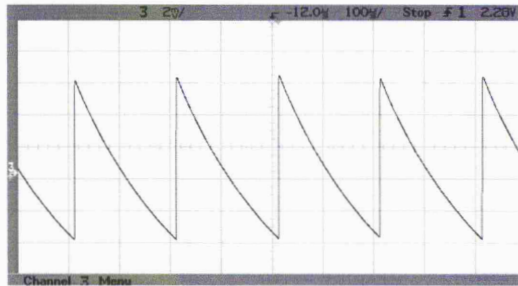


Figure 3-19: Two photon absorption signal from InAs detector on oscilloscope
Timebase is 100 μsec per div, sensitivity is 2 mV per div

The signal magnitude was measured as a function of incident energy and quadratic behaviour confirmed that it was a two-photon absorption induced signal as shown in Figure 3-20.

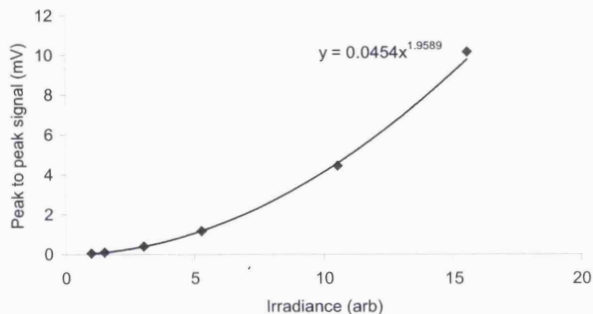


Figure 3-20: Quadratic two-photon signal from InAs detector

Two different techniques were used to change the path length in one arm of the interferometer. Initially the cube was mounted on a stepper motor translation stage. LabVIEW was used to control the stage position and to record lock-in amplifier signals via the IEEE bus. The stage was moved in 1 μm increments through the zero delay position building up an autocorrelation signal. The double path to and from the corner cube meant each 1 μm movement corresponded to a path length increment of 2 μm and a delay increase of 6.7 fs. Scans were repeated several times to build up an envelope. A typical result is shown in Figure 3-21 taken at 5 μm wavelength.

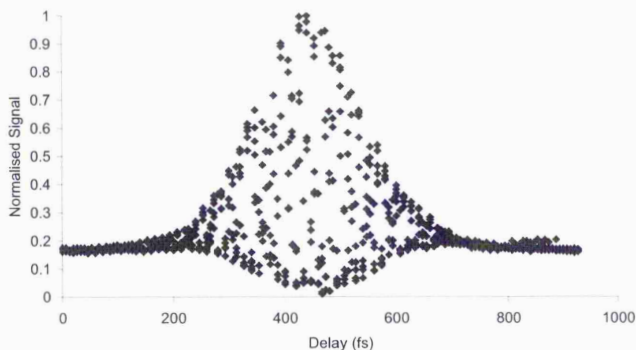
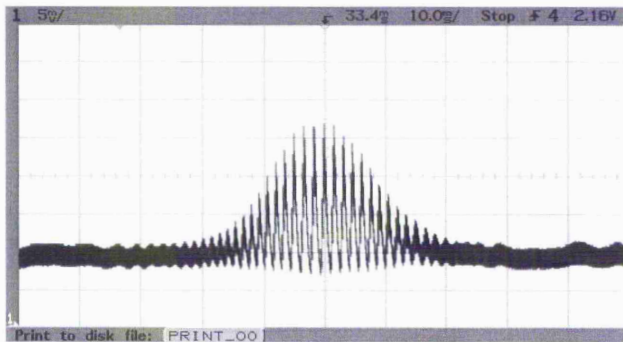


Figure 3-21: Stepper stage based autocorrelation at 5 μm

For an alternative technique the corner cube was mounted on an 8 inch loudspeaker cone. The speaker was driven by a rounded sawtooth waveform which provided constant velocity through the centre region. The InAs detector output was monitored on an oscilloscope triggered by a reference synchronised with the vibration frequency of the speaker. The autocorrelation was observed in real time on the oscilloscope. A typical trace is shown in below:



*Figure 3-22: Oscilloscope trace of loudspeaker based autocorrelation at $5 \mu\text{m}$
Timebase is 10 ms per div, sensitivity is 5 mV per div*

The thick noisy signal in the wings was caused by the temporal response of the detector. On a shorter timescale a sawtooth pattern was resolved which corresponded to each individual pulse as illustrated in Figure 3-19. The oscilloscope timescale was calibrated with respect to speaker displacement by translating one of the corner cubes through a known amount, typically $\sim 20 \mu\text{m}$. The whole autocorrelation envelope was observed to undergo a time shift on the oscilloscope. A scale factor ($\mu\text{m}/\text{msec}$) was calculated remembering that the path length was actually increased by a double pass of $40 \mu\text{m}$. This enabled the spatial width of the autocorrelation to be inferred. The temporal autocorrelation width (FWHM) was then the spatial width divided by the speed of light.

3.6.3 Results and discussion

Both arrangements produced interferometric autocorrelation traces as a result of the short pulses, spatially long wavelengths and fast detector. The fringe pattern was more clearly visible with the speaker technique. The stage technique built up an envelope as a result of the positional resolution of $\pm 0.5 \mu\text{m}$ on successive runs.

Good agreement was seen between the two techniques within experimental errors. The speaker method was adopted as the preferred technique since it gave quicker results by observing the pattern real time on the oscilloscope. The stage set-up took many minutes to step through the range and average each point several times. The observed contrast was around 6:1 for both techniques. This indicated the possibility of some chirp on the beam which was not unexpected given the multiple stages required for pulse generation. A summary of pulse lengths measured across the active range of the InAs detector is shown in Figure 3-23.

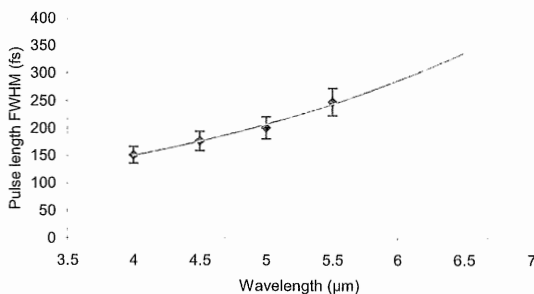


Figure 3-23: Infrared DFM pulses lengths measured across tuning range

Pulse measurement beyond $5.5 \mu\text{m}$ was not possible because the wavelength crossed the energy boundary for two-photon absorption in the cooled InAs. Attempts were made to measure beyond this limit with an InSb detector where the bandgap corresponded to $5.1 \mu\text{m}$, giving an upper bound of $10.2 \mu\text{m}$. Unfortunately these failed, principally because a

small amount of linear, single photon signal was being detected and dominating the detector output signal.

The bandwidth-pulse duration product, $\Delta\nu\Delta\tau$, gives a useful indication of the quality of the pulse. The frequency bandwidth was calculated through the output spectra using the relation:

$$\begin{aligned} \nu &= \frac{c}{\lambda} && \text{Equation 3-6} \\ \frac{d\nu}{d\lambda} &= \frac{-c}{\lambda^2} \\ |\Delta\nu| &= \frac{c}{\lambda^2} \Delta\lambda \end{aligned}$$

A summary of the output parameters and calculated bandwidth – pulse products across the measured wavelengths is shown in Table 3-1.

Centre wavelength μm	$\Delta\lambda$ (FWHM) μm	$\Delta\nu$ (FWHM) THz	$\Delta\tau$ (FWHM) fs	$\Delta\nu\Delta\tau$
4	0.25	4.7	151	0.70
4.5	0.28	4.2	177	0.75
5	0.42	5.0	201	1.0
5.5	0.46	4.5	248	1.1
6	0.57	4.7	285 *	1.3
6.5	0.78	5.5	335 *	1.8

Table 3-1: Measured parameters and bandwidth-pulse products
* denotes extrapolated pulse length

The bandwidth-pulse product at the lower wavelengths was around twice the Gaussian bandwidth limit of 0.441. This was considered respectable in view of the complexity of the generation process. The product increased at longer wavelengths indicating that more chirp was present. This probably arose from dispersion within the optics.

3.7 Day to day operation

The Mai Tai seed laser was turned on and allowed to warm up for ~45 mins. Control was through a computer interface and straightforward. At same time the Pockels cell driver unit was switched on. It was important to allow this unit to warm up since synchronised trigger

signals were required down to nanosecond resolution. Initial drift in the electronics was significant. The Evolution pump laser for the regenerative amplifier was also turned on.

After allowing warm-up time, the Hurricane amplifier was turned on and adjusted for proper operation. An internal photodiode enabled the build-up of an amplified pulse within the amplifier to be observed on an oscilloscope. The initial input signal was optimised, looking for a good signal pulse into the amplifier with no double pulses. The second delay was then adjusted for switching pulse out of amplifier, looking for clean cut-off at the peak pulse height. It was generally found that the Pockels cell driver settings could be left without adjustment from day to day provided proper warm-up time was given for the electronics.

Once satisfied with the operation of the amplified Ti:Sapphire laser, the output was allowed to pass into the OPA. The method here was to choose the desired infrared wavelength and set BBO and DFM crystal at the appropriate angles based on look-up tables from experience (section 3.5). The OPA output could be monitored by temporarily removing the AgGaS₂ crystal and placing a power meter in the beam. Combined signal and idler output was maximised by adjusting the temporal overlap using the delay stages, and the spatial overlap mainly by adjusting seed position through adjustment of the top seed mirror (see Figure 2-7). The AgGaS₂ crystal was reinserted and IR output maximised by adjusting crystal angle. The output wavelength was checked using monochromator.

The OPA output would typically remain stable for a few hours but periodic re-optimisation of the delays was necessary.

3.8 Summary of chapter

In this chapter the characterisation of the infrared output of the OPA-DFM system has been described. Key parameters required to specify the intensity distribution of a pulse have

been determined. Nonlinear optical properties could now be measured and the magnitude of corresponding coefficients correctly inferred.

Characterisation over a 4 to 7 μm tuning range showed that the output had good stability with a Gaussian spatial distribution around 3 mm in diameter. Typical pulse energy was 1.5 μJ and reliable modulation of the pulse energy was achieved. Output spectra showed broad Gaussian distributions with significant width, around 10% of the centre wavelength, consistent with femtosecond laser pulses incorporating some dispersion. A description of ultrashort pulse duration characterisation by autocorrelation has been given and a review of published infrared results presented. Sub-200 fs pulse lengths were measured with a two-photon detector based autocorrelator. The time-bandwidth product, $\Delta t \Delta \nu$, was calculated to be 0.7 at 4 μm , around twice the transform limit indicating some chirp was present.

3.9 References

- 1 R Watton, "Infrared Television: Thermal imaging with the pyroelectric vidicon," *Phys Technol* **11**, 62 (1980).
- 2 SH Mersch, JS Harris, and DL Mullen, "Imaging CO₂ high energy laser usec pulses with a pyroelectric vidicon camera," *Opt Eng* **20**, 464 (1981).
- 3 S Matthews, "Thermal imaging on the rise," *Laser Focus World*, March (2004).
- 4 F Keilman, "Precision broadband far-infrared attenuator," *SPIE 666* (Far-infrared Science and Technology), 213 (1986).
- 5 Arlee Smith, "SNLO - Software for the selection of nonlinear crystals," Sandia National Laboratories www.sandia.gov/imrl/XWEB1128/xxtal.htm (2004).
- 6 EP Ippen and CV Shank, in *Ultrashort Light Pulses*, edited by SL Shapiro (Springer-Verlag, New York, 1977).
- 7 JC Diels, JJ Fontaine, IC McMichael, and F Simoni, "Control and measurement of ultrashort pulse shapes (in amplitude and phase) with femtosecond accuracy," *Appl Opt* **24**, 1270 (1985).
- 8 Y Takagi, T Kobayashi, K Yoshihara, and S Imamura, "Multiple- and single-shot autocorrelator based on two-photon conductivity in semiconductors," *Opt Lett* **17**, 658 (1992).
- 9 H.S. Kwok and E. Yablonovitch, "30-psec CO₂ laser pulses generated by optical free induction decay," *Appl. Phys. Lett.* **30**, 158 (1977).
- 10 M.P. Hasselbeck, A.A. Said, E.W. Van Stryland, and M. Sheik-Bahae, "Three-photon absorption in InAs," *Opt Quantum Electron* **30**, 193 (1998).
- 11 S Benson, DAG Deacon, JN Eckstein, JMJ Madey, K Robinson, TI Smith, and R Taber, "Optical autocorrelation function of a 3.2 μm free-electron laser," *Phys Rev Lett* **48**, 1982 (1982).

- 12 J Burghoorn, VF Andereg, TO Klaassen, WT Wenckebach, RJ Bakker, AFG van der Meer, D Oepts, and PW Amersfoot, "Free electron laser induced two-photon absorption in $\text{Hg}_{1-x}\text{Cd}_x\text{Te}$," *Appl Phys Lett* **61**, 2320 (1992).
- 13 A Zavriyev, E Dupont, PB Corkum, HC Liu, and Z Biglov, "Direct autocorrelation measurements of mid-infrared picosecond pulses by quantum-well devices," *Opt Lett* **20**, 1886 (1995).
- 14 KC Burr, CL Tang, MA Arbore, and MM Fejer, "Broadly tunable mid-infrared femtosecond optical parametric oscillator using all solid-state-pumped periodically poled lithium niobate," *Opt Lett* **22**, 1458 (1997).
- 15 KA Briggman, LJ Richter, and JC Stephenson, "Imaging and autocorrelation of ultrafast infrared laser pulses in the 3 - 11 μm range with silicon CCD cameras and photodiodes," *Opt Lett* **26**, 238 (2001).

Chapter 4 - Two-photon absorption

4.1 Introduction

Multi-photon absorption in semiconductors is a well-documented phenomena in which free carriers may be generated through the absorption of intense radiation with photon energies less than the bandgap. Under conventional, low intensity illumination the low photon energy radiation is not absorbed and the material transmission is linear. At sufficiently high intensities the optical transmission becomes non-linear and dependent on the incident intensity.

Multi-photon absorption is explained by the quantum mechanical concept of energy-time uncertainty, $\Delta E \Delta t \geq \hbar/2$ [1]. There is a finite probability that a carrier can absorb an initial photon of energy less than the bandgap, E_g , and “borrow” some additional energy to enable occupation of an allowed state across the bandgap. This intermediate state is short-lived in accordance with the energy-time uncertainty. Under low intensity conditions, the carrier drops back down to the original energy level, re-emitting the photon. At high radiation intensities there can be sufficient probability that the carrier is able absorb a second photon whilst still in the intermediate state. For two-photon absorption this enables an excitation to be completed across the bandgap in which energy and momentum are conserved. Higher order multi-photon transitions are equally possible but require correspondingly higher intensities.

Multi-photon excitation was first proposed from a theoretical quantum mechanical perspective by Goppert-Mayer in 1931 [2]. Experimental confirmation had to wait for a suitable light source capable of providing the high optical intensities. The pulsed ruby laser was not realised until 1960 [3] and the first report of two-photon absorption in a $\text{CaF}_2:\text{Eu}^{2+}$

crystal followed just one year later [4]. The possibility of two-photon absorption across the bandgap in semiconductors was considered [5] and subsequently observed by Braunstein in 1964 [6]. A ruby laser was used to excite CdS (E_g 2.5eV) and evidence of two-photon absorption was deduced from radiative recombination emission at \sim 500 nm. Since then many materials have been studied at diverse laser wavelengths and pulse durations that have become available.

This thesis is primarily concerned with the narrow bandgap material InAs. The strength of the two-photon process will be shown to be inversely proportional to E_g^3 and hence greatly enhanced for this material. A further attraction is that the coulomb interaction of electrons and holes, or exciton binding energy, decreases with narrower bandgap. The reduction of exciton effects simplifies the process of 2PA in InAs.

4.2 Multi-photon absorption theories

The most successful theory for calculation of multi-photon absorption in semiconductors has been second-order perturbation theory. The transition rate between two bands, c and v , is given by a modified Fermi's golden rule which includes an intermediate state, i , which may be real or virtual:

$$W_2 = \frac{2\pi}{\hbar} \sum_{vc} \left| \sum_i \frac{\langle \psi_c | \hat{H}_{opt} | \psi_i \rangle \langle \psi_i | \hat{H}_{opt} | \psi_v \rangle}{E_{iv}(\mathbf{k}) - \hbar\omega} \right|^2 \delta(E_{cv}(\mathbf{k}) - 2\hbar\omega) \quad \text{Equation 4-1}$$

\hat{H}_{opt} is the optical interaction Hamiltonian given by $(e/mc)\mathbf{A}\cdot\hat{\mathbf{p}}$ and $\psi_{c,v}$ are the Bloch wavefunctions representing the conduction and valence bands that arise from the crystal periodicity. The summations are over all possible intermediate states, i , and also over all the transitions that are possible across the band structure.

Determination of the exact band structure of a semiconductor requires application of k,p theory to the crystal lattice and is beyond the scope of this review. As already described the band structure for zinc blende semiconductors such as InAs has been calculated by Kane [7]. The main features are shown in Figure 4-1.

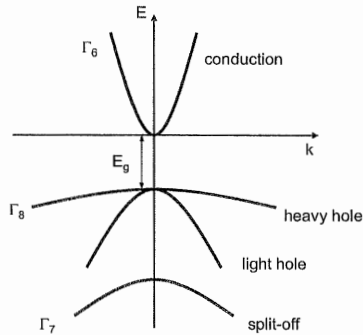


Figure 4-1 Kane band structure for zinc blende semiconductor

A calculation of the two-photon absorption coefficient in a semiconductor was first given by Braunstein and Ockman [6]. A simple band structure with parabolic valence and conduction bands was used with a higher level conduction band acting as the intermediate state. Transitions were taken between states with the same k , i.e. the photon momentum was neglected.

Basov also used perturbation theory to describe pumping of a GaAs semiconductor laser where improved sample penetration was envisaged through 2PA [8,9]. In a different approach, the virtual states were included within the original parabolic valence and conduction bands through intra-band transitions. Lee and Fan furthered this parabolic 2PA theory to include multiple degenerate valence bands and an exciton allowance [10]. Both intra- and inter-band transition processes were considered, as shown in Figure 4-2, giving a total of 12 possible final states including the spin of each band. Good agreement was

obtained with experimental results from nonlinear transmission measurements of several wide bandgap materials with a Nd:glass laser as well as InSb with a CO₂ laser.

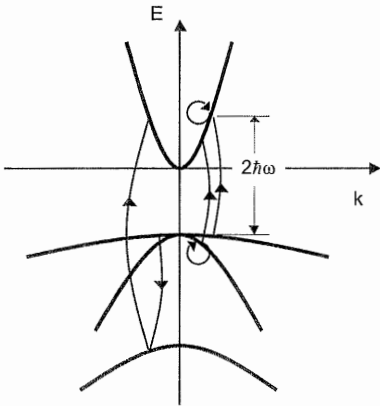


Figure 4-2 Idealised two-photon transitions for 4-band model

Universal curves taking band non-parabolicity into account were developed by Pidgeon [11,12] to give improvement particularly for two-photon energies significantly greater than the bandgap ($\hbar\omega \sim E_g$). Subsequent corrections and an exciton allowance were given by

Weiler [13]. Good agreement was shown with experimental results over a wide range of 2PA coefficients measured for bandgaps from 1.35 eV GaAs to 0.18 eV InSb.

Wherrett used a dimensional analysis with simplified parabolic band structure to produce a standard expression for multi-photon absorption coefficients [14]. The absolute values of the coefficients were not as accurate because of the assumptions. However it succeeded in predicting simple scaling rules to allow comparison of multi-photon absorption between different materials and predict the variation with wavelength. Van Stryland measured 2PA in several different semiconductors and showed that the scalings were valid though a uniform reduction by a factor of 1.6 gave best absolute agreement [15].

An alternative theory has been to adapt the ionisation theory of Keldysh [16], also known as tunnelling theory. The electron wave functions are dressed to take into account the oscillating electric field and crystal potential. This has had some success [17,18], however problems have been highlighted. The theory can not account for the relatively low light intensities under which non-linear absorption can be observed [19]. Also it is difficult to allow for valence band degeneracies [20].

A useful review by Nathan compares reported experimental values of multiphoton absorption with predictions from the different theories [21].

Finally a recent treatment by Hutchings used the full Kane band structure to calculate complete momentum matrix elements [20]. The elements were summed over all possible transitions between two conduction bands and six valance bands. This allowed polarisation dependencies and non-degenerate 2PA coefficients to be calculated where the two photons have different energies.

4.3 Two-photon absorption coefficient calculation for InAs

The two-photon absorption coefficient, β (cmW^{-1}), is defined such that the rate at which energy is absorbed per unit volume is βI^2 . The interband transition rate is therefore given by:

$$W_2 = \frac{\beta I^2}{2\hbar\omega} \quad \text{Equation 4-2}$$

Second order perturbation theory derives the following generic expression to describe the magnitude and spectral dependence of the coefficient:

$$\beta(\omega) = K \frac{\sqrt{E_p}}{n^2(\omega)E_g^3} F\left(\frac{2\hbar\omega}{E_g}\right) \quad \text{Equation 4-3}$$

where K is a material-independent constant of proportionality, n is the refractive index and E_g the material bandgap. E_p is the Kane energy, related to the Kane momentum parameter and is largely material independent with a constant value of ~ 21 eV for most direct gap semiconductors. F is a polynomial function of the photon energy relative to the bandgap and thus describes the wavelength dependence of the coefficient. The complexity of the F function depends on the detail that is used for the band structure.

It can be seen that the coefficient scales by the inverse of the bandgap cubed, E_g^{-3} . This drives the attractiveness of narrow bandgap materials such as InAs and InSb. Two photon absorption can be expected to be nearly 3 orders of magnitude stronger in these materials compared to wider gap, visible or near-infrared waveband semiconductors such as GaAs.

The K constant is given by:

$$K = \frac{4\pi e^4}{\sqrt{2m_e c^2}} = 0.0538 \text{ (cm eV}^{5/2}\text{MW}^{-1}) \quad \text{Equation 4-4}$$

where e is the electron charge, m_e electron mass and c the speed of light.

Three variations of the theory were compared for this study. Single parabolic valence and conduction bands result in a relatively straightforward form for the F function [14]:

$$F(x) = \frac{(2x-1)^{3/2}}{(2x)^5} \quad \text{Equation 4-5}$$

Van Stryland et al [22] also used this expression but changed the K constant to obtain a best fit to experimental values from ten different semiconductor samples. This indicated a value of $0.031 \text{ cm eV}^{5/2}\text{MW}^{-1}$, nearly half the theoretical value.

The non-parabolic bands theories of Pidgeon [11,12] and Weiler [13] make the F function more complex:

$$F(x) = 16\sqrt{\frac{2}{3}} \frac{(x-1)^{3/2}}{x^3} \left[\frac{\sqrt{x}}{\left(\frac{3}{2}x-1\right)^2} + \frac{6}{45} \frac{(x+1)^{3/2}}{x^5} \left(\frac{9}{16}x^4 + \frac{5}{2}x^2 + 6 \right) \right] \quad \text{Equation 4-6}$$

This is taking the case of a large split-off band, 0.4 eV for InAs [23] and neglecting exciton effects which are weak for narrow gap materials.

The wavelength dependence of the room temperature refractive index was incorporated using the following empirical formula [24]:

$$n(\lambda) = \sqrt{11.1 + \frac{0.71}{1-6.5\lambda^{-2}} + \frac{2.75}{1-2085\lambda^{-2}} - 6 \times 10^{-4} \lambda^2} \quad \text{Equation 4-7}$$

where the wavelength, λ , is in μm . This dependence is illustrated below in Figure 4-3:

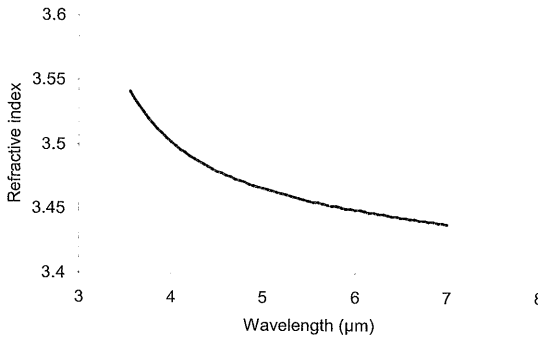


Figure 4-3 Wavelength dependence of refractive index in room temperature InAs

A comparison of the three variants of second order perturbation theory is shown below.

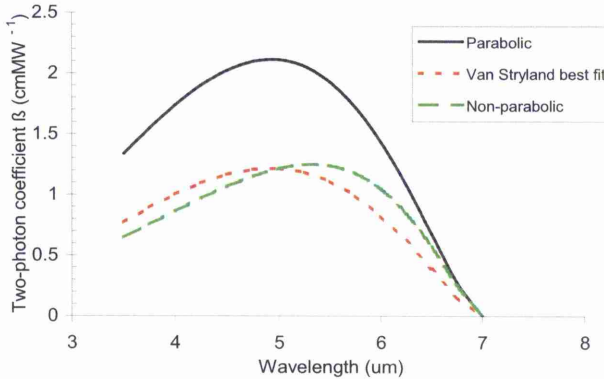


Figure 4-4 Theoretical wavelength dependence of two-photon absorption coefficient in InAs based on three variants of second order perturbation theory

All give a similar overall shape to the predicted coefficient, rising to a peak around 5 μm then declining rapidly as the photon energy approaches the two-photon threshold at 7 μm . The non-parabolic and best-fit parabolic curves lie close to each other, however the standard parabolic curve predicts a coefficient that is noticeably larger.

4.4 Measurement of 2PA coefficient

4.4.1 Historical trends

Reported values of two-photon absorption coefficients in semiconductors have followed a steadily decreasing trend over the decades. This is illustrated by Van Stryland et al [25] in which β measured for GaAs is illustrated to have fallen by nearly two orders of magnitude since the original reports in the mid 1960s. The refinement can be attributed to improved laser sources, better experimental techniques and more thorough understanding of effects such as carrier absorption and recombination.

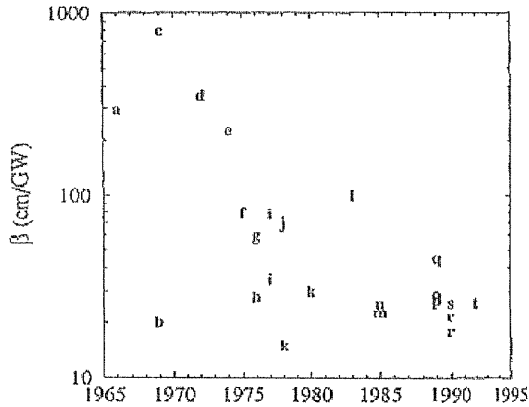


Figure 4-5: Two photon absorption coefficient of GaAs as function of year published

Letters denote references as given by Van Stryland et al [25]

Early measurements were typically made with relatively long, >1 ns duration lasers pulses. This remained the case with narrow bandgap materials where generation of ultra-short pulses at the required mid- to long-IR wavelengths has been more challenging. For longer pulse durations the generated free carrier effects such as absorption and recombination become significant.

The importance of laser pulse length was highlighted by Bechtel and Smith [26] who presented the following expression for a critical intensity at which absorption due to excited carriers becomes comparable to the two-photon absorption:

$$I_{crit} \approx \frac{2\hbar\omega}{\sigma_h\tau(1-R)} \quad \text{Equation 4-8}$$

where $\hbar\omega$ is the photon energy, σ_h is the carrier absorption cross section, typically dominated by holes, τ the HWe^{-1}M of the laser pulse and R the surface reflectivity. Two-photon absorption depends on the intensity whereas the generated carrier density depends on the total energy, or integrated intensity, in the pulse. A shorter pulse generates higher

intensity with lower energy and should experience more 2PA with less free carrier absorption.

Deduction of an accurate two-photon absorption coefficient is highly dependent on accurately measuring the intensity distribution of the pulse. Measurement techniques have improved over time both with better single mode output of lasers and devices such as direct viewing cameras and frame grabbers to measure beam sizes.

Finally, the non-linear refractive effects associated with the two-photon process were not identified until the late 1970s. The possibility of beam spreading and energy missing the collecting detector could lead to the deduction of erroneously high absorption coefficients. Often there is insufficient experimental description in papers to determine whether this might have been occurring.

4.4.2 Review of measurement in narrow bandgap materials

The earliest report of two-photon absorption in a narrow bandgap semiconductor was by Patel in 1966 [27]. Emission of recombination radiation was observed in PbTe corresponding to the bandgap of $6.5 \mu\text{m}$ when illuminated by sufficiently intense radiation from a pulsed $10.6 \mu\text{m}$ CO_2 laser. Similar radiation was observed with an InSb crystal but the possibility of second harmonic generation (SHG) and subsequent absorption could not be ruled out. The measured carrier production rate was compared with Keldysh tunnelling theory and gave order-of-magnitude agreement.

Subsequent measurements concentrated on InSb for quite a time since it was a readily available material of good quality that benefited from characterisation and development efforts in the infrared detector field. The bandgap of InSb was matched conveniently for 2PA with the CO_2 laser which typically produced long duration pulses, $\sim 100 \text{ ns}$ or greater.

Photoconductivity was initially used to give measurement of carrier densities [28-30]. SHG was ruled out by orientating the crystal such that the laser polarisation was along a high-symmetry direction. No variation in signal was observed and therefore 2PA was proposed as the dominant mechanism. The simpler, passive method of monitoring the optical transmission was also developed to measure the nonlinear absorption [31]. These early studies often deduced erroneously high values for β as a result of either neglecting the free carrier absorption or, in some cases, incorrectly interpreting results and assuming the absorption to be negligible (see [32] comments on [31]).

The importance of free carrier absorption and recombination during the relatively long nanosecond pulse lengths was finally appreciated and predictor-corrector computer programs were developed to step through and calculate carrier densities through out the pulse [32]. Reinterpretation of previous data resulted in an order of magnitude smaller β than originally determined.

Single mode, hybrid CO₂ lasers were developed with well-characterised beam properties to improve measurements through smoother temporal and spatial intensity profiles [33]. However the long pulses still required use of the stepping computer algorithms. At this time the ternary material Hg_xCd_{1-x}Te became available in bulk samples of sufficient optical quality to allow transmission measurements. Primarily a detector material like InSb, the bandgap of Hg_xCd_{1-x}Te can be varied by changing the x value [34]. Measurements on both materials with the hybrid lasers were compared with non-parabolic second order perturbation theory [11] and showed good agreement [35]. The frequency dependence of the 2PA coefficient was measured through cryogenic cooling. Again good agreement was seen with non-parabolic perturbation model, though a divergence was seen from Keldysh tunneling theory [36].

Measurements using shorter duration pulse (10's of ps) at far infrared wavelengths were finally reported by Sheik-Bahae et al in 1986 [37], a decade later than for narrow gap materials. A CO₂ laser based on optical free induction decay was used to measure two and three-photon absorption in InSb. The same OFID system was also used to observe three- and four-photon absorption in InAs [38,39].

Short pulse measurements of two-photon absorption in narrow gap materials away from CO₂ wavelengths were achieved in the 1990s with the advent of Free Electron Lasers (FEL). Early reports were of InSb measured at 8.9 μm [40] and Hg_xCd_{1-x}Te out to 40 μm [41]. The frequency dependence of InSb and InAs was subsequently measured and shown to have reasonable agreement with non-parabolic theory [42].

Most recently a further FEL laser measurement of two-photon absorption in InAs was reported by Berryman [43].

4.5 Summary of chapter

In this chapter the phenomenon of multi-photon absorption has been introduced. Theoretical models of multi-photon absorption have been reviewed. Second order perturbation theory has been used to predict the two-photon absorption coefficient for room temperature InAs. The results indicated a peak of $\beta \sim 1.3 \text{ cmMW}^{-1}$ at around 5 μm wavelength, then falling off rapidly to zero at 7 μm.

Reasons for trends in the measurement of two-photon absorption coefficient have been summarised. Measurements in narrow band-gap semiconductors are reviewed.

4.6 References

- 1 see for example AIP Center for History of Physics, "Heisenberg and the Uncertainty Principle," <http://www.aip.org/history/heisenberg/p08.htm>.
- 2 Goppert-Mayer, "Elementary processes with two quantum transitions," Ann Phys 9, 273 (1931).

- 3 TH Maiman, "Stimulated Optical Radiation in Ruby," *Nature* **187**, 493 (1960).
- 4 W Kaiser and CGB Garrett, "Two-Photon Excitation in CaF₂: Eu²⁺," *Phys Rev Lett* **7**, 229 (1961).
- 5 R. Braunstein, "Nonlinear Optical Effects," *Phys Rev* **125**, 475 (1962).
- 6 R Braunstein and N Ockman, "Optical Double-Photon Absorption in CdS," *Phys Rev* **134**, A499 (1964).
- 7 EO Kane, "Band structure of indium antimonide," *J Phys Chem Solids* **1**, 249 (1957).
- 8 NG Basov, AZ Grasiuk, VF Efimkov, IG Zubarev, VA Katulin, and JM Popov, "Semiconductor lasers using optical pumping," *Int Conf on Physics of Semiconductors, Kyoto*, 277 (1966).
- 9 NG Basov, AZ Grasiuk, IG Zubarev, VA Katulin, and ON Krokhin, "Semiconductor quantum generation with two photon optical excitation," *Sov Phys JETP* **23**, 366 (1966).
- 10 C.C. Lee and HY Fan, "Two-photon absorption with exciton effect for degenerate valence bands," *Phys Rev B* **9** (8), 3502 (1974).
- 11 C.R. Pidgeon, B.S. Wherrett, A.M. Johnston, J. Dempsey, and A. Miller, "Two photon absorption in zinc-blende semiconductors," *Phys Rev Lett* **42**, 1785 (1979).
- 12 C.R. Pidgeon, B.S. Wherrett, A.M. Johnston, J. Dempsey, and A. Miller, "Errata: Two photon absorption in zinc-blende semiconductors," *Phys Rev Lett* **43**, 1843 (1979).
- 13 MH Weiler, "Nonparabolicity and exciton effects in two-photon absorption in zincblende semiconductors," *Solid State Commun* **39**, 937 (1981).
- 14 B.S. Wherrett, "Scaling rules for multiphoton interband absorption in semiconductors," *J Opt Soc Am B* **1**, 67 (1984).
- 15 E.W. Van Stryland, H. Vanherzeele, M.A. Woodall, M.J. Soileau, A.L. Smirl, S. Guha, and Boggess T.F., "Two-photon absorption, nonlinear refraction, and optical limiting in semiconductors," *Opt Eng* **24**, 613 (1985).
- 16 L.V. Keldysh, "Ionization in the field of a strong electromagnetic wave," *Sov. Phys. JETP* **20** (5), 1307 (1965).
- 17 HS Brandi and CB Araujos, "Multiphoton absorption coefficients in solids: a universal curve," *J Phys C* **16**, 5929 (1983).
- 18 M. Sheik-Bahae, T Rossi, and J Kwok, "Frequency dependence of the two-photon absorption coefficient in InSb: tunneling effects," *J Opt Soc Am B* **4**, 1964 (1987).
- 19 MH Weiler, "Comments on 'Multiphoton absorption coefficients in solids: a universal curve'," *J Phys C* **17**, 1329 (1984).
- 20 D.C. Hutchings and E.W. Van Stryland, "Nondegenerate two-photon absorption in zinc blende semiconductors," *J Opt Soc Am B* **9**, 2065 (1992).
- 21 V. Nathan and A. H. Guenther, "Review of multiphoton absorption in crystalline solids," *J Opt Soc Am B* **2**, 294 (1985).
- 22 E.W. Van Stryland, M.A. Woodall, H. Vanherzeele, and M.H. Soileau, "Energy band-gap dependence of two-photon absorption," *Opt Lett* **10**, 490 (1985).
- 23 O Madelung, in *Landolt-Bornstein - Numerical Data and Functional Relationships Science and Technology*, edited by O Madelung and M Schulz (Springer-Verlag, Berlin, 1987), Vol. 22a Semiconductors - Intrinsic properties of Group IV elements and II-V, II-VI and I-VII compounds, p. 117.
- 24 MP Mikhailova, in *Handbook Series on Semiconductor Parameters (Ioffe Institute)*, edited by M Levinshtein, S Rummyantsev, and M Shur (World Scientific, 2000), Vol. 1 - Si, Ge, C (Diamond), GaAs, GaP, GaSb, InAs, InP, InSb, p. 147.

- 25 E.W. Van Stryland, M. Sheik-Bahae, A.A. Said, D.J. Hagan, and M.H. Soileau, in *Laser-Induced Damage in Optical Materials: 1993, Proceedings of the SPIE*, edited by HE Bennett, L.L. Chase, A. H. Guenther et al. (1994), Vol. 2114.
- 26 JH Bechtel and WL Smith, "Two-photon absorption in semiconductors with picosecond laser pulses," *Phys Rev B* **13**, 3515 (1976).
- 27 CKN Patel, P Fluery, R Slusher, and H Frisch, "Multiphoton plasma production and stimulated recombination radiation in semiconductors," *Phys Rev Lett* **16**, 971 (1966).
- 28 Fossum and Chang, "Two-Photon Excitation Rate in Indium Antimonide," *Phys Rev B* **8**, 2842 (1973).
- 29 AF Gibson, MJ Kent, and MF Kimmitt, "Photoconductivity in indium antimonide at 10.6 μm wavelength," *J Phys D* **1**, 148 (1968).
- 30 A.M. Danishevshii, A.A. Patrin, S.M. Ryvkun, and I.D. Yaroshetskii, "The effect of stimulated free-carrier absorption on two photon photoconductivity in semiconductors," *Sov Phys JETP* **29**, 781 (1969).
- 31 Doviak and et al, "Two-photon absorption in indium antimonide at 10.6 μm ," *J Phys C* **6**, 593 (1973).
- 32 AF Gibson, CB Hatch, PND Maggs, DR Tiley, and AC Walker, "Two-photon absorption in indium antimonide and germanium," *J Phys C: Solid State Phys* **9**, 3259 (1976).
- 33 J Dempsey, J Smith, GD Holah, and A Miller, "Nonlinear absorption and pulse shaping in InSb," *Opt Commun* **26**, 265 (1978).
- 34 GL Hansen, JL Schmit, and TN Casselman, "Energy gap versus alloy composition and temperature in HgCdTe ," *J Appl Phys* **53**, 7099 (1982).
- 35 A. Miller, A. Johnston, J. Dempsey, J. Smith, C.R. Pidgeon, and G.D. Holah, "Two-photon absorption in InSb and $\text{Hg}_{1-x}\text{Cd}_x\text{Te}$," *J Phys C* **12**, 4839 (1979).
- 36 A. Johnston, J. Dempsey, and C.R. Pidgeon, "Frequency dependence of two-photon absorption in InSb and $\text{Hg}_{1-x}\text{Cd}_x\text{Te}$," *Phys Rev B* **22**, 825 (1980).
- 37 M. Sheik-Bahae, P Mukherjee, and H.S. Kwok, "Two-photon and three-photon absorption coefficients of InSb," *J Opt Soc Am B* **3**, 379 (1986).
- 38 M.P. Hasselbeck, A.A. Said, E.W. Van Stryland, and M. Sheik-Bahae, "Three-photon absorption in InAs," *Opt Quantum Electron* **30**, 193 (1998).
- 39 M.P. Hasselbeck, E.W. Van Stryland, and M. Sheik-Bahae, "Scaling of four-photon absorption in InAs," *J Opt Soc Am B* **14**, 1616 (1997).
- 40 BN Murdin, C Mervielle, AK Kar, C.R. Pidgeon, DA Jaroszynski, JM Ortega, R Prazeres, and F Glotin, "Infrared free-electron laser measurement of power limiting by two-photon absorption in InSb," *Opt Quant Electron* **25**, 171 (1993).
- 41 J Burghoorn, VF Anderegg, TO Klaassen, WT Wenckebach, RJ Bakker, AFG van der Meer, D Oepts, and PW Amersfoot, "Free electron laser induced two-photon absorption in $\text{Hg}_{1-x}\text{Cd}_x\text{Te}$," *Appl Phys Lett* **61**, 2320 (1992).
- 42 BN Murdin and et al, "Excite-probe FEL (CLIO) study of two-photon-induced carrier dynamics in narrow gap semiconductors," *Nucl Instrum Methods A* **341**, 165 (1994).
- 43 KW Berryman and CW Rella, "Nonlinear absorption in indium arsenide," *Phys Rev B* **55** (11), 7148 (1997).

Chapter 5 - Nonlinear absorption measurements

5.1 Two photon absorption

Two photon absorption was measured in room temperature InAs by observing the nonlinear optical transmission as a function of input intensity.

Pulse energies of 2 μJ in a 3 mm diameter beam and pulse length τ (HWe^{-1}M) of 100 fs implied peak intensities of 300 MWcm^{-2} . With predicted 2PA coefficients of $\sim 1 \text{ cmMW}^{-1}$ this peak intensity was high enough that significant absorption was anticipated with the direct unfocused beam. This was extremely beneficial since it meant the beam size could be measured to high accuracy with the infrared camera thereby reducing one of the main sources of error in the nonlinear optical measurement. Virtually all previous measurements of β in narrow band gap materials have required significant focusing of the beam to small sizes of a few hundred microns where considerable uncertainty in the beam size is introduced.

The critical intensity at which absorption due to excited carriers becomes significant was derived by Bechtel and Smith [1] as:

$$I_{crit} \approx \frac{2\hbar\omega}{\sigma_h\tau(1-R)} \quad \text{Equation 5-1}$$

where $\hbar\omega$ is the photon energy, σ_h is the carrier absorption cross section, τ the HWe^{-1}M pulse duration of the laser pulse and R the surface reflectivity. I_{crit} as a function of pulse length is shown in Figure 5-1 for a wavelength of 5 μm . The carrier absorption cross section, σ_h , was taken to be $\sim 5 \times 10^{-16} \text{ cm}^{-2}$ based on values from Berryman [2].

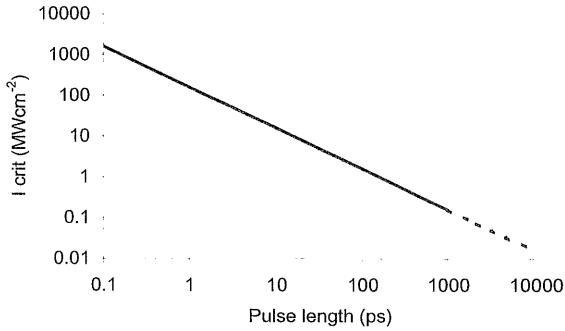


Figure 5-1: Critical intensity where free carrier absorption becomes significant compared two photon absorption as a function of pulse length

The dotted line for pulse lengths longer than 1 ns is an indication that Equation 5-1 may no longer be valid because carrier recombination could start occurring on such timescales.

For the 100 fs pulse duration of the OPA, I_{crit} was several times higher than the observed beam intensity. It was therefore judged that free carrier absorption would be negligible.

Using analyses described later in this chapter, the two-photon induced nonlinear transmission of a 1 mm thick InAs sample was calculated at the critical intensity for several pulse lengths and is shown below:

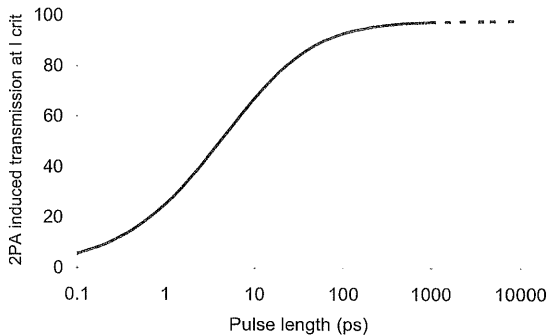


Figure 5-2: Two-photon induced nonlinear transmission at critical intensity as a function of pulse length

This demonstrates that two-photon absorption can only be clearly observed in isolation, without free carrier absorption, by using pulse lengths shorter than ~ 10 ps.

5.1.1 Experimental set-up

The experimental arrangement is shown below.

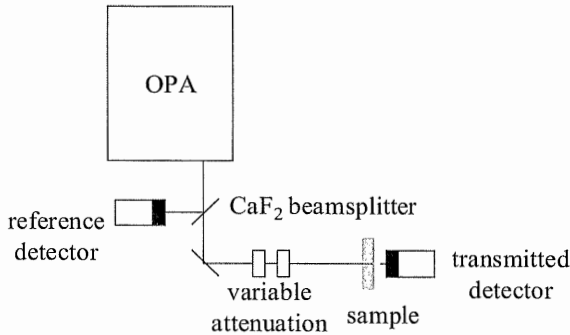


Figure 5-3: Experimental arrangement for two photon absorption measurements

The input intensity was varied by attenuation. The incident energy was monitored shot to shot by calibrating the calcium fluoride beamsplitter and reference J3-09 pyroelectric detector. Transmitted energy was measured with another J3-09 detector as the attenuation was changed.

Precautions were taken to ensure that the output detector collected all of the transmitted radiation. Nonlinear refraction through the sample associated with the 2PA and free carriers may have spread the beam and caused some energy to miss the final detector. This would result in the deduction of an erroneously high 2PA coefficient. The sample under test was placed as close as possible to the front of the transmitted energy detector to eliminate this possibility.

For each measurement wavelength the beam was fully characterised. The beam size at the sample position was recorded using the vidicon camera. The wavelength was checked using the monochromator and the pulse duration measured using the loudspeaker based

autocorrelator previously described in Chapter 3. The beamsplitter was recalibrated and a linearity check performed with no sample present. A typical result is shown below.

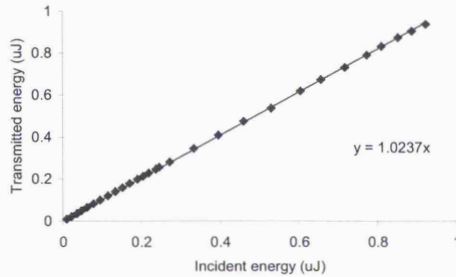


Figure 5-4: Linearity check with no sample present

5.1.2 Beam transmission model

Modelling of the nonlinear optical transmission to deduce a 2PA coefficient followed a similar treatment to that given by Van Stryland [3]. Figure 5-5 shows a schematic of the optical arrangement.

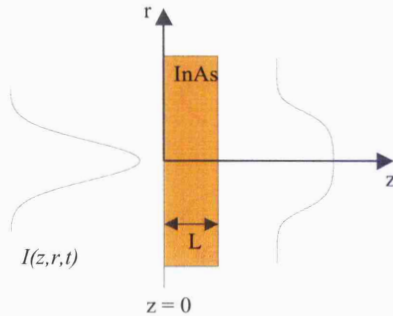


Figure 5-5: Schematic of optical arrangement assumed for beam transmission modelling

The intensity is a function of position, z , time, t , and assumed to be radially symmetric in r . The front surface of the sample is at $z=0$ and the sample is of thickness L . In the absence of significant free carrier absorption, the beam propagation through the sample is described by the expression:

$$\frac{dI}{dz} = -\alpha I - \beta I^2 \quad \text{Equation 5-2}$$

where α and β are the linear and two photon absorption coefficients respectively. This has a solution:

$$I(z, r, t) = \frac{I(0, r, t)(1-R)^j e^{-\alpha z}}{1 + I(0, r, t)(1-R)(1-e^{-\alpha z})\beta/\alpha} \quad \text{Equation 5-3}$$

where $I(0, r, t)$ is the initial boundary condition of the input beam to the sample, R is the sample surface reflectivity, $j=1$ inside the sample and 2 behind the sample. This can be rewritten:

$$I(z, r, t) = \frac{I(0, r, t)(1-R)^j e^{-\alpha z}}{1 + q(z, r, t)} \quad \text{Equation 5-4}$$

with

$$q(z, r, t) = I(0, r, t)(1-R)(1-e^{-\alpha z})\beta/\alpha \quad \text{Equation 5-5}$$

At the exit of the sample length L :

$$I(L, r, t) = \frac{I(0, r, t)(1-R)^2 e^{-\alpha L}}{1 + q(L, r, t)} \quad \text{Equation 5-6}$$

The incident beam is taken to be spatially and temporally Gaussian:

$$I(0, r, t) = I_0 \exp \left[-2 \left(\frac{r}{r_0} \right)^2 - \left(\frac{t}{t_0} \right)^2 \right] \quad \text{Equation 5-7}$$

such that r_0 is the HWe⁻²M beam size and t_0 is the HWe⁻¹M pulse length. I_0 is the peak intensity in the centre of the beam. Integration of the above expression reveals that, for a pulse of energy E :

$$I_0 = \frac{2E}{\pi \sqrt{\pi} t_0 r_0^2} \quad \text{Equation 5-8}$$

Substitution of the beam equation into Equation 5-6, followed by spatial and temporal integration results in an analytical expression for the overall pulse transmission:

$$T = \frac{2\alpha(1-R)}{I_0\sqrt{\pi}\beta(e^{\alpha L}-1)} \int_0^{\infty} \ln\left[1 + q(L,0,0)e^{-x^2}\right] dx \quad \text{Equation 5-9}$$

$$\text{where } q(L,0,0) = I_0(1-R)(1-e^{-\alpha L})\beta/\alpha$$

The integral in Equation 5-9 is solved directly by mathematical packages such as Mathcad allowing a complete solution to be determined without resorting to the summation expansions used by Berryman [2].

5.1.3 Results and discussion

Example nonlinear transmission data measured at a wavelength of 5 μm are shown below in Figure 5-6 together with a curve of the best value for β based on a least-squares fit of Equation 5-9.

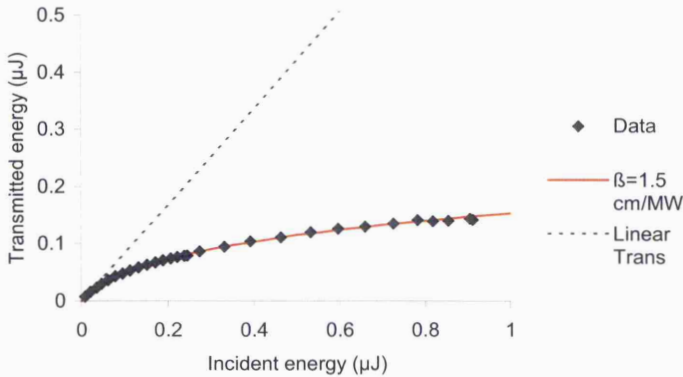


Figure 5-6: Nonlinear transmission arising from two photon absorption of beam through InAs at 5 μm

It can be seen that the experimental data fit well to the theoretical curve over the whole energy range. If free carrier absorption were taking place the data would tend to dip below the theory prediction at higher input energies.

The wavelength spectrum of the transmitted beam was measured to investigate whether any interesting features were present that could be indicative of preferential absorption or self phase modulation. The resultant data are shown in Figure 5-7 where the transmitted pulse is shown both in absolute magnitude and renormalized relative to the input pulse:

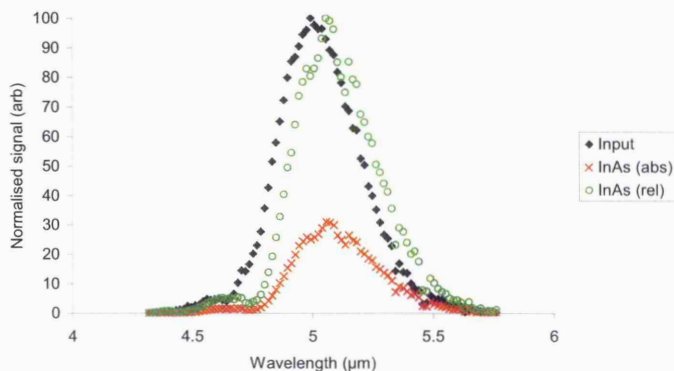


Figure 5-7: Transmitted spectra through InAs, absolute and renormalized against input

The observed red-shift of the transmitted spectrum relative to the input spectrum was expected since the two-photon absorption should preferentially absorb the higher energy, blue end photons. No additional features were present.

The measured wavelength dependence of the two-photon absorption coefficient is shown in Figure 5-8. Comparison is shown with the theoretical expression for 2nd order perturbation with non-parabolic bands presented in Chapter 4. Data of Berryman [2] and Murrin [4] are also plotted which were both measured using picosecond pulse length free electron lasers.

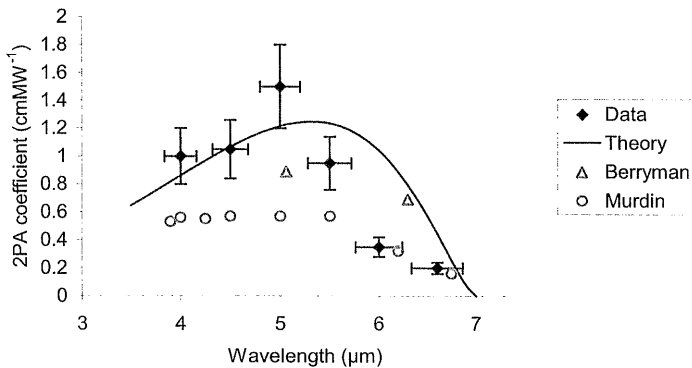


Figure 5-8: Wavelength dependence of measured two photon absorption coefficient

Good agreement is seen between the measured and theoretical coefficient between 4 and 5.5 μm . The horizontal bars indicate the FWHM spectral width of the OPA-DFM output. 20% vertical error bars are shown and represent the spread of results across three different samples, two antireflection coated and one uncoated. The main sources of error are uncertainty in the pulse length and sample transmission. The broad infrared output spectra created some uncertainty in defining the transmission values to be used in the analysis. Instead low energy readings were used for linear transmission values. However, for some wavelengths, the two-photon process was so strong that it was difficult to be certain that the linear regime was reached and still resolve the energies.

At longer wavelengths the measured coefficient falls off more rapidly than expected. This is believed to be due to two reasons:

Firstly the OPA output spectra are getting broader and an increasing portion of the output is at wavelengths where 2PA is negligible, particularly for the measurement centred at 6.5 μm . This portion beyond the 2PA limit will be transmitted linearly, giving higher transmission and lower apparent 2PA coefficient.

Secondly, the pulse duration was not known at the longer wavelengths because of the limitations of the InAs detector autocorrelation measurement of Chapter 3. An extrapolation was performed based on the shorter wavelength results. If the pulse length were longer than assumed, the intensity would be lower giving rise to a lower apparent 2PA coefficient. Further attempts of pulse length measurements at the longer wavelengths would be worthwhile.

5.1.4 Temporal broadening

An assumption in the above analysis is that the laser pulse length remains constant through the sample. Broadening of ultrashort pulses in optical media can occur through group velocity dispersion, which is related to the change in refractive index with wavelength. The pulse stretching, $\Delta\tau$, from propagation of a distance z inside a crystal is given by:

$$\Delta\tau = \frac{\tau'}{\tau} = \sqrt{1 + (z/L_D)^2} \quad \text{Equation 5-10}$$

where L_D is the dispersion distance defined as the length over which a transform-limited Gaussian pulse broadens by a factor of $\sqrt{2}$ [5]:

$$L_D = \frac{\Delta\tau^2}{4 \ln 2} \frac{2\pi c^2}{\lambda^3} \left(\frac{d^2 n}{d\lambda^2} \right)^{-1} \quad \text{Equation 5-11}$$

The refractive index was based on the empirical formula [6]:

$$n(\lambda) = \sqrt{11.1 + \frac{0.71}{1 - 6.5\lambda^{-2}} + \frac{2.75}{1 - 2085\lambda^{-2}} - 6 \times 10^{-4} \lambda^2} \quad \text{Equation 5-12}$$

where the wavelength, λ , is in μm . The second derivative was determined and is shown below in Figure 5-9.

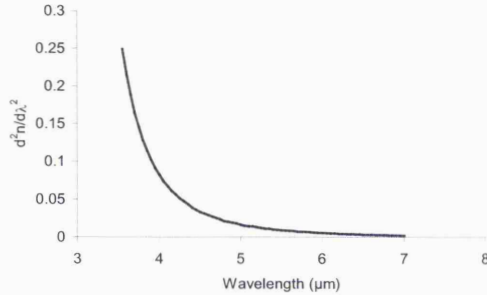


Figure 5-9: 2nd order derivative of wavelength dependent refractive index in InAs

The dispersion becomes significant as the wavelength approaches the bandgap. This was expected and is associated with the abrupt change in absorption. The curve was used to calculate the expected pulse broadening arising from the 1 mm thick InAs sample, using pulse lengths from the autocorrelation characterisation in Chapter 3. The result is shown in Figure 5-10:

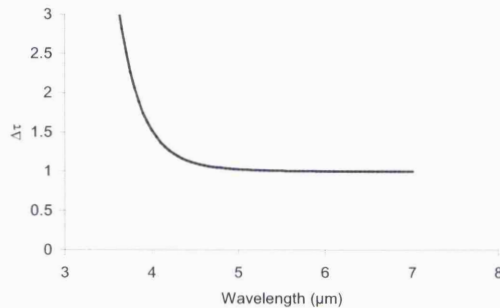


Figure 5-10: GVD pulse stretching through 1mm of InAs for OPA-DFM pulse lengths

This indicated that there was a possibility of some pulse broadening occurring at the shortest wavelength of 4 μm to around 1.5 times the original pulse length at the exit of the crystal. The average effect experienced by the two-photon absorption through the entire crystal would be around half of this. A longer pulse length would increase the two-photon absorption coefficient required to account for the observed nonlinear transmission.

However this calculation assumed a bandwidth-limited pulses. Pulse length measurements with the autocorrelator showed that chirp was present. Under certain conditions the GVD in InAs could have the reverse effect and shorten the pulse. Further phase characterisation of the beam would be required to determine the exact effect.

5.2 Free carrier absorption

One of the original aims of the work was to determine a free carrier absorption (FCA) coefficient. In particular the absorption cross section, σ_a , was desired for subsequent deduction of carrier densities from planned pump-probe transmission measurements.

FCA should become apparent at higher intensities. In the presence of free carriers, the beam propagation through the sample is governed by the expression:

$$\frac{dI}{dz} = -\alpha I - \beta I^2 - \sigma_a NI \quad \text{Equation 5-13}$$

where I is the intensity, z the propagation direction, α and β are the linear and two photon absorption coefficients respectively, σ_a is the free carrier absorption cross section and N is the free carrier density arising from the 2PA.

The free carriers increase the absorption and one would expect to see the measured transmission depart below the transmission predicted by model that includes only two-photon absorption.

Generation of free carriers is given by the rate equation:

$$\frac{dN}{dt} = \frac{\beta I^2}{2\hbar\omega} - \eta N \quad \text{Equation 5-14}$$

where η is the carrier recombination rate. For femtosecond pulses it was reasonable to assume that $1/\eta \gg \tau$, i.e. no recombination could take place during the ultrashort pulses.

The carrier densities induced by a pulse are therefore given by

$$N(t) = \frac{\beta}{2\hbar\omega} \int_{-\infty}^t I^2(t') dt' \quad \text{Equation 5-15}$$

Assuming a Gaussian pulse defined in Equation 5-7 allows the peak number of excess carriers to be determined as:

$$\Delta N = \frac{\sqrt{\pi} \beta t_0 I_0^2}{2\sqrt{2}\hbar\omega} \quad \text{Equation 5-16}$$

Higher intensities were achieved by focusing the beam. The accurate figures already obtained for β in low intensity regime were used to try and isolate additional absorption from free carriers.

5.2.1 Experimental arrangement

The experimental method used to measure the nonlinear absorption at high intensities was an open aperture z-scan. The z-scan is a well-known, powerful experimental technique for measuring both nonlinear absorption and refraction in optical materials [7]. A thin sample is scanned through the beam waist focus of a lens and the transmittance measured both in total (open) and through a finite aperture (closed). Provided that care is taken to gather all the transmitted light, the open scan is a measure of the nonlinear absorption. The closed aperture scan is dependent on both the absorption and refraction. Further details and data from closed aperture z-scans are presented later in this thesis.

The experimental arrangement is shown in Figure 5-11.

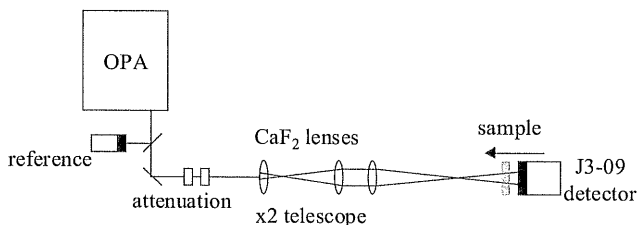


Figure 5-11: Experimental arrangement for open aperture z-scans

An expanding telescope doubled the beam diameter up to $\sim 6\text{mm}$ before focusing to provide a greater variation of intensity over the scan. A calcium fluoride lens of 100 mm focal length focused the beam onto the sample. The sample assembly was moved using a motorised translation stage. The experiment was controlled and data collected through a PC using LabVIEW.

The characteristics of the beam waist were investigated using the infrared camera. Near focus, the beam was observed down to $\sim 300\ \mu\text{m}$ in diameter which illuminated too few pixels on the camera for confidence in the calculated beam size. Pinhole scans were performed as a cross check.

For open aperture scans the sample was mounted on the front of a J3-09 pyroelectric detector. This ensured that all the transmitted light was collected however the signal was low and approached the detector noise limit for the lowest energy scans. Scans were also performed with no sample in place and some non-linearity was seen in the detector signal. This was not unexpected since the beam size on the detector element was changing significantly through the scan. Scans were normalised against the no-sample results and smooth, symmetric curves free from unexpected features were produced. No optical damage was observed during the z -scans. Although the peak intensities were extremely high at $\sim 30\ \text{GWcm}^{-2}$, the fluence was low at $\sim 20\ \text{mJcm}^{-2}$.

Data were compared against a pure two photon absorption model. Using the same treatment as section 5.1.2 the transmission was calculated as a function of z , the sample position:

$$T(z) = \frac{2\alpha(1-R)}{I_0(z)\sqrt{\pi}\beta(e^{\alpha L} - 1)} \int_0^\infty \ln \left[1 + q(z)e^{-x^2} \right] dx \quad \text{Equation 5-17}$$

$$q(z) = I_0(z)(1-R)(1 - e^{-\alpha L})\beta/\alpha$$

The z dependence was controlled by the variation of input intensity:

$$I_0(z) = \frac{2E}{\pi\sqrt{\pi} t_0 r(z)^2} \quad \text{Equation 5-18}$$

where E is the pulse energy, t_0 the HWe⁻¹M pulse length and $r(z)$ the HWe⁻²M beam radius at each z position. The radius was given by the following beam propagation equations:

$$r(z) = M^2 r_0 \left[1 + \left(\frac{z}{M^2 z_R} \right)^2 \right]^{1/2} \quad \text{Equation 5-19}$$

with

$$z_R = \frac{\pi r_0^2}{\lambda}, \quad r_0 = \frac{2f\#\lambda}{\pi} \quad \text{Equation 5-20}$$

where r_0 is the diffraction limited beam waist at focus ($1/e^2$ radius), z_R the diffraction limited Rayleigh range and $f\#$ the ratio of the input beam radius to lens focal length. M^2 is a measure of the beam quality given by the ratio of the real beam waist to r_0 . For a perfect beam $M^2 = 1$ and Equation 5-19 reduces to a standard Gaussian propagation equation.

Equation 5-19 was used to fit the beam size scans measured at each wavelength and a summary of the measured parameters and best fit coefficients is shown in Table 5-1.

Wavelength μm	Measured		Fit to Equation 5-19		f #	M ²
	r μm	Z _R mm	r ₀ μm	Z _R mm		
4	87	3.56	52	2.11	20.4	1.68
4.75	84	3.0	46	1.64	17.9	1.92
5.5	165	3.15	34	0.65	9.6	4.9

Table 5-1: Fitting parameters used to model focused beam propagation at each wavelength

It can be seen that the beams at 4 and 4.75 μm were fairly good quality with $M^2 < 2$. The beam at 5.5 μm was anomalous mainly because the beam was significantly larger at the input lens, caused by dispersion in the output collimating lens of the OPA. The larger beam made the effective lens speed faster and lowered the $f\#$.

5.2.2 Results and discussion

Measured data (dots) and a model calculation (line) for a low, 12 nJ energy scan at 4 μm wavelength are shown below. Negative z values correspond to the sample positioned before the beam waist.

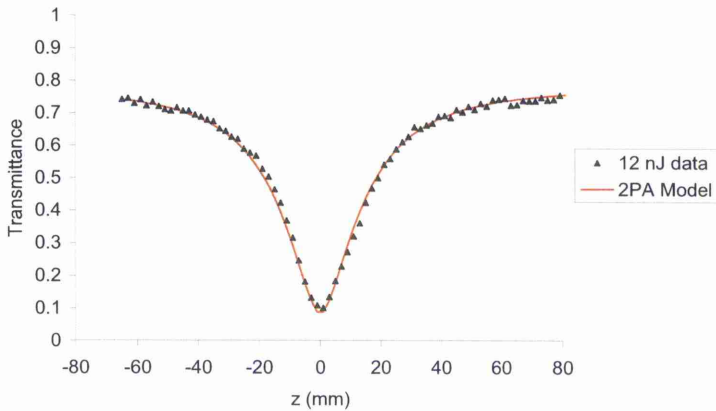


Figure 5-12: Open aperture z -scan of InAs with 12 nJ pulse energy at 4 μm wavelength

Good agreement with the 2PA model was seen throughout the scan indicating that no free carrier absorption was apparent. The peak irradiance at focus for this scan was $\sim 500 \text{ MWcm}^{-2}$.

The data for a higher energy 1.16 μJ scan are shown in Figure 5-13. Note the vertical axis is now logarithmic.

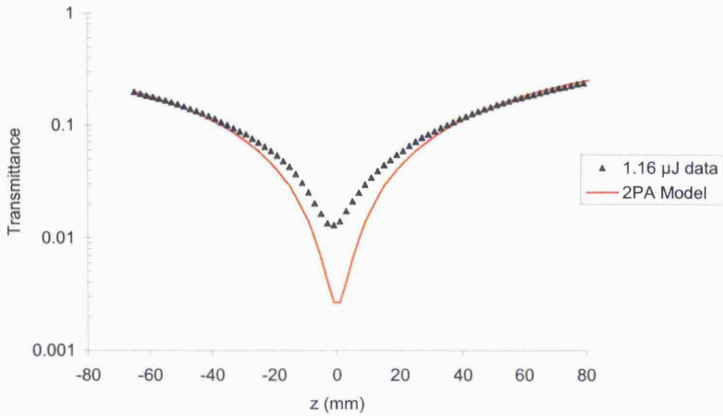


Figure 5-13: Open aperture z-scan of InAs with 1.16 μJ pulse energy at 4 μm wavelength

Good agreement with the 2PA model was still seen at low intensities away from focus. However the expected drop in measured transmittance at higher intensities was not seen. Instead the measured transmittance was actually higher than expected from 2PA alone. The data are summarised in Figure 5-14 which shows the transmittance as a function of calculated peak incident irradiance.

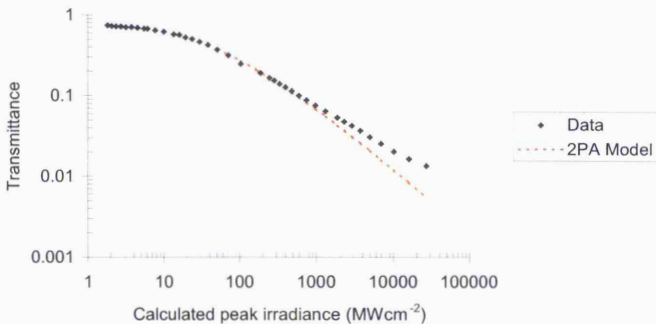


Figure 5-14: Transmittance of InAs as function of irradiance measured in open aperture z-scan

This shows good agreement up to $\sim 500 \text{ MWcm}^{-2}$ after which the measured transmittance deviates upwards. At no point does the transmittance dip below the 2PA model which

would occur if free carrier absorption were present. The same trend was observed at other measurement wavelengths of 4.75 and 5.5 μm .

Several possible reasons are proposed why no free carrier absorption was apparent and a transmission increase was observed:

- Beam spreading through nonlinear refraction
- Saturation of two-photon absorption
- Dependence of free-carrier absorption coefficient on pulse length

The most likely cause for the observed increase in transmittance at intensities above 500 MWcm^{-2} is nonlinear refraction and beam spreading arising from the free carrier plasma. This will be described and studied in more detail in next chapter. At sufficiently high input intensities the beam will be defocused early within the sample. The sample is no longer optically thin and the “external self-action” regime is no longer satisfied [8]. This will reduce the intensity later in the sample, less 2PA will take place and the observed transmission will be higher than expected. This is likely to be occurring at the highest energies near focus. However the lack of FCA at intermediate energies away from focus was still unexpected.

Saturation of the two photon absorption coefficient could also be occurring. Temporal evolution of the carriers and relaxation processes are covered fully later in Chapter 7. The generated free carriers do not have time during a ~ 100 fs pulse to relax or thermalise within the band. A limited number of states are therefore available at energy corresponding to the two-photon energy. As these states fill up the two-photon transitions become blocked and the transmission would rise.

For absorption of conventional monochromatic laser light the induced carrier distribution will be narrow in energy. Saturation could be expected to occur rapidly. The infrared fs pulses from the OPA were unusual because of the significant spectral width. This would

tend to produce a distribution of states with significant width in energy. For example, the $0.4 \mu\text{m}$ spectral width observed at $5 \mu\text{m}$ corresponded to photon energies $0.25 \pm 0.02 \text{ eV}$. Since the excitation process of interest was two-photon, a continuum of states with a width of 0.08 eV could be expected. This is illustrated in Figure 5-15.

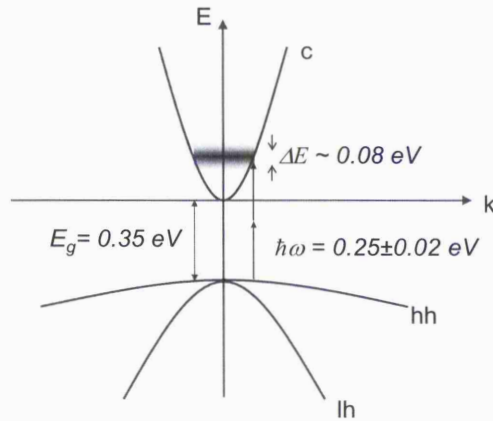


Figure 5-15: Distribution of states resulting from two-photon absorption of fs pulse at $5 \mu\text{m}$ with significant energy dispersion.

The effect of this distribution is to increase the number of potential states available for two-photon absorption and therefore reduce any saturation effects.

The use of ultrashort fs pulses will be affecting the apparent absorption coefficient. The pulse length dependence of free carrier absorption has been investigated by Mukherjee et al [9,10] who observed a decrease in the absorption coefficient of InSb for low energy, sub 100 ps pulses from a CO_2 OFID system as described in Chapter 2.

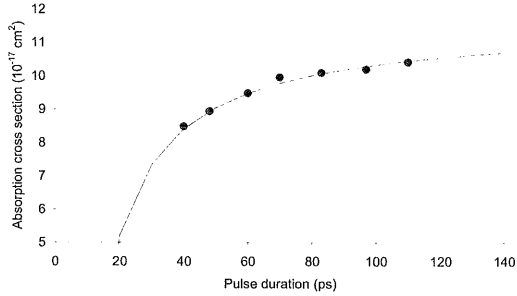


Figure 5-16: Absorption cross section in InSb as function of pulse length. Dashed line represents long pulse absorption at 100 ns. Solid line is theoretical fit with relaxation time of 5.6 ps. Data of Mukherjee et al [9] Fig 1 replotted based on sample 0.037 cm thick and $n_i=1.5 \times 10^{18} \text{ cm}^{-3}$.

The trend was attributed to incomplete carrier relaxation within the laser pulse duration. For long pulse duration, the absorption cross section can be obtained from the classical Drude model of the electron-hole plasma as:

$$\sigma_0 = \frac{4\pi e^2}{m^* n \omega^2 \tau c} \quad \text{Equation 5-21}$$

where m^* is the effective mass, n the refractive index, ω the laser frequency and τ the damping time constant in the classical model. The damping time can be interpreted as the interband relaxation time. If the laser pulse length is comparable to the relaxation time τ the carriers do not have sufficient time to relax leading to a reducing damping force. For a decaying pulse with exponential fall time τ_p , the equation is modified to:

$$\sigma = \frac{4\pi e^2 (1/\tau - 1/\tau_p)}{m^* n \omega^2 \tau c} \quad \text{Equation 5-22}$$

i.e.

$$\sigma = \sigma_0 (1 - \tau/\tau_p) \quad \text{Equation 5-23}$$

This is shown as the solid line in Figure 5-16 with a relaxation time of 5.6 ps giving best fit to the experimental data. The relation clearly breaks down for $\tau_p < \tau$, which is the case for fs duration pulses indicating the Drude model is no longer valid.

5.3 Summary of Chapter

In this chapter the nonlinear absorption of infrared fs pulses in room temperature InAs has been characterised. Two-photon absorption was measured by observing the nonlinear optical transmission as a function of input intensity. A beam propagation model enabled a two-photon absorption coefficient to be determined from the limiting curves. The wavelength dependence of the 2PA coefficient was compared with the theoretical predictions of the previous chapter. Good agreement was seen from 4 to 5.5 μm , above which the measured coefficient was smaller than expected. This was attributed to uncertainty in the pulse length and broad wavelength distribution.

Further study of 2PA at high input intensities was achieved through open aperture z-scans. No additional absorption was observed from free carriers. This was attributed to the carriers having insufficient time to undergo intra-band relaxation. Increased transmission at very high intensities was attributed to refractive beam spreading and possibly saturation effects.

5.4 References

- 1 JH Bechtel and WL Smith, "Two-photon absorption in semiconductors with picosecond laser pulses," *Phys Rev B* **13**, 3515 (1976).
- 2 KW Berryman and CW Rella, "Nonlinear absorption in indium arsenide," *Phys Rev B* **55** (11), 7148 (1997).
- 3 E.W. Van Stryland, H. Vanherzeele, M.A. Woodall, M.J. Soileau, A.L. Smirl, S. Guha, and Boggess T.F., "Two-photon absorption, nonlinear refraction, and optical limiting in semiconductors," *Opt Eng* **24**, 613 (1985).
- 4 BN Murdin and et al, "Excite-probe FEL (CLIO) study of two-photon-induced carrier dynamics in narrow gap semiconductors," *Nucl Instrum Methods A* **341**, 165 (1994).

- 5 HP Li, CH Kam, YL Lam, and W Ji, "Femtosecond z-scan measurement of
nonlinear refraction in nonlinear optical crystals," *Opt Mater* **15**, 237 (2001).
- 6 MP Mikhailova, in *Handbook Series on Semiconductor Parameters (Ioffe
Institute)*, edited by M Levinstein, S Rumyantsev, and M Shur (World Scientific,
2000), Vol. 1 - Si, Ge, C (Diamond), GaAs, GaP, GaSb, InAs, InP, InSb, p. 147.
- 7 M. Sheik-Bahae, A.A. Said, and E.W. Van Stryland, "High sensitivity, single beam
 n_2 measurements," *Opt Lett* **14**, 955 (1989).
- 8 E.W. Van Stryland, M. Sheik-Bahae, A.A. Said, D.J. Hagan, and M.H. Soileau, in
Laser-Induced Damage in Optical Materials: 1993, Proceedings of the SPIE,
edited by HE Bennett, L.L. Chase, A. H. Guenther et al. (1994), Vol. 2114.
- 9 P Mukherjee, M. Sheik-Bahae, and H.S. Kwok, "New method of measuring
relaxation times in semiconductors," *Appl Phys Lett* **46**, 770 (1985).
- 10 P Mukherjee, M. Sheik-Bahae, and H.S. Kwok, in *Energy beam-solid interactions
and transient thermal processing - MRS Symposia*, edited by DK Biegelson, GA
Rozgonyi, and CV Shank (Materials Research Society, Boston, 1985), Vol. 35, p.
97.

Chapter 6 - Nonlinear refraction

6.1 Introduction

Nonlinear refraction is fundamentally tied to nonlinear absorption. A causality argument leads to the deduction that any change in absorption at one frequency must be accompanied by a phase shift, or refractive change at all other frequencies [1]. This is expressed analytically through the Kramers-Kronig relations:

$$n(\omega) - 1 = \frac{c}{\pi} \mathbf{P} \int_0^{\infty} \frac{\alpha(\omega')}{\omega'^2 - \omega^2} d\omega' \quad \text{Equation 6-1}$$

where \mathbf{P} represents the Cauchy principal value. Normally such a dispersion relation is only valid for linear systems, and might not be expected to valid for nonlinear optics. However, this can be resolved by considering the material plus the strong perturbing light beam as a new system. This new system would still be linear if probed by a weaker beam. The Kramers-Kronig relation can be applied in the presence and absence of the perturbation and the difference becomes:

$$\Delta n(\omega; \zeta) = \frac{c}{\pi} \mathbf{P} \int_0^{\infty} \frac{\Delta \alpha(\omega'; \zeta)}{\omega'^2 - \omega^2} d\omega' \quad \text{Equation 6-2}$$

where ζ is the perturbation.

There are many processes that can give rise to nonlinear absorption and refraction within a semiconductor. A comprehensive review and analytical treatment through the Kramers-Kronig relations has been published by Sheik-Bahae and Van Stryland [2]. In general the processes can be divided into cumulative free carrier effects or non-resonant, ultrafast effects.

6.1.1 Free carrier effects

The cumulative free carrier refraction arises from the free-carrier plasma, band-filling (dynamic Burstein-Moss) and bandgap renormalisation contributions. The carriers are generated by two-photon absorption but the refractive effects are not instantaneously self-acting. Instead they are an accumulation and act on subsequent light giving rise to an apparent cascaded fifth order, $\chi^{(5)}$ effect [1]. This is also consistent with their quadratic dependence on intensity.

The free carrier plasma refraction results from the intraband free carrier absorption and is described by the Drude-Lorentz model [3]. The change in refractive index, Δn , is given by:

$$\Delta n_p = \sigma_{rp} \Delta N = \frac{-e^2}{2n_0 \epsilon_0 \omega^2 m_{cv}} \Delta N \quad \text{Equation 6-3}$$

where σ_{rp} is the refractive cross section, e is the electronic charge, n_0 the linear refractive index, ω the light frequency and ϵ_0 the permittivity of free space. ΔN is the induced change in carrier density, and m_{cv} is the combined reduced effective mass of the conduction and valence bands, given by:

$$m_{cv} = \frac{m_c m_v}{m_c + m_v} \quad \text{Equation 6-4}$$

The valence band effective mass is further complicated by the presence of the light and heavy hole bands. Their masses are averaged out to a single valence band effective mass:

$$m_v = \frac{m_{hh}^{3/2} + m_{lh}^{3/2}}{m_{hh}^{1/2} + m_{lh}^{1/2}} \quad \text{Equation 6-5}$$

For InAs $m_c=0.023m_0$, $m_{lh}=0.026m_0$ and $m_{hh}=0.41m_0$ giving $m_v=0.33m_0$ and $m_{cv}=0.0215m_0$ [4]. The plasma refraction cross section defined in Equation 6-3 is thus calculated at a wavelength of 4 μm to be $\sigma_{rp}=0.95 \times 10^{-19} \text{ cm}^3$.

The band-filling contribution occurs when the injected carriers relax to bottom of the conduction band and saturate the available states blocking band-to-band transitions. This phenomenon can be especially strong in InSb and InAs because of the small effective mass of the conduction band and the consequent low density of states at the band minima. The overall effective is to enlarge the bandgap. The same effect was observed by Burstein and Moss through heavy doping, hence the description of this as a dynamic Burstein-Moss shift (DBMS). The absorption change is negative and most significant at wavelengths with energy close to the bandgap (i.e. resonant). The nature of the Kramers-Kronig dispersion relationship means that the refractive changes arising from the $\Delta\alpha$ may be observed at frequencies away from resonance. Hence this effect can become significant for refraction from the two-photon absorption process. The band-filling effect is, to first order, linearly dependent on the induced carrier density, ΔN .

Bandgap renormalisation is caused by interactions between the free carriers at the bottom of the conduction band. When the spacing approaches that of the effective Bohr radius, carriers with the same spin will tend to repel each other. The result is a lowering of energy and narrowing of the bandgap which is therefore in the opposite direction of band-filling. The renormalisation scales with particle spacing which is proportional to $\Delta N^{1/3}$ and is thus weaker than the band-filling effect.

Thorough treatments of the nonlinear refractive index arising from free carriers have been published by Paskov for a variety of materials including InAs, InSb and their ternary alloys [5-7]. The methodology was to derive the band-filling and normalisation absorption changes using a non-parabolic Kane band structure and Fermi-Dirac statistics. The corresponding refractive changes were then calculated by numerical integration of the Kramers-Kronig expression followed by addition of the free carrier plasma contribution. A free carrier cross section of $-2 \times 10^{-19} \text{ cm}^3$ was predicted at 4 μm wavelength from a

refractive index of -0.08 arising from a carrier density of $4 \times 10^{17} \text{ cm}^{-3}$. This indicates band-filling and normalisation contribute a factor of two enhancement to the plasma refraction at this wavelength. As the wavelength increases, the enhancement would be expected to decrease from moving off resonance with the bandgap.

A simplified form of the free carrier induced refractive cross section taking band filling into account was given by Auston [8] and adopted by Van Stryland and colleagues in various papers [2,9,10]:

$$\sigma_{r-Auston} = \frac{-e^2}{2n_0\epsilon_0\omega^2 m_{ch}} \cdot \frac{1}{1 - \left(\frac{\hbar\omega}{E_g}\right)^2} \quad \text{Equation 6-6}$$

The second term is an approximation for band-filling effects, though it is apparent that the expression breaks down near bandgap resonance ($\hbar\omega \sim E_g$).

An different expression comparing the band filling DBMS and plasma contributions was given by Miller et al [11] as:

$$\frac{\Delta n_{plasma}}{\Delta n_{DBMS}} = 4 \left(1 - \frac{\hbar\omega}{E_g} \right) \quad \text{Equation 6-7}$$

The plasma contribution is therefore stronger for photon energies less than 75% of the bandgap. The blocking contribution dominates for photon energies between 75 and 100 %, i.e. as resonance is approached. From this an alternative relationship for the refractive cross section can be deduced:

$$\sigma_{r-Miller} = \frac{-e^2}{2n_0\epsilon_0\omega^2 m_{ch}} \cdot \left[1 + \frac{1}{4 \left(1 - \frac{\hbar\omega}{E_g} \right)} \right] \quad \text{Equation 6-8}$$

The magnitude and wavelength scaling of both the Auston and Miller expressions are shown in Figure 6-1 with comparison to the plasma only contribution and Paskov's results.

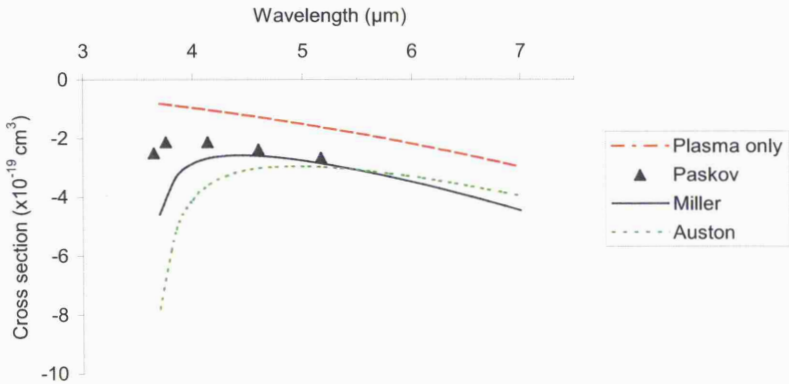


Figure 6-1: Comparison of models for free carrier refractive cross section
Paskov data interpolated from Figure 1 reference [6]

It can be seen that the Miller approach provides the better approximation to predictions of Paskov, with the Auston enhancement appearing to be too strong near bandgap resonance.

The net free carrier effect below the bandgap is always negative, i.e. the beam is spread out and defocused. This phenomenon forms the basis of the two photon induced fluence limiting observed with narrow gap semiconductors. From a practical standpoint, it is fortunate that the process defocuses the beam since self-focusing often leads to optical damage.

6.1.2 Ultrafast effects

The ultrafast, or n_2 Kerr-type refractive contribution is directly related to the two-photon absorption. The instantaneous self-interaction corresponds to the real part of the third order susceptibility $\chi^{(3)}$. Normally this effect would not be need to be considered for longer duration pulses where the peak intensity is too low and considerable carrier densities are

generated which would dominate the observed refraction. However, the ultrafast refraction should be considered with the low energy, high intensities achievable with the femtosecond pulse OPA.

The ultrafast n_2 change in refractive index for the degenerate case of absorbed photons with the same energy has been determined by Sheik-Bahae et al [12]. The second order perturbation expression for 2PA was used with a parabolic bands approximation:

$$\beta(\omega) = K \frac{1}{n^2(\omega)E_g^3} F\left(\frac{2\hbar\omega}{E_g}\right) \quad \text{Equation 6-9}$$

$$\text{where } F(x) = \frac{(2x-1)^{3/2}}{(2x)^5}$$

The Kramers-Kronig relation was applied to Equation 6-9 to obtain the resultant refraction:

$$\begin{aligned} n_2(\omega) &= \frac{\Delta n(\omega)}{I_\omega} = K \frac{\hbar c}{2} \frac{\sqrt{E_p}}{n^2(\omega)E_g^4} G\left(\frac{\hbar\omega}{E_g}\right) \\ &= K' \frac{\sqrt{E_p}}{n^2(\omega)E_g^4} G\left(\frac{\hbar\omega}{E_g}\right) \end{aligned} \quad \text{Equation 6-10}$$

This retains a similarity to the original 2PA expression except now the bandgap scaling is E_g^{-4} and the dispersion function G more complicated:

$$G(x) = \frac{-2 + 6x - 3x^2 - x^3 - \frac{3}{4}x^4 - \frac{3}{4}x^5 + 2(1-2x)^{3/2}\Phi(1-2x)}{64x^6} \quad \text{Equation 6-11}$$

where $\Phi(y)$ is the Heaviside step function which returns zero if y is negative, and 1 otherwise.

The value of the K' constant used was a best fit of $6 \times 10^{-5} \text{ cm}^2 \text{ eV}^{7/2} \text{ MW}^{-1}$ obtained from prior literature data [14]. The calculated wavelength dependence of n_2 for room temperature InAs is shown in Figure 20.

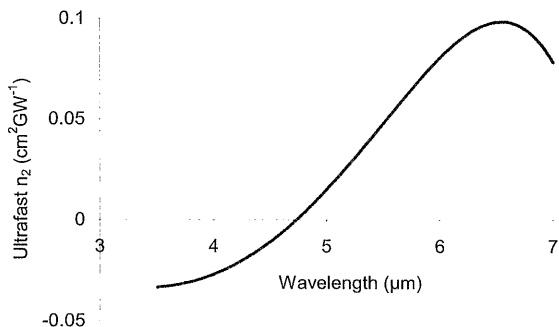


Figure 6-2: Magnitude and wavelength dependence of ultrafast n_2 refraction in InAs

It is noticeable that the sign of n_2 goes through an inversion at $\sim 4.75 \mu\text{m}$. For wavelengths shorter than this the refraction is negative and complementary to the free carrier contributions. For longer wavelengths the refraction is positive so self-focusing should occur that is opposite to, and may partially suppress the free carrier refraction. It was of interest to determine whether this difference could be observed with an enhancement or reduction of the overall refraction, as determined by the wavelength.

The magnitude of the n_2 coefficient implied that very large changes in refractive index might be induced. When focused to a few hundred microns, the peak intensity in the OPA beam could potentially be as high as 10 GWcm^{-2} . This would give rise to changes of index of ± 0.5 . Realistically such changes will not be achieved because the absorption of the beam is limited through strong beam spreading from the free carrier refraction and saturation of the 2PA.

6.2 Review of narrow-gap nonlinear refraction measurements

It is perhaps surprising that although multi-photon and free-carrier nonlinear absorption effects were observed and measured in narrow bandgap semiconductors in the mid 1960s

[13,14], it was not until the late 1970s that large order non-linear refractive effects associated with the induced free carrier distributions were first reported.

Nonlinear refraction came into prominence with the observations of Miller et al [15] in 1978. Strong beam distortion and nonlinear absorption were observed in cryogenically cooled InSb when illuminated with a continuous wave CO laser at wavelengths close to the bandgap, from 5.2 to 6 μm . The power levels were low enough, at ~ 10 mW, that thermal mechanisms were ruled out. Beam propagation modelling showed that only negative (defocusing) refraction was consistent with the observed beam profiles [16]. The nonlinear susceptibility n_2 , was calculated to be $-6 \times 10^{-5} \text{ cm}^2\text{W}^{-1}$. This was several orders of magnitude larger than values previously predicted from bound electron and conduction band non-parabolicity mechanisms.

The phenomena were attributed to the band filling, described in Section 6.1.1, which at wavelengths resonant with the bandgap dominate over any plasma contribution. Saturation of the free carrier states in the conduction band caused a dynamic Burstein-Moss shift. This gave rise to a reduction in absorption and hence a change of refractive index as a result of the inter-dependence [11,17]. The process became known as bandgap resonant nonlinear refraction [18].

Similar observations were also made in $\text{Cd}_{0.21}\text{Hg}_{0.79}\text{Te}$ with a CW CO_2 laser and showed that Auger recombination processes accounted for an observed $I^{1/3}$ intensity dependence of the nonlinear refractive index change [19]. The paper shows the results of scanning the sample through the focus of a lens (Figure 2a in ref). The peak-trough characteristic of a negative refraction z-scan is evident once it is appreciated that beam width was plotted, the inverse of transmitted intensity. This can be therefore be considered the first ever closed aperture z-scan result some 7 years prior to the full power of the technique being realised by Sheik-Bahae et al [20].

The nonlinear refraction was quickly exploited to achieve optical bistability [21,22]. Optical switching and amplification was observed through the intensity-dependent path length change within a Fabry-Perot etalon. The experiment consisted of a simple, cryogenically-cooled plane parallel InSb crystal. Several orders of $\lambda/2$ phase shifts were seen, with a 5th order hysteresis loop. The optical analogy of a transistor was observed where a second, weaker switching beam could induce large modulations in the primary beam.

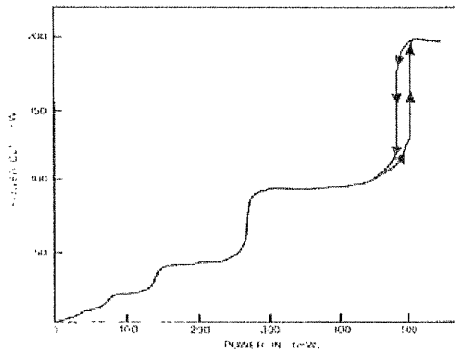


*Figure 6-3: Optical bistability in InSb through bandgap resonant nonlinear refraction
From Miller et al [23]*

Bistable properties were also observed with $\text{Cd}_x\text{Hg}_{1-x}\text{Te}$ etalons where composition tuning of the band-edge allowed room temperature operation [24,25].

Bandgap resonant refraction and bistability in InAs was demonstrated by Poole and Garmire [26]. A quasi-CW HF laser was used with an output wavelength of 3.096 μm . The bandgap of the InAs was tuned around this wavelength by cryogenically cooling it to temperatures near 77K. Bistability was seen at powers as low as 3 mW. The bandfilling theory was expanded to include a light hole contribution and Fermi-Dirac statistics giving good agreement with their results [27,28].

Bistability through two-photon excitation was first reported by Kar et al [29] who used a pulsed CO₂ laser to excite room temperature InSb. Two-photon absorption offered a wider range of operating wavelength and higher transmission prior to switching. Bandgap resonant operation, by definition, worked at limited wavelengths within the absorption tail of the band-edge so experienced inherent absorption losses. Further studies with long, ~ 2 μsec duration length hybrid laser pulses gave quasi-CW operation [30]. The $I^{2/3}$ intensity dependence of the induced nonlinear refraction was again consistent with Auger recombination effects. Evidence of concentric rings was seen in the temporal evolution of far field spatial profiles. This highlighted that the diffractive effect of the spatial variations needed to be considered for proper devices [31]. Similar results were achieved with Cd_xHg_{1-x}Te with switching on nanosecond timescales [32-34].

Guha et al were the first to consider both free carrier and ultrafast, n_2 nonlinear refraction in their measurements on two-photon absorption in CdSe [35]. This was necessary because of the use of short, picosecond duration pulses from a mode-locked Nd:YAG with significantly higher intensity than the previous studies, most of which used CO₂ lasers. Another significant step was the use of the full Huygen-Fresnel formalism to calculate the beam propagation after the sample. Previous calculations were based on the Gaussian decomposition method [16]. Spatial profiles were observed with a vidicon and showed the dramatic effect of beam spreading. Peak fluences were measured at various positions both on and off-axis. Good agreement was seen with a model that attributed the refraction solely to free carrier effects. Similar picosecond pulse length defocusing results were reported in the narrow bandgap material InSb by Sheik-Bahae and Kwok using an optical free induction decay CO₂ laser [36], previously described in Chapter 2. Ultrafast Kerr-type n_2 nonlinear refraction was again included in the propagation equations but later argued to be negligible.

The advent of the z-scan technique in 1989 finally gave a rigorous protocol for the proper characterisation of nonlinear absorption and refraction. Van Stryland and colleagues reported extensive results of the magnitude and dispersion of the third order, ultrafast refraction [12,37-39]. Excellent agreement was observed with the emerging theory described in Section 6.1.2. Measurements concentrated on wider bandgap materials because of the availability of the mode-locked Nd:YAG laser for high quality short, ps pulses. The higher effective masses also meant the free carrier contributions were smaller than observed in narrow-gap semiconductors.

6.3 Simple experimental observation of nonlinear refraction

We now move to experimental observations of nonlinear refraction made with the ultrafast OPA system. A straightforward method of observing two-photon induced nonlinear refraction was to view the beam transmitted through the InAs at some distance after the sample using the vidicon camera. This was equivalent to the original method used by Miller and later by Guha et al [15,35].

The experimental arrangement is shown below:

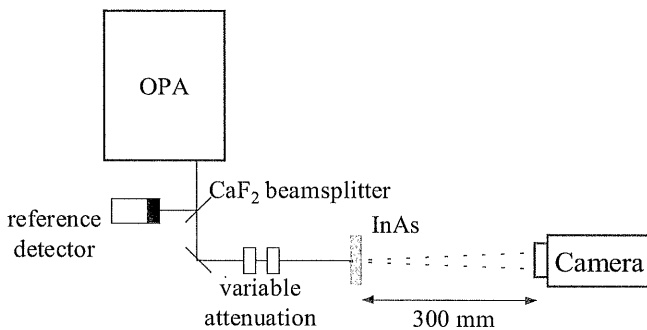


Figure 6-4: Experimental arrangement for observation of nonlinear refraction

The OPA output wavelength was fixed at 4 μm and the output energy calibrated using the beamsplitter and reference detector. The beam was first observed at the sample position to

determine the input intensity. The camera was then set back 300 mm back and the profile recorded again still with the sample removed. Camera data was exported to text files enabling the major horizontal and vertical axes to be extracted and plotted externally. The horizontal profile with no sample is shown below and indicates a good Gaussian distribution of 3.3 mm width (FW $e^{-2}M$):

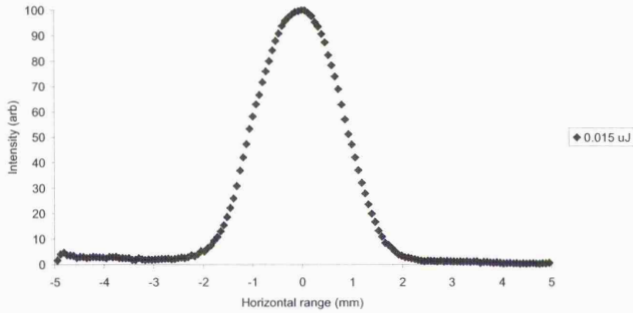


Figure 6-5: Horizontal beam profile with no sample, energy 0.015 μJ

The sample was then inserted and the beam profiles recorded as the incident energy was increased. The resultant horizontal profiles are shown below and have been normalised against the peak intensity observed with no sample.

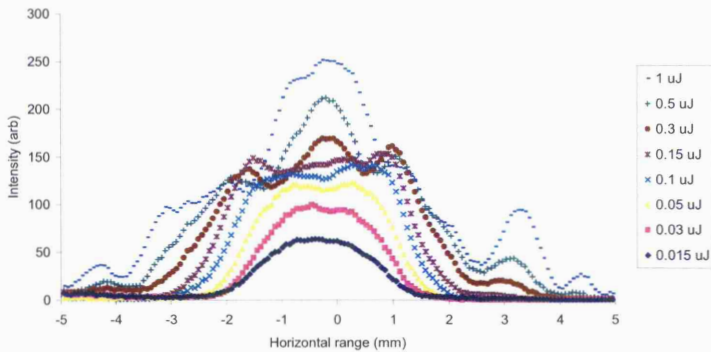


Figure 6-6: Horizontal beam spreading from nonlinear refraction in InAs, normalised against no sample intensity of 100 at 0.015 μJ

The effects of nonlinear refraction were clearly visible with the beam spreading out as the input intensity increased. The low energy curves showed broadening that could be partly attributed to two-photon absorption. Peaks and troughs at the higher energies were evidence of strong diffraction caused by large phase changes. The profile at 0.5 μJ (green crosses) bore a particular resemblance to the far-field profiles observed by Miller et al [16]. The results demonstrated the effective fluence limiting action of the semiconductor. Although the input energy was increased over 66 times in magnitude, the on-axis transmitted intensity only increased by a factor of 2.5. The transmitted intensity calculated in the centre of the beam is shown in Figure 6-7 as a function of input intensity.

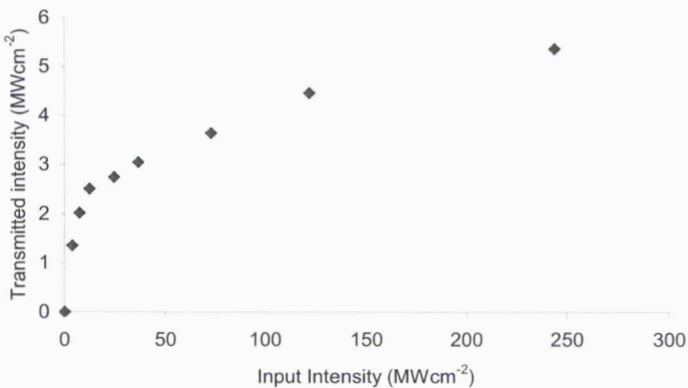


Figure 6-7: Transmitted on-axis intensity as function of input intensity

6.4 z-scan experiments

6.4.1 Introduction

The z-scan was previously introduced in Chapter 5 as a powerful technique for measuring both nonlinear absorption and refraction in optical materials [40]. A thin sample is scanned through the beam waist focus of a lens and the transmittance measured both in total (open)

and through a finite aperture (closed). Provided that care is taken to gather all the transmitted light, the open scan is a measure of the nonlinear absorption.

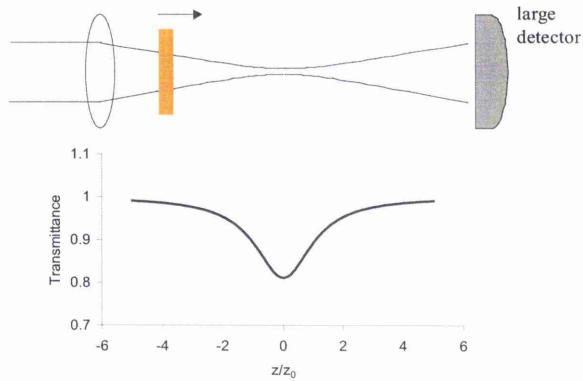


Figure 6-8: Open aperture z-scan schematic. The resultant transmittance curve shows the effects of nonlinear absorption

The closed aperture scan is dependent on both the absorption and refraction. In front of focus at low intensity the refraction is minimal. Closer to focus the intensity increases and a self-defocusing effect tends to collimate the beam and hence gives rise to an increase in apparent transmittance. Once past focus the defocusing spreads the beam further and the aperture transmittance decreases. Continuing further out reduces the effect and the transmittance returns to unity.

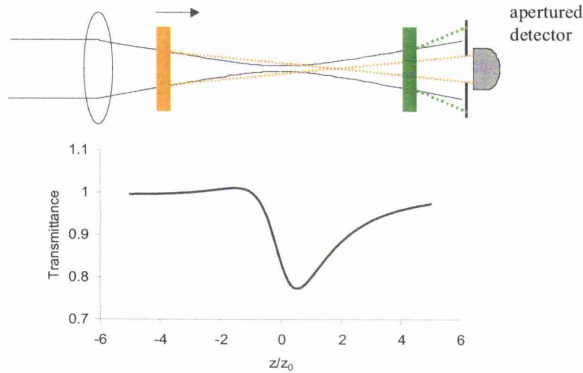


Figure 6-9: Closed aperture z-scan schematic showing self-defocusing. The resultant transmittance curve is a superposition of nonlinear refraction and absorption

Nonlinear refraction can be isolated by plotting the ratio of the intensity recorded in the closed-aperture scan to the corresponding open-aperture value; this eliminates the effects of nonlinear absorption. A peak-trough pattern is thus characteristic of a negative, defocusing nonlinearity. For a positive, self-focusing nonlinearity the situation is reversed and a trough-peak is the outcome.

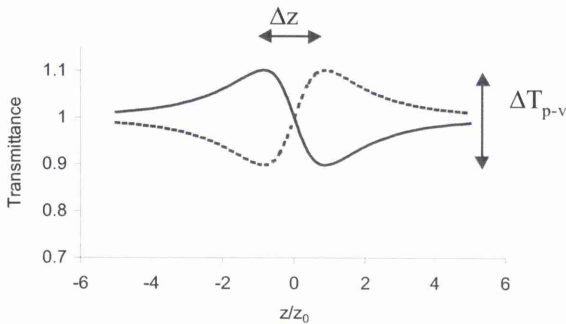


Figure 6-10: Ratio z-scan curve - dividing closed by open isolates the nonlinear refraction. Solid line shows negative, self-defocusing and dotted line shows positive, self-focusing nonlinearity

As well as instantly indicating the sign of the refraction, the ratio scan allows the strength of the nonlinear phase shift to be determined from the transmission difference between the peak and the trough. $\Delta T_{p-v} \sim 0.406 |\Delta\Phi|$ for small apertures. Finally the z-separation of the peak and trough, Δz , relative to the Rayleigh range, z_0 , is a function of order of the refractive process; $1.7z_0$ for a third order $\chi^{(3)}$ or $1.2z_0$ for a cascaded effective fifth order $\chi^{(5)}$ which were both anticipated for these measurements.

The refractive index change, Δn , is related to the nonlinear phase shift by the expression:

$$\Delta\Phi = \frac{2\pi}{\lambda} L \Delta n \quad \text{Equation 6-12}$$

where L is the sample length and λ the wavelength.

6.4.2 Thick samples

Standard expressions have been derived to describe z-scan characteristics and were used to generate the plots in the above figures. For example, the ratio scan is given by:

$$T(z, \Delta\Phi) = 1 - \frac{4\Delta\Phi x}{(x^2 + 9)(x^2 + 1)} \quad \text{Equation 6-13}$$

where $x = z/z_0$. However it should be realised that these expressions have only been derived for third order $\chi^{(3)}$ processes ($\Delta z_{p-v}=1.7z_0$) Similar relations do not appear to be available for fifth order processes such as free-carrier plasma refraction, which is unfortunate.

An implicit assumption in the z-scan analysis is that the refraction is in the “external self-action” regime, where the sample is optically thin and the beam diameter does not change significantly within the sample. For this to be valid the phase shift cannot typically exceed ~ 1 . This constrains the peak and the trough transmission changes to be less than $\pm 20\%$.

Once this condition is exceeded higher order terms in the z-scan analysis must be introduced.

Thick sample conditions have been studied by several groups [41,42]. Higher orders terms in the ratio z-scan give rise to an expanded expression:

$$T_{thick}(z, \Delta\Phi) = 1 - \frac{4\Delta\Phi}{(x^2 + 9)(x^2 + 1)} \left[x + \frac{(5 - 3x^2)\Delta\Phi}{(25 + x^2)} + \frac{8x(11 - x^2)\Delta\Phi^2}{(25 + x^2)(49 + x^2)} \right] \quad \text{Equation 6-14}$$

This is shown below compared with the simpler expression of Equation 6-13 for a large phase shift $\Delta\Phi = -2$:

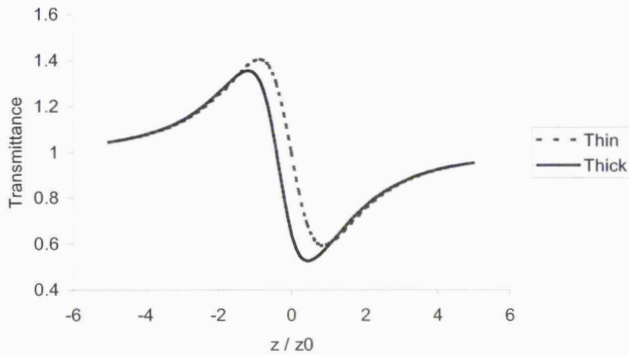


Figure 6-11: Comparison of ratio z-scans for thin sample and thick sample expressions with a phase change $\Delta\Phi = -2$

The effect of the beam changing within the thick sample is a loss of symmetry both in z and in transmittance. The plot shifts towards negative z, i.e. towards the source. The peak transmittance is suppressed whereas the dip of trough increases. These analyses have again been limited to third order processes and so can not be directly applied in this case. However the general trends are worth noting.

6.4.3 Experimental arrangement

The closed aperture measurements followed on from the open aperture measurements described in Chapter 5 and hence used the same optical arrangement up to the sample:

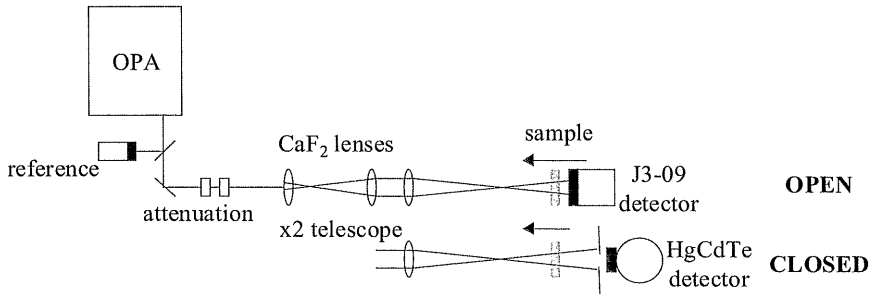


Figure 6-12: Experimental arrangement for open and closed aperture z-scan measurements

To recap, an expanding telescope doubled the beam diameter up to ~ 6 mm before focusing to provide a greater variation of intensity over the scan. A calcium fluoride lens of 100 mm focal length focused the beam onto the sample. For open aperture scans the sample was mounted on the front of a J3-09 pyroelectric detector and the whole assembly scanned through focus using a motorised translation stage.

For closed aperture scans a cooled HgCdTe detector was placed 20 cm behind focus and only the sample was moved. At the detector position the normal, linear beam was ~ 20 mm diameter. The 100 μm detector element size was used as an effective aperture with a transmission of 1.5%. Considerable care was taken that the sample z-position was preserved between the open and closed aperture runs. The transmission changes were large enough that even a slight change of position between the two conditions would invalidate the eventual ratio result.

6.4.4 Results and discussion

Closed aperture scans measured at 4 μm wavelength are below for a range of energies:

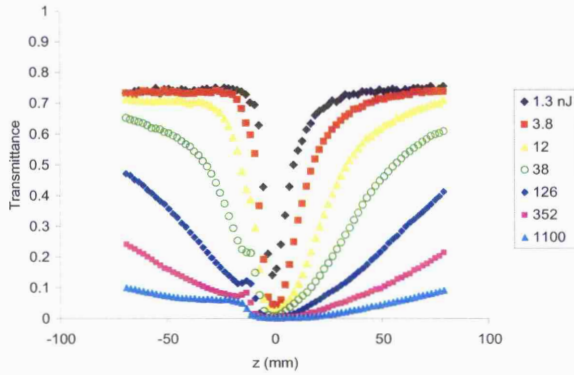


Figure 6-13: Closed aperture z-scans of InAs at $4 \mu\text{m}$ wavelength for a range of energies. At lower energies the loss of symmetry was an early sign of refraction occurring. At higher energies $> 12 \text{ nJ}$ a peak became apparent on the absorptive dip in front of focus suggesting a negative, defocusing effect.

The ratio scans are shown split onto two charts for clarity:

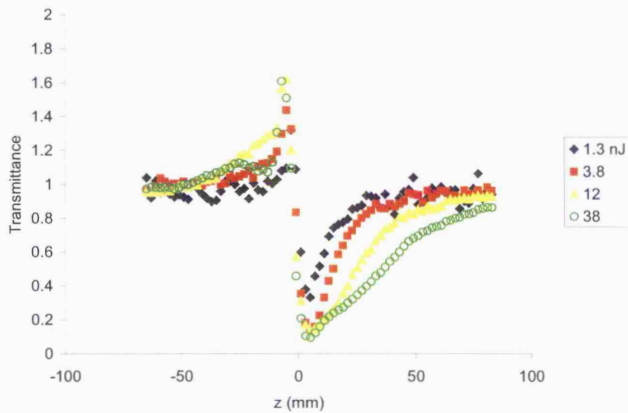


Figure 6-14: Ratio z-scans of InAs at $4 \mu\text{m}$ wavelength for low energies

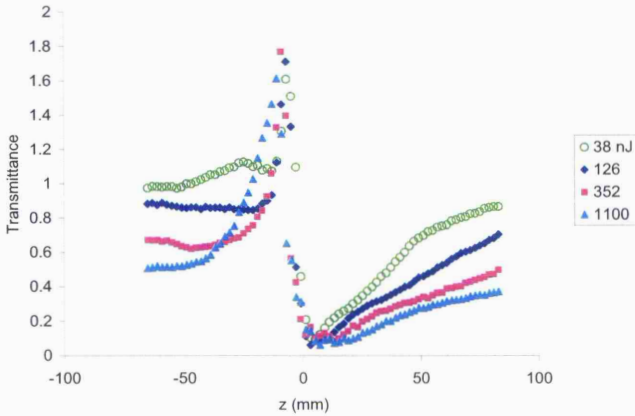


Figure 6-15: Ratio z-scans of InAs at $4 \mu\text{m}$ wavelength for higher energies

A peak-trough trace indicative of negative refraction was evident even at the lowest resolvable energy. At higher energies the peak-trough pattern remained but the symmetry became distorted and transmittance at the edges diverged from unity indicating refraction was occurring even at the extremes.

Similar results were obtained at the other two wavelengths of $4.75 \mu\text{m}$ and $5.5 \mu\text{m}$, shown below.

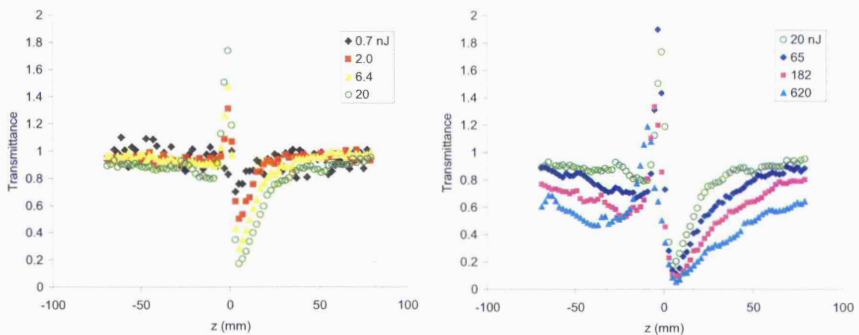


Figure 6-16: Ratio z-scans of InAs at $4.75 \mu\text{m}$ wavelength

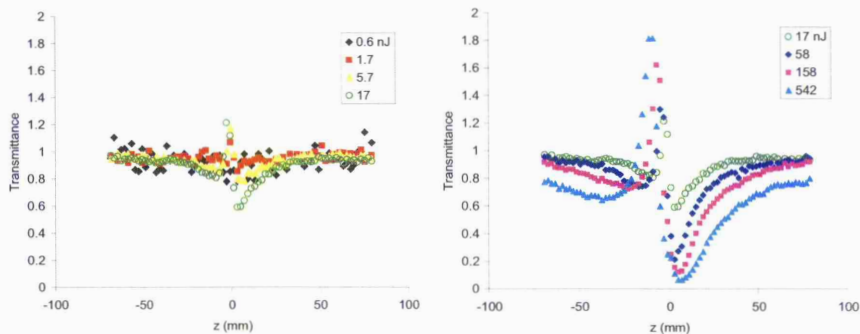


Figure 6-17: Ratio z-scans of InAs at 5.5 μm wavelength

All the scans were dominated by peak-trough patterns indicative of the negative, defocusing free carrier plasma. The peak-trough transmission differences, ΔT_{p-v} , were large even for low energies indicating corresponding large phase changes within the samples. Asymmetries in the traces were consistent with the sample being in the “thick” regime for most measurements.

Immediate comparison across the three wavelengths could not be made based simply on energies since several other parameters such as spot size, pulse length and sample transmission all changed as well. A suitable metric for comparison was deduced to be the peak induced free carrier density, ΔN . This was calculated using the expression previously derived in Chapter 5 from the assumption that no carrier recombination takes place during the ultrashort pulse duration:

$$\Delta N = \frac{\sqrt{\pi} \beta t_0 I_0^2}{2\sqrt{2} \hbar \omega} \quad \text{Equation 6-15}$$

where β is the two-photon absorption coefficient, t_0 the pulse duration (Hwe^{-1}M), ω the radiation frequency and I_0 the peak intensity given by the relation:

$$I_0 = \frac{2E}{\pi\sqrt{\pi} t_0 r_0^2}$$

Equation 6-16

where E is the pulse energy, t_0 the HWe⁻¹M pulse length and r_0 the spot size at focus.

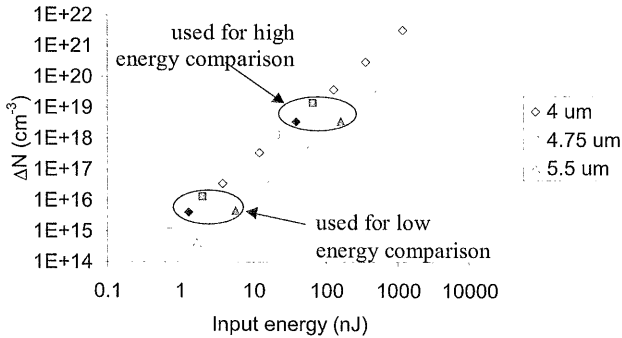


Figure 6-18: Peak carrier densities at focus of z-scans
Solid points are used for later comparison

The carrier densities at 4.0 and 4.75 μm were comparable because the parameters were all similar. The 5.5 μm values were noticeably lower because the beam size was larger and pulse length longer.

The carrier densities resulting from this were clearly overestimates and unrealistic since recombination, saturation and beam spreading were all neglected. However the calculation enabled comparable points to be identified. Measurement points with similar carrier densities should exhibit similar magnitudes of plasma refraction so differences could be attributed to ultrafast n_2 refraction. Two sets of data for comparison were chosen corresponding to the solid points in Figure 6-18. The first set of data was at low energy:

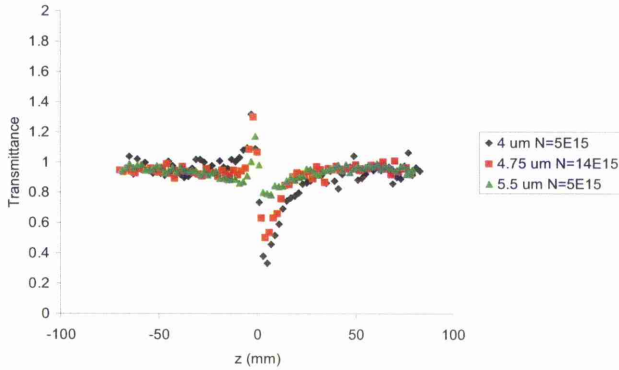


Figure 6-19: Ratio z-scans at comparable carrier densities for low energy

The 5.5 μm data showed the smallest variation, though still characteristic of negative refraction. This was consistent with the ultrafast n_2 being positive at this wavelength and partially suppressing the negative plasma refraction. At 4.75 μm there should have been very little ultrafast contribution and refraction should have come almost entirely from the free carrier plasma. The 4 μm refraction should have been strengthened by the now negative ultrafast contribution. The 4 μm scan appears comparable to 4.75 μm despite being at a lower carrier density, suggesting it had been enhanced.

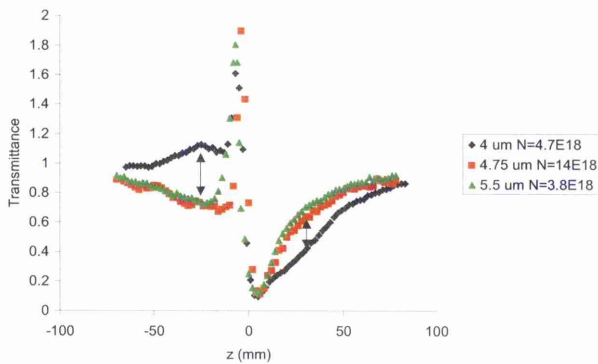


Figure 6-20: Ratio z-scans at comparable carrier densities for high energy

Here the effects of the ultrafast component were clearer, highlighted by the arrows. Both 5.5 and 4.75 μm wavelengths showed distinct dips prior to the plasma peak in front of focus. This could be attributed to a trough from the positive ultrafast n_2 contribution. On the other side of focus the corresponding peak of the n_2 brought the trace back to unity more rapidly. The 4 μm wavelength show opposite effects in agreement with the sign change of n_2 . An additional peak of the same sign as the plasma was seen before focus, and past focus the refraction was enhanced by a further trough.

6.4.5 Free-carrier refractive cross-sections

Refractive cross sections were calculated from the ratio z-scans for each wavelength. Data from the lowest possible energies was used in order to minimise the ΔT_{p-v} . The results are shown in Table 6-1.

Wavelength (μm)	Input energy (nJ)	ΔN at focus ($\times 10^{15} \text{ cm}^{-3}$)	ΔT_{p-v}	$\Delta\Phi$	Δn ($\times 10^{-3}$)	σ_r ($\times 10^{-19} \text{ cm}^3$)
4	1.3	4	1	-2.5	-1.6	-3.9
4.75	0.7	1.6	0.3	-0.74	-0.56	-3.5
5.5	5.7	4	0.3	-0.74	-0.65	-1.5

Table 6-1: Refractive cross sections determined from low energy ratio z-scans

Even at the lowest energy it can be seen that the induced phase change at 4 μm is excessive and the thin sample condition was not satisfied. However the deduced refractive cross-sections compared well with the predictions earlier in this Chapter:

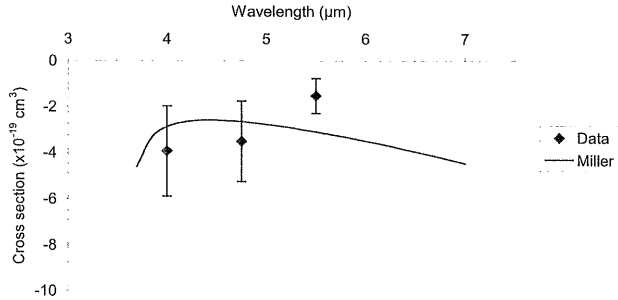


Figure 6-21: Comparison of refractive cross-sections measured with z-scans and predictions of Miller free-carrier refraction

The results are in agreement with additional n_2 effects with an enhancement at 4 μm and reduction at 5.5 μm . The result at 4.75 μm could be caused by the spectral width of the OPA output. Preferential absorption at higher energies, shorter wavelengths would result in a negative n_2 contribution. The error bars reflect uncertainty in both the measured z-scan transmission results as well as the calculated change in carrier density.

At higher energies the refractive cross-sections became much smaller which can be attributed to saturation of the z-scan measurement technique. In an attempt to reduce the sensitivity of the z-scan a larger, 2mm element size HgCdTe detector was used. This proved unsuccessful giving minimal reduction on the peak-trough heights. A longer focal length was also considered but the sample stage travel was limited to 200mm. The next best way to reduce the z-scan sensitivity would be to use a thinner sample.

6.5 Summary of chapter

In this chapter the nonlinear refraction associated with two-photon absorption has been studied. Self-defocusing through free carrier plasma refraction is shown to be the dominant fluence-limiting process in semiconductors. Additional contributions from band-filling (Dynamic Burstein-Moss shift) and bandgap normalisation are also considered through

several different expressions. Ultrafast, n_2 contributions must also be considered with the ultrashort, high intensity pulses. The sign and magnitude of the ultrafast contribution is shown to be dependent on the wavelength and may enhance or suppress the free carrier refraction accordingly.

A review of previous nonlinear refraction in narrow-gap semiconductors and an overview of the z-scan technique are given.

Z-scan results are presented for InAs at three different wavelengths. The method was found to be extremely sensitive and showed saturation effects even at low energies. All the scans were dominated by a negative, defocusing component in agreement with the free-carrier predictions. Comparing similar scans at different wavelengths showed evidence of an n_2 contribution. Refractive cross-sections were in general agreement with predictions.

6.6 References

- 1 E.W. Van Stryland, in *Forty Seventh Scottish Universities Summer School in Physics*, edited by A. Miller and DM Finlayson (IOP, St Andrews University, 1995), p. 15.
- 2 M. Sheik-Bahae and E.W. Van Stryland, in *Semiconductors and semimetals* (1999), Vol. 58.
- 3 BR Bennett, RA Soref, and JA Del Alamo, "Carrier induced change in refractive index of InP, GaAs, and InGaAsP," *IEEE J Quant Elec* **26**, 113 (1990).
- 4 O Madelung, in *Landolt-Bornstein - Numerical Data and Functional Relationships Science and Technology*, edited by O Madelung and M Schulz (Springer-Verlag, Berlin, 1987), Vol. 22a Semiconductors - Intrinsic properties of Group IV elements and II-V, II-VI and I-VII compounds, p. 117.
- 5 PP Paskov and LI Pavlov, "Calculation of the carrier-induced refractive index change in InSb," *Appl Phys B* **54**, 113 (1992).
- 6 PP Paskov, "Carrier-induced change in the refractive index of InAs(1-x)Sbx," *Solid State Comm* **82**, 739 (1992).
- 7 PP Paskov, "Refractive indices of InSb, InAs, GaSb, InAsSb and InGaSb: effects of free carriers," *J Appl Phys* **81** (4), 1890 (1997).
- 8 DH Auston, S McAfee, CV Shank, EP Ippen, and O Teschke, "Picosecond spectroscopy of semiconductors," *Solid State Electron* **21**, 147 (1978).
- 9 J. Wang, M. Sheik-Bahae, A.A. Said, D.J. Hagan, and E.W. Van Stryland, "Time resolved z-scan measurements of optical non-linearities," *J Opt Soc Am B* **11**, 1009 (1994).

- 10 E.W. Van Stryland, H. Vanherzeele, M.A. Woodall, M.J. Soileau, A.L. Smirl, S. Guha, and Boggess T.F., "Two-photon absorption, nonlinear refraction, and optical limiting in semiconductors," *Opt Eng* **24**, 613 (1985).
- 11 DAB Miller, SD Smith, and BS Wherrett, "The microscopic mechanism of third-order optical nonlinearity in InSb," *Opt Commun* **35** (2), 221 (1980).
- 12 M. Sheik-Bahae, D.J. Hagan, and E.W. Van Stryland, "Dispersion and band-gap scaling of the electronic Kerr effect in solids associated with two-photon absorption," *Phys Rev Lett* **65**, 96 (1990).
- 13 CKN Patel, P Fluery, R Slusher, and H Frisch, "Multiphoton plasma production and stimulated recombination radiation in semiconductors," *Phys Rev Lett* **16**, 971 (1966).
- 14 CKN Patel, R Slusher, and P Fluery, "Optical nonlinearities due to mobile carriers in semiconductors," *Phys Rev Lett* **17**, 1011 (1966).
- 15 DAB Miller, MH Mozolowski, A Miller, and SD Smith, "Nonlinear optical effects in InSb with a cw CO laser," *Opt Comm* **27** (1), 133 (1978).
- 16 D. Weaire, B.S. Wherrett, D.A.B. Miller, and SD Smith, "Effect of low-power nonlinear refraction on laser-beam propagation in InSb," *Opt Lett* **4**, 331 (1979).
- 17 TS Moss, "Theory of intensity dependence of refractive index," *Phys Status Solidi (B)* **101**, 555 (1980).
- 18 DAB Miller, CT Seaton, ME Prise, and SD Smith, "Band-gap-resonant nonlinear refraction in III-V semiconductors," *Phys Rev Lett* **47**, 197 (1981).
- 19 JR Hill, G Parry, and A Miller, "Non-linear refractive index changes in CdHgTe at 175K with 10.6um radiation," *Opt Comm* **43** (2), 151 (1982).
- 20 M. Sheik-Bahae, A.A. Said, T.H. Wei, D.J. Hagan, and E.W. Van Stryland, "Sensitive measurement of optical nonlinearities using a single beam," *IEEE J Quant Elec* **26**, 760 (1989).
- 21 DAB Miller and SD Smith, "Two beam optical signal amplification and bistability in InSb," *Opt Commun* **31**, 101 (1979).
- 22 DAB Miller, SD Smith, and AM Johnston, "Optical bistability and signal amplification in a semiconductor crystal: applications of new low power nonlinear effects in InSb," *Appl Phys Lett* **35**, 658 (1979).
- 23 DAB Miller, SD Smith, and C.T. Seaton, "Optical bistability in semiconductors," *IEEE J Quant Elec* **17**, 312 (1981).
- 24 A Miller, G Parry, and R Daley, "Low power nonlinear fabry-perot reflection in CdHgTe at 10um," *IEEE J Quant Elec* **QE-20** (7), 710 (1984).
- 25 D. Craig, M.R. Dyball, and A. Miller, "Thermally induced optical bistability in CdHgTe," *Opt Commun* **54** (6), 383 (1985).
- 26 CD Poole and E Garmino, "Optical bistability at the band gap in InAs," *Appl Phys Lett* **44**, 363 (1984).
- 27 CD Poole and E Garmino, "Nonlinear refraction at the absorption edge in InAs," *Opt Lett* **9** (8), 356 (1984).
- 28 CD Poole and E Garmino, "Bandgap resonant optical nonlinearities in InAs and their use in optical bistability," *IEEE J Quant Elec* **QE-21**, 1370 (1985).
- 29 AK Kar, JGH Mathew, SD Smith, B Davis, and W Prettl, "Optical bistability in InSb at room temperature with two-photon excitation," *Appl Phys Lett* **42**, 334 (1983).
- 30 W Ji, AK Kar, JGH Mathew, and AC Walker, "Quasi-cw optical bistability in InSb at room temperature," *IEEE J Quant Electron* **QE-22**, 369 (1986).

- 31 JGH Mathew, AK Kar, NR Heckenberg, and I Galbraith, "Time resolved self-defocusing in InSb at room temperature," *IEEE J Quant Electron* **QE-21** (1), 94 (1985).
- 32 JGH Mathew, D Craig, and A Miller, "Optical switching in CdHgTe etalon at room temperature," *Appl Phys Lett* **46**, 128 (1985).
- 33 D Craig, "Two photon absorption induced optical bistability in CdHgTe at room temperature," *IEEE J Quant Elec* **21**, 1363 (1984).
- 34 D. Craig, A. Miller, J.G.H. Mathew, and A.K. Kar, "Fast optical switching and bistability in room temperature CdHgTe at 10.6 μ m," *Infr Phys* **25**, 289 (1985).
- 35 S. Guha, E.W. Van Stryland, and M.H. Soileau, "Self-defocusing in CdSe induced by charge carriers created by two-photon absorption," *Opt Lett* **10**, 285 (1985).
- 36 M. Sheik-Bahae and H.S. Kwok, "Picosecond CO₂ laser-induced self-defocusing in InSb," *IEEE J Quant Elec* **23**, 1974 (1987).
- 37 M. Sheik-Bahae, D.C. Hutchings, D.J. Hagan, M.H. Soileau, and E.W. Van Stryland, in *Laser Induced Damage in Optical Materials 1990, Proceedings of SPIE*, edited by HE Bennett, L.L. Chase, A. H. Guenther et al. (1991), Vol. 1441.
- 38 M. Sheik-Bahae, D.C. Hutchings, D.J. Hagan, and E.W. Van Stryland, "Dispersion of bound electronic nonlinear refraction in solids," *IEEE J Quant Elec* **27**, 1296 (1991).
- 39 A.A. Said, M. Sheik-Bahae, D.J. Hagan, T.H. Wei, J. Wang, J. Young, and E.W. Van Stryland, "Determination of bound-electronic and free-carrier nonlinearities in ZnSe, GaAs, CdTe and ZnTe," *J Opt Soc Am B* **9**, 405 (1992).
- 40 M. Sheik-Bahae, A.A. Said, and E.W. Van Stryland, "High sensitivity, single beam n₂ measurements," *Opt Lett* **14**, 955 (1989).
- 41 M. Sheik-Bahae, A.A. Said, D.J. Hagan, M.J. Soileau, and E.W. Van Stryland, "Nonlinear refraction and optical limiting in thick media," *Opt Eng* **30**, 1228 (1991).
- 42 PB Chapple, J Staromlynska, JA Hermann, and TJ McKay, "Single-beam z-scan: Measurement techniques and analysis," *J Nonlinear Opt Phys and Mat* **6**, 251 (1997).

Chapter 7 - Pump-probe experiment

7.1 Introduction

Optical excitation across the band gap generates non-equilibrium populations of electrons and holes. The carrier distribution reverts back towards equilibrium through various processes including relaxation, recombination, diffusion and drift. The evolution of the carriers will clearly be important in determining the temporal characteristics of a device that are in turn driven by the desired application. Low threshold devices such as continuous wave (CW) lasers and infrared detectors need long carrier lifetimes. Laser Q-switches or mode-lockers and ultrafast radiation detectors require fast recovery.

The requirements of optical switching are varied. For high bandwidth, telecommunication type uses, the lifetimes must be short to ensure recovery between pulses. For lower bandwidth, reduced intensity switching a long lifetime is desirable such that an active state can be maintained throughout a long pulse.

There were several advantages of using the OPA-DFM system to study carrier dynamics. The use of two-photon absorption to generate the free carriers meant that good penetration through a thick sample could be achieved. Also the same sub-bandgap wavelength could then probe the resultant free carrier absorption. The ultrashort pulse meant that the carrier generation was effectively instantaneous and took place prior to any recombination. The induced change in carrier density was a step function, and subsequent evolution could be probed free from complications of ongoing generation. This would remain true except for very high intensities generating carrier densities ($\sim 10^{19} \text{ cm}^{-3}$) that were sufficient to drive the Auger recombination time to sub-ps values. Evidence from the z-scan results suggested

that refraction and beam spreading prevented the intensity ever getting high enough to reach these levels.

7.2 Relaxation processes

The excess free carriers generated by optical absorption have increased momentum and higher effective temperature with respect to the surrounding lattice. Relaxation occurs through a number of processes on short timescales. Useful reviews of semiconductor relaxation processes, laser sources and techniques for measurement have been published by Othonos and Elsaesser [1,2].

The relaxation can be divided into several processes as shown in Figure 7-1. Each process has a characteristic time and they typically occur simultaneously.

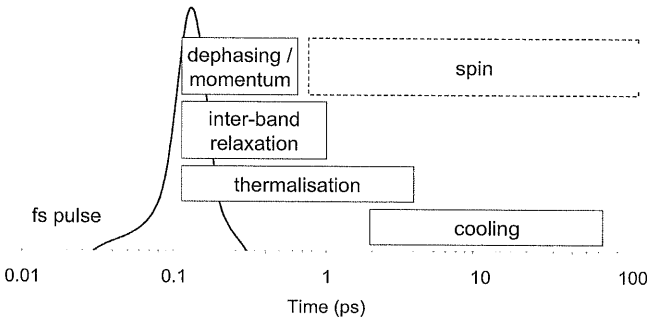


Figure 7-1: Relaxation processes initiated by ultrafast excitation of carriers

Excitation by monochromatic coherent radiation will produce a distribution that is narrow in energy and momentum, with phase related to the polarisation. Momentum randomisation and dephasing occurs through carrier-carrier scattering collisions within a few tens of femtoseconds.

Circularly polarised light can be used to excite carriers of a particular spin preferentially according to selection rules from the light and heavy hole bands. Spin relaxation has been

studied in “bulk” 3 μm thick layers of InAs where a lifetime of 19 ps was observed [3]. Heavy n-type doping has been shown to increase this lifetime to over 1 ns due to a change of relaxation mechanism [4].

Interband relaxation refers to transitions between the split-off or light hole band down to the ground state heavy hole band and is mainly concerned with p-type doped material. Theoretical modelling has estimated this to occur on short femtosecond timescales through optical phonon emission [5].

Carrier thermalisation is the relaxation of the carriers into a quasi-equilibrium Fermi-Dirac distribution. Energy is transferred between carriers predominately via scattering. The distribution can then be characterised by a Fermi energy and effective temperature that is typically higher than the surrounding lattice.

The hot carrier distribution cools by exchange of energy with the surrounding lattice through emission of optical phonons and subsequent transfer to acoustic phonons. For small carrier injections and low excess temperatures the process is unimpeded and cooling occurs rapidly over a few ps. At higher carrier densities and temperatures a bottleneck can arise at the acoustic phonon stage. The temperature of the optical phonon distribution then rises rapidly to match the carrier temperature and a substantial slowing in the cooling is observed to ~ 100 ps. This “hot-phonon” saturated cooling effect was originally observed in germanium [6,7] but has also arisen in a variety of other materials [8-10].

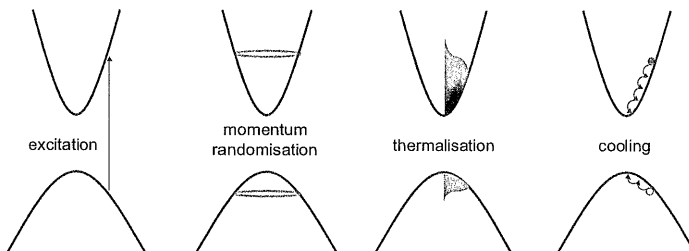


Figure 7-2: Various carrier relaxation processes following optical excitation

7.3 Recombination processes

7.3.1 Auger recombination

Auger recombination is the complementary process to impact ionisation. An electron and hole recombine transferring their excess energy and momentum to a third carrier. There are several variants depending on the band structure and type of third carrier. For n-type material, the CHCC or Auger-1 process is expected to dominate where the energy is transferred to an electron in the conduction band. There may also be CHLH Auger-7 processes where heavy-to-light-hole band transitions take place, though this is more common in p-type material. Finally the transition of a hole to the split-off band can take place through the CHSH process. This is expected to be enhanced in InAs because of the resonance in energy between the band gap, $E_g = 0.35$ eV and split-off energy, $E_{so} = 0.37$ eV [11].

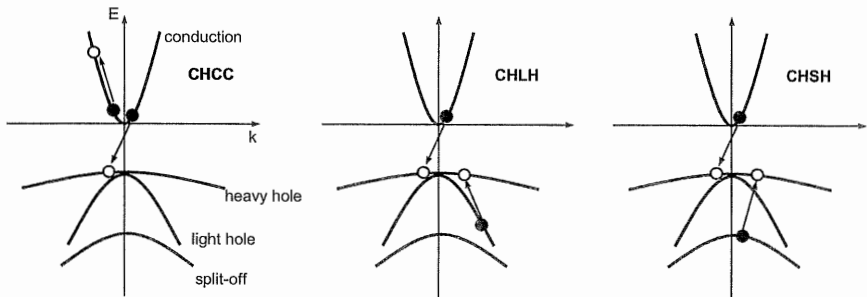


Figure 7-3: Normal Auger recombination processes

In contrast, the split off energy in InSb is ~ 4 times larger than the band gap so the CHSH process plays no part. As a result the Auger rate in InAs is comparable to that of InSb despite the larger bandgap.

In addition to these “normal” Auger processes, there are more complicated variants which include phonon, exciton and trap assistance. However these are expected to have minimal

contribution in the narrow-gap InAs. Further information is available in book sections by Blakemore and Ridley [12,13].

Since the process involves three particles, the Auger recombination rate scales approximately as the third power of the carrier densities. The Auger lifetime therefore shows a quadratic dependence:

$$\frac{1}{\tau_{aug}(t)} = \gamma N(t)^2 \quad \text{Equation 7-1}$$

where γ is the Auger coefficient (cm^6s^{-1}). Auger is the dominant recombination mechanism at high carrier densities.

Auger was first considered theoretically by Beattie and Landsberg [14]. Various predictions have been made for InAs with improvements arising from the influence of the CHSH process, degenerate carrier populations, non-parabolic bands and carrier screening [11,15-17]. A median value of $\gamma \sim 6 \times 10^{-27} \text{ cm}^6\text{s}^{-1}$ agrees well with the spread of experimentally observed lifetimes [18-21]

Auger recombination may enter a different regime at high carrier densities. Under such degenerate conditions the lifetime depends inversely on the carrier density and an alternative Auger coefficient is observed (cm^3s^{-1}) [22,23]. This effect has been seen in InAs/Ga_{1-x}In_xSb quantum wells for carrier densities greater than $\sim 10^{18} \text{ cm}^{-3}$ [20,24].

7.3.2 Shockley-Read-Hall recombination

Shockley-Read-Hall (SRH) recombination is a process whereby electrons and hole recombine through trap levels situated within the forbidden energy gap [25,26]. Excess energy is released by multiphonon emission. The energy traps arise from physical defects, foreign objects and structural flaws within the crystal.

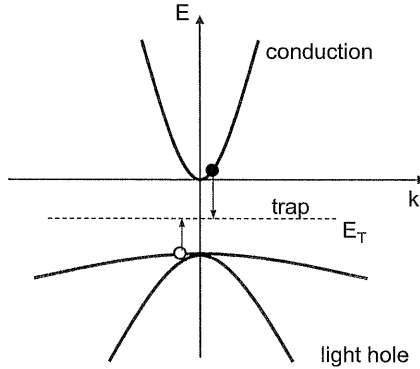


Figure 7-4: Shockley-Read-Hall trapping recombination

The SRH recombination lifetime is given by:

$$\tau_{SRH} = \frac{\tau_p (\Delta n + n_o + n_i e^{(E_T - E_F)/kT}) + \tau_n (\Delta n + p_o + n_i e^{(E_T - E_F)/kT})}{n_o + p_o + \Delta n} \quad \text{Equation 7-2}$$

where n_o and p_o are the equilibrium carrier densities, E_T and E_F the trap and Fermi energy levels for the intrinsic material respectively, and $\Delta n = \Delta p$ the excess carrier concentration. τ_p and τ_n are defined as:

$$\tau_{p/n} = \frac{1}{\sigma_{p(n)} v_{th} N_T} \quad \text{Equation 7-3}$$

where v_{th} , N_T and $\sigma_{p(n)}$ denote the thermal velocity, trap density and capture cross sections for hole (electron) traps. SRH is most efficient with trap levels near the centre of the band gap since thermal re-emission of carriers can compete when traps are close to either band. For high injection densities the lifetime becomes independent of carrier densities:

$$\tau_{hl} = \tau_n + \tau_p \quad \text{Equation 7-4}$$

SRH lifetimes of only ~10 ns were reported in InAs epilayers by Lindle et al [19]. It was observed that these were probably reduced by the effect of lattice mismatch with the AlSb buffer layer on the GaAs substrates. The effects of bulk and surface interface defects on

SRH lifetimes was investigated by Vodopyanov et al who used proton bombardment to introduce variable levels of damage defects into InAs epilayers [27].

A complex calculation of SRH lifetimes in bulk InAs has been performed recently by Krishnamurthy and Berding [28]. Point defects densities and trap energy levels were calculated from a dynamic model of the crystal growth process. The dominant defect was found to arise from indium antisites with predicted density of $\sim 5 \times 10^{14} \text{ cm}^{-3}$ and trap level 0.23 eV above the valence band. Lifetimes of 2 and 71 ns were obtained for electrons and holes respectively for the limiting cases of highly doped samples. Good agreement was observed with two-photon pump probe experimental data taken using a doubled CO₂ laser where a room temperature lifetime of 135 ns was measured [29].

7.3.3 Radiative recombination

Radiative recombination is the reverse of optical absorption across the band gap. An electron and hole recombine and release the excess energy by emission of a photon, depicted in Figure 7-5.

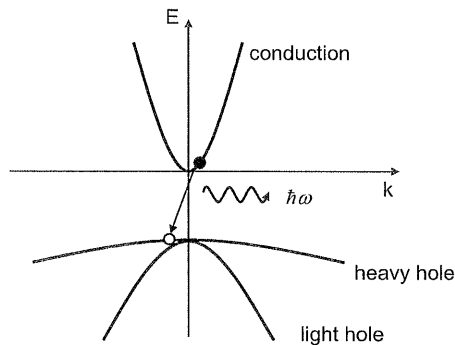


Figure 7-5: Radiative recombination

The recombination time will be dependent on the occupation probabilities and Fermi energies of the electron and hole distributions. With InAs the large difference in effective

mass between the conduction and valence bands means that there is a 77-fold difference in the respective density of states. Despite the conduction band becoming highly degenerate with Fermi energy greater above the band gap, the hole-occupational probability is unlikely to exceed 0.1 [30]. For this reason a radiative lifetime of 3 ns for InAs calculated using the radiative treatment of Matsuesue is not completely valid since it assumes completely degenerate statistics [31]. Partially-degenerate statistics will result in a longer lifetime and ~ 25 ns is quoted by Vodopyanov et al for InAs epilayers [18]. However no justification is given for this estimate and it plays no part in the analyses of their results, which are all concerned with much shorter timescales.

Significantly longer lifetimes up to 1 μ s observed in bulk InAs have been attributed to radiative recombination [32-34]. The theory of Roosbroeck and Shockley [35] was used to show good agreement; however, this assumed small departures from equilibrium, i.e. non-degenerate conditions. The lifetimes appear to saturate at ~ 200 ns for carrier densities above 10^{16} cm^{-3} [33]; however Auger recombination quickly dominates.

More recent studies of recombination in InAs have neglected radiative recombination and concentrated on SRH and Auger [19,36].

7.3.4 Carrier rate equation

The free carrier density and recovery after a pulse in the presence of SRH and Auger recombination is thus described by the rate equation:

$$\frac{\partial N(t)}{\partial t} = -\frac{N(t)}{\tau_{srh}} - \gamma N(t)^3 \quad \text{Equation 7-5}$$

where τ_{srh} (s) is the SRH lifetime and γ (cm^6s^{-1}) is the Auger recombination coefficient.

The solution to this expression has the form:

$$N(t) = \frac{n_0}{\sqrt{(1 + \gamma_{aug} n_0^2 \tau_{srh}) e^{2t/\tau_{srh}} - \gamma_{aug} n_0^2 \tau_{srh}}}$$

where n_0 is the initial excess carrier density after excitation. The generalised form of this function is shown in illustrating three cases.

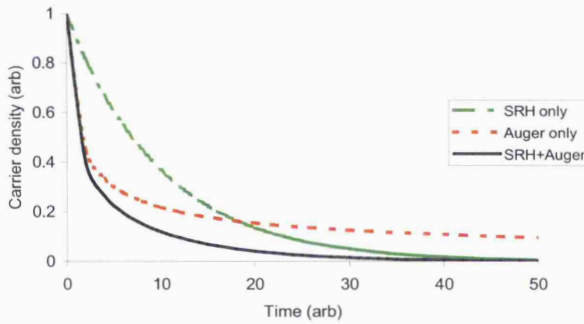


Figure 7-6: Generalised examples of recombination curves for varying SRH and Auger contributions

It can be seen that the combined action of SRH plus Auger gives the most effective recombination process. Auger causes the initial rapid drop from high carrier densities, after which Shockley-Read-Hall takes over. The Auger lifetime as a function of carrier density based on the median value of $\gamma = 6 \times 10^{-27} \text{ cm}^6 \text{ s}^{-1}$ is shown below:

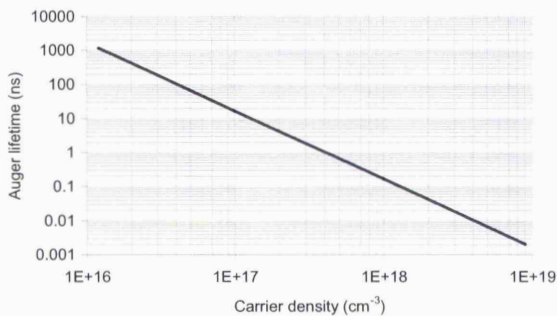


Figure 7-7: Auger lifetimes based on literature median value of $\gamma = 6 \times 10^{-27} \text{ cm}^6 \text{ s}^{-1}$

This shows that the carrier density must exceed $\sim 3 \times 10^{16} \text{ cm}^{-3}$ for the Auger process to become noticeable over a fixed SRH lifetime of $\sim 100 \text{ ns}$. Such carrier densities should be achievable with the OPA pulse. However it may be significant that this is an order of magnitude over the excess carrier density required for significant refraction from the free carrier plasma.

7.4 Pump-probe measurements

Induced carrier lifetimes and recombination were studied in room temperature InAs using a two-photon pump-probe experiment. The temporal resolution desired to study carrier dynamics was clearly beyond that of conventional detectors or electronics so optical techniques were required. The pump- or excite-probe is a well-known method. The optical beam is split into two parts: a high intensity pump to excite the sample and a low intensity probe. A delay is introduced between the two parts, often through a variable optical path length. The probe can measure the temporal evolution of processes within the sample through optical properties such as reflectivity, transmission, induced absorption, refraction and scattering. Spatial overlap is obviously required and the probe beam is usually made smaller than the pump.

The first application of a pump-probe experiment was by Shelton and Armstrong to measure relaxation dynamics in a Q-switching dye [37]. A review of various techniques has been published by Ippen and Shank [38]. Alternative methods that have been developed to study ultrafast optical dynamics include streak cameras, optical Kerr gating (fast optical switching) and parametric up-conversion / sum frequency mixing [1].

In the experiment the probe was used to measure the temporal transmission change. The propagation of the probe beam through the sample is described by:

$$\frac{dI_p}{dz} = -\beta_{pp} I_p^2 - \beta_{ep} I_e I_p - \sigma_a N I_p - \alpha I_p \quad \text{Equation 7-7}$$

where $I_{p/e}$ are the probe and excite intensities respectively, z the propagation direction, α and β are the linear and two photon absorption coefficients respectively, σ_a is the free carrier absorption cross section and N is the free carrier density arising from the 2PA of the excite beam.

The first term in Equation 7-7 represents conventional 2PA of the probe beam. Provided the intensity is kept low this can be neglected. The second extra term is also 2PA but represents the combined effect of the probe and pump beams. A different two photon absorption coefficient, β_{ep} , is used since the probe and pump may have different polarisations and / or wavelengths. Polarisation anisotropy and non-degenerate two-photon absorption have been predicted from full band calculations by Hutchings [39] and observed in some larger band-gap materials [40]. The final term in Equation 7-7 is linear absorption which can be neglected if the relative transmittance change is measured.

The nonlinear probe transmission is therefore mainly dependent on the free carriers generated by two-photon excitation.

$$\begin{aligned} T(t) &= e^{-L\alpha(t)} \\ &= e^{-L\sigma_a N(t)} \end{aligned} \quad \text{Equation 7-8}$$

where L is the sample length, α the free carrier absorption and σ_a (cm^2) the free carrier absorption cross section. The carrier density could be deduced from the optical absorption using the free carrier absorption cross section.

$$N(t) = \frac{-\ln[T(t)]}{L\sigma_a} \quad \text{Equation 7-9}$$

Choosing an appropriate cross section, σ_a becomes the main difficulty. Reported values cover a wide range from 4×10^{-18} [41] to $8 \times 10^{-16} \text{ cm}^2$ [42]. The cross section will also vary

with the carrier density, $\sigma_a(N)$, since transitions will be dependent on the occupation of states. This dependence has been inferred from transmission measurement of varying doped samples [43]. However, doping will result in different carrier distributions when compared to two photon excitation. Decreased free carrier absorption with short, <100 ps pulse lengths has also been observed [44,45].

Carrier recombination and optical transmittance are illustrated below for figures representative of what might be expected with InAs. The initial excess carrier density was $n_0 = 5 \times 10^{17} \text{ cm}^{-3}$, $\gamma = 6 \times 10^{-27} \text{ cm}^6 \text{ s}^{-1}$ and a median figure for the absorption was $\sigma_a = 2 \times 10^{-17} \text{ cm}^2$.

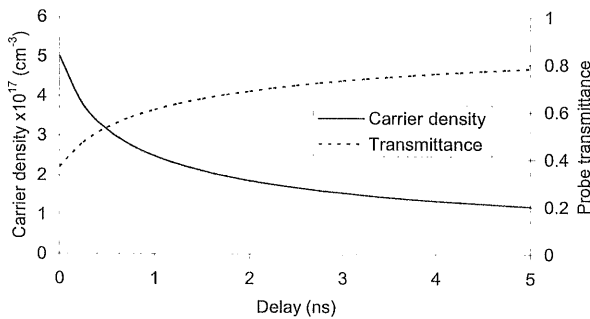


Figure 7-8: Carrier density and probe transmittance for parameters representative of InAs

7.4.1 Experimental arrangement

The experimental arrangement for the pump-probe measurements is shown below.

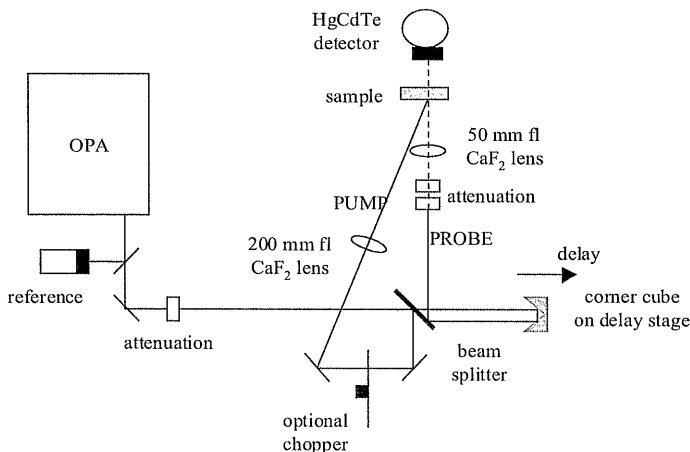


Figure 7-9: Experimental arrangement for two photon pump-probe

The OPA output wavelength was $4\ \mu\text{m}$. A beamsplitter was used to create two beam paths. One path of constant length was focused on to the sample with a CaF_2 lens of long 200 mm focal length. The spot size at the sample was estimated to be $400\ \mu\text{m}$. With no additional attenuation this formed the pump.

The second, probe path was retro-reflected off a corner cube mounted on a 250 mm motorised translation stage. This provided a variable path such that the probe could be delayed up to 1.6 ns with respect to the pump. After a second reflection off the beamsplitter, the probe was focused on to the sample with a CaF_2 lens of short 50 mm focal length. This gave a smaller spot than the pump and ensured that only the centre portion of the pump-irradiated region was measured. Attenuation was also inserted so that the probe was typically 10 times lower in energy than the pump.

The pump and probe were accurately aligned using the vidicon camera such that their focused spots were coincident. A visible diode laser was used to provide visible beam paths enabling the sample to be accurately positioned at their confluence.

Probe transmission through the sample was monitored by a cooled HgCdTe photo-detector. The detector was initially positioned as close as possible to the sample without seeing stray pump signal. Changing this separation and use of a collecting lens was investigated experimentally.

Care was taken that the probe beam spot did not deviate through walk-off over the range of the translation stage. However beam divergence over the extra path did mean that some change in measured probe energy was observed even with the pump blocked. This was normalised out for each measurement.

The pump-probe overlap was optimised by inserting a chopper in the pump arm running at ~ 220 Hz. The lock-in amplifier for the probe was synchronised with the reference from the pump chopper and the delay stage moved until a signal was observed. This ensured that the observed signal on the probe was a direct result of the pump. The signal was maximised by carefully adjusting the sample position and pump alignment.

7.4.2 Results and discussion

An initial result from the pump probe experiments is shown below.

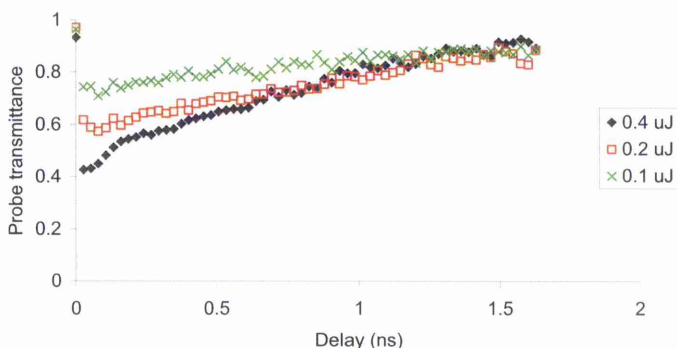


Figure 7-10: Initial result from pump-probe

The pump was clearly inducing a transmission drop in the sample with a rapid recovery to ~90% that was observable over the time delay covered by the translation stage. 0.4 μJ was the maximum energy achievable in the pump beam. The peak intensity of the pump at focus was 3 GWcm^{-2} and resultant pump transmission ~3%. Lower energies produced smaller peak changes in transmission but decayed to similar long delay transmission values. This was consistent with a two-stage decay process starting with a short, intensity dependent Auger lifetime and transferring to a long, fixed SRH lifetime. Results were variable and the alignment had to be re-optimised periodically to maintain a good signal. The leading edge of the signal was investigated over much reduced timescale. A sharp dip in transmittance was observed over the initial few hundred fs period, as shown below:

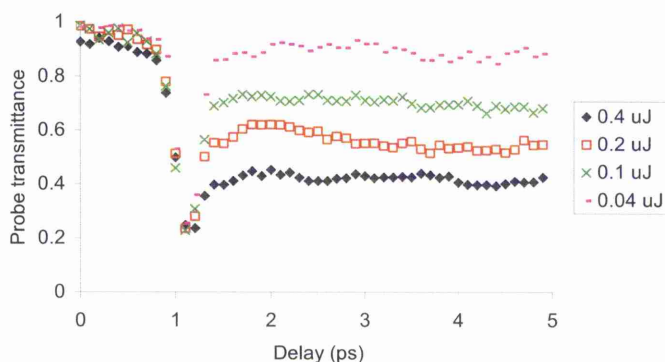


Figure 7-11: Leading edge of pump-probe on reduced timescale

The resonance spike is usually a coherent, autocorrelation type interaction between pump and probe commonly observed in pump-probe experiments [46]. The feature can arise from interference between the free-carrier plasma gratings generated by the two beams. This often results in energy being coupled from the stronger pump into the probe and an apparent increase in transmittance. However in this case it appeared energy was being transferred out of the probe, i.e. the transmission decreased. The effect can be explained by

considering the second term in Equation 7-7, $-\beta_{ep}I_pI_e$, where the two-photon absorption of the probe is enhanced by the presence of the intense excite pump. The normal approach of using cross polarisations would be ineffective at removing this feature since β_{ep} would still be finite.

The resonance had the effect of masking other sub-ps timescale features. As a result, no evidence of phenomena such as interband relaxation or thermalisation was observed which was slightly disappointing.

The origin of probe signal in the initial detector arrangement was a combination of free carrier absorption and refraction. Both were linearly dependent on carrier density, however only the free carrier absorption could be interpreted linearly through the transmission, as outlined above. To investigate the nature of the signal, the sample-to-detector separation was varied with results shown below:

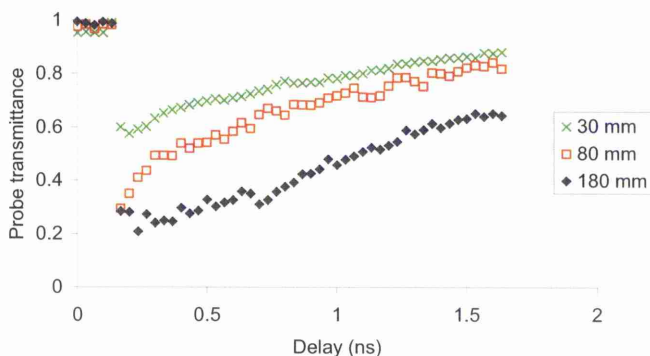


Figure 7-12: Effect of changing sample - detector separation with pump-probe

A pure absorptive effect would show no change as the separation was varied. The observed trend confirmed that refraction was contributing to the observed signal. To isolate the absorptive contribution a collecting lens was placed after the sample and the detector

positioned at the secondary focus. With the small size of the detector it was still possible that some of the probe was not collected. The refocused result is shown in Figure 7-13:

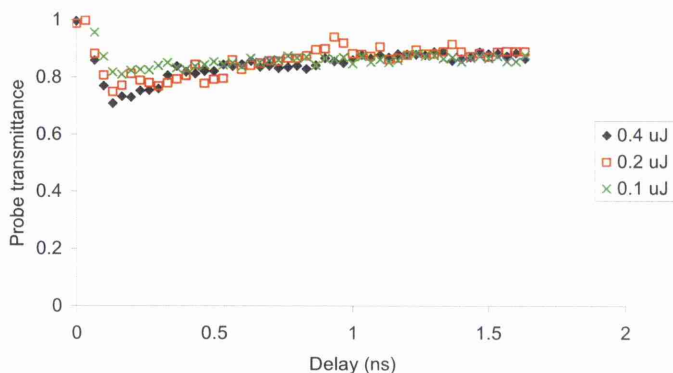


Figure 7-13: Probe beam refocused after sample to isolate absorption

This suggested the absorption accounted for, at most, half of the observed signal in the initial results. The transmission recovered to an almost flat level at around 88 %, with a long lifetime beyond the delay timescale of the translation stage, again indicative of SRH. A CW probe experiment would be a practical way of measuring this decay [29]. Some difference in the initial lifetimes was apparent suggesting that an Auger dependent state was being reached at the highest energy.

The induced absorption clearly took time to evolve with a leading edge decay of ~ 100 ps. This was not seen with the unfocused measurements from which it can be deduced that the refractive component was instantaneous. The time for the absorption to saturate is indicative of screened, hot-phonon decay. Free carriers are being generated at significant densities with very high excess energies. With the output centred at $4 \mu\text{m}$, the carriers are injected around 0.28 eV above the band gap. This equates to an effective temperature of over 3000 K. The decay is long because of the time to transfer this amount of excess heat into the lattice.

Further refinement of this measurement could be achieved with a larger area detector to ensure that the entire probe beam is collected. Finding such a detector is difficult since high sensitivity is still required to resolve the low energy probe.

As shown in Equation 7-9 the natural logarithm of the focused pump probe transmittance should be proportional to the induced carrier density when absorption is the primary mechanism. Values for the SRH lifetime, τ_{SRH} , and the initial Auger lifetime at the point of minimum transmission, τ_{aug0} , were obtained with a modified form of Equation 7-6 to the data:

$$N(t) = \frac{n_0}{\sqrt{\left(1 + \frac{\tau_{srh}}{\tau_{aug0}}\right) e^{2t/\tau_{srh}} - \frac{\tau_{srh}}{\tau_{aug0}}}} \quad \text{Equation 7-10}$$

where

$$\tau_{aug0} = \frac{1}{\gamma_{aug} n_0^2} \quad \text{Equation 7-11}$$

A resultant fit of Equation 7-10 is illustrated below for the highest energy:

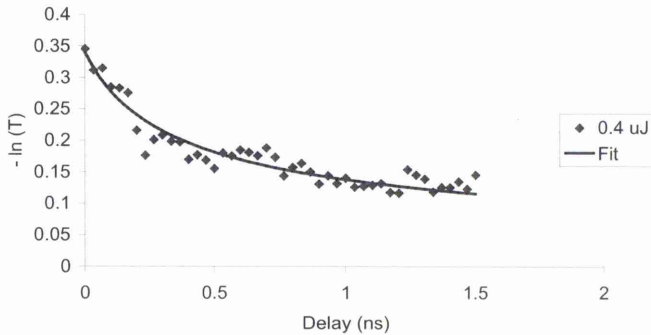


Figure 7-14: Fit of carrier evolution equation to experimental data

A summary of the lifetimes determined for each of the energies is in Table 7-1:

Energy (μJ)	SRH lifetime τ_{SRH} (ns)	Initial Auger lifetime at $t=0$ τ_{aug0} (ns)
0.1	65	2.8
0.2	5	0.8
0.4	62	0.4

Table 7-1: Lifetime fits from pump-probe absorption data

The long lifetime ~ 65 ns observed for the lowest and highest energies showed good agreement with the expected value for SRH. However the uncertainty on this value was quite high because of the short timescale over which data was available. The intermediate energy gave a spurious value sub-10 ns lifetime probably as a result of this limitation.

The dependence of the initial Auger lifetimes on pump energy is shown in Figure 40 below. The solid line indicated the trend scaled to the inverse square of the input energy.

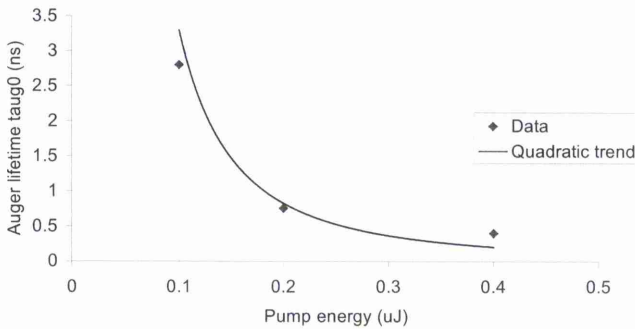


Figure 7-15: Initial Auger lifetime dependence on pump energy

Conventional Auger theory suggests the lifetime should scale as E^{-4} , since $\Delta N \propto I^2$ for two-photon absorption. However the observed trend is consistent with the open aperture z-scans at high intensity conditions, $> 500 \text{ MWcm}^{-2}$, detailed in Chapter 5. In the thick sample regime an effective $I^{1/2}$ scaling was observed indicative of beam spreading. With this effect the number of generated carriers would increase only linearly with the input intensity. The Auger lifetime would then scale as E^{-2} as observed.

Deduction of carrier densities associated with these lifetimes required either assumption of the Auger coefficient and adjustment of the free carrier absorption coefficient or vice-versa. With the published mean of $\gamma=6 \times 10^{-27} \text{ cm}^6 \text{ s}^{-1}$, the deduced carrier density for the measured Auger lifetime of 0.4 ns at the maximum input was $6 \times 10^{17} \text{ cm}^{-3}$. The observed transmission minimum of 70% implied a free carrier absorption coefficient of $6 \times 10^{-18} \text{ cm}^2$. This was smaller than some published values but in good agreement with Dixon [41]. Reported pulse length dependence of free carrier absorption indicates small coefficients may be observed in the early stages arising from intra-band relaxation [45].

7.5 Summary of chapter

In this chapter the temporal evolution of excess carriers generated by two-photon absorption has been considered. Various carrier relaxation and recombination processes have been described. Published reports of carrier lifetimes in InAs and related structures were reviewed.

Carrier lifetimes in bulk InAs were measured using a two-photon pump-probe technique. The observed nonlinear transmission was attributed to both free carrier absorption and refraction. The absorption was isolated and evidence of hot-phonon, screened carrier cooled relaxation was observed. The carrier density rate equation in the presence of Auger and Shockley-Read-Hall recombination was solved and applied to the experimental results. The deduced lifetime values were consistent with previous theoretical and experimentally observed values. However some uncertainty in carrier densities was present because the free-carrier absorption coefficient could not be reliably determined.

7.6 References

- 1 A Othonos, "Probing ultrafast carrier and phonon dynamics in semiconductors," J Appl Phys (Appl Phys Rev) **83**, 1789 (1998).

- 2 T Elsaesser, R Bauerle, and W Kaiser, "Picosecond infrared spectroscopy of molecules and semiconductors," *Infrared Phys* **29**, 503 (1999).
- 3 TF Boggess, JT Olesberg, C Yu, ME Flatte, and WH Lau, "Room-temperature electron spin relaxation in bulk InAs," *Appl Phys Lett* **77**, 1333 (2000).
- 4 P Murzyn, C.R. Pidgeon, and PJ Phillips, "Suppression of Dyakonov-Perel spin relaxation in InAs and InSb by n-type doping at 300K," *Appl Phys Lett* **83**, 5220 (2003).
- 5 M Woerner and T Elsaesser, "Ultrafast thermalization of nonequilibrium holes in p-type tetrahedral semiconductors," *Phys Rev B* **51**, 17490 (1995).
- 6 A Elci, M Scully, AL Smirl, and JC Matter, "Ultrafast transient response of solid-state plasmas. I Germanium, theory and experiment," *Phys Rev B* **16**, 191 (1977).
- 7 HM van Driel, "Influence of hot phonons on energy relaxation of high carrier densities in germanium," *Phys Rev B* **19**, 5928 (1979).
- 8 M Pugnet, J Collet, and A Cornet, "Cooling of hot electron-hole plasmas in the presence of screened electron-phonon interactions," *Solid State Comm* **38**, 531 (1981).
- 9 E Yoffa, "Screening of hot-carrier relaxation in highly photoexcited semiconductors," *Phys Rev B* **23**, 1909 (1981).
- 10 H Lobentanzer, W Stolz, J Nagle, and K Ploog, "Cooling of hot carriers in three- and two-dimensional Ga_{0.47}In_{0.53}As," *Phys Rev B* **39**, 5234 (1989).
- 11 M Takeshima, "Auger recombination in InAs, GaSb, InP and GaAs," *J Appl Phys* **43**, 4114 (1972).
- 12 JS Blakemore, in *Semiconductor Statistics* (Pergamon Press, Oxford, 1962).
- 13 RA Smith, in *Semiconductors* (University Press, Cambridge, 1988).
- 14 Beattie and Landsberg, "Auger effect in semiconductors," *Proc Phys Soc A* **249**, 16 (1959).
- 15 A Sugimura, "Band-to-band Auger effect in GaSb and InAs lasers," *J Appl Phys* **51**, 4405 (1980).
- 16 M Takeshima, "Role of dielectric screening in Auger recombination in semiconductors," *Phys Rev B* **26**, 3192 (1982).
- 17 A Rogalski and Z Orman, "Band-to-band recombination in InAs_{1-x}Sb_x," *Infrared Phys* **25**, 551 (1985).
- 18 KL Vodopyanov, H Graener, CC Phillips, and TJ Tate, "Picosecond carrier dynamics and studies of Auger recombination processes in indium arsenide at room temperature," *Phys Rev B* **46**, 13194 (1992).
- 19 JR Lindle, JR Meyer, CA Hoffman, FJ Bartoli, GW Turner, and HK Choi, "Auger lifetime in InAs, InAsSb, and InAsSb-InAlAsSb quantum wells," *Appl Phys Lett* **67**, 3153 (1995).
- 20 J Meyer, CL Felix, WW Bewley, I Vurgaftman, EH Aifer, LJ Olafson, JR Lindle, CA Hoffman, MJ Yang, BR Bennett, and BV Shanabrook, "Auger coefficients in type-II InAs/Ga_{1-x}In_xSb quantum wells," *Appl Phys Lett* **73**, 2857 (1998).
- 21 S Marchetti, M Martinelli, and R Simili, "The Auger recombination coefficient in InAs and GaSb derived from the infrared dynamical plasma reflectivity," *J Phys: Cond Mat* **14**, 3653 (2002).
- 22 PM Fauchet, "The Auger rate in highly excited Indium Antimonide," *Phys Status Solidi (B)* **110**, K11 (1982).
- 23 BN Murdin, C.R. Pidgeon, DA Jaroszynski, CC Phillips, RA Stradling, CM Ciesla, R Praseres, and CJGM Langerak, presented at the 7th Int Conf on Narrow Gap Semicond, Santa Fe, 1995 (unpublished).

- 24 ME Flatte, CH Grein, Hasenberg. TC, SA Anson, DJ Jang, JT Olesberg, and TF Boggess, "Carrier recombination rates in narrow-gap InAs/Ga_{1-x}In_xSb-based superlattices," *Phys Rev B* **59**, 5745 (1999).
- 25 W Shockley and WT Read, "Statistics of the recombinations of holes and electrons," *Phys Rev* **87**, 835 (1952).
- 26 RN Hall, "Electron-hole recombination in Germanium," *Phys Rev* **87**, 387 (1952).
- 27 KL Vodopyanov, "Extrinsic recombination processes in proton radiated InAs/GaAs heterostructures grown by molecular beam epitaxy," *J Appl Phys* **73**, 627 (1993).
- 28 S Krishnamurthy and MA Berding, "Full-band-structure calculation of Shockley-Read-Hall recombination rates in InAs," *J Appl Phys* **90**, 848 (2001).
- 29 S Guha, JL Blackshire, and A Zakel, "Measurement of charge carrier decay rates in bulk indium arsenide and mercury cadmium telluride wafers," *Proceedings of SPIE* **4288**, 362 (2001).
- 30 CC Phillips, YB Li, RA Stradling, and KL Vodopyanov, "Picosecond saturable absorption measurements on thin film single-crystal InAs layers grown by MBE," *J Phys D* **24**, 437 (1991).
- 31 T Matsuesue and H Sakaki, "Radiative recombination coefficient of free carriers in GaAs-AlGaAs quantum wells and its dependence on temperature," *Appl Phys Lett* **50**, 1429 (1987).
- 32 MI Iglitsin and EV Soloveva, "Recombination of nonequilibrium charge carriers in InAs single crystals," *Sov Phys Solid State* **7**, 2770 (1966).
- 33 AW Blaut-Blachev, LA Balagurov, VV Kartaev, and EM Omelyanovskii, "Recombination of carriers in n-type InAs at 77K," *Sov Phys Semicond* **9**, 515 (1975).
- 34 AI Andrushko, KhM Salikhov, and SV Slobodchikov, "Mechanisms of recombination in indium arsenide crystals," *Sov Phys Semicond* **20**, 255 (1986).
- 35 W van Roosbroeck and W Shockley, "Photon-radiative recombination of electrons and holes in germanium," *Phys Rev* **94**, 1558 (1954).
- 36 CM Ciesla, BN Murdin, CR Pidgeon, RA Stradling, CC Phillips, M Livingstone, I Galbraith, DA Jaroszynski, JGM Langerak C, PJP Tang, and MJ Pullin, "Suppression of auger recombination in arsenic-rich InAs_{1-x}Sb_x strained layer superlattices," *J Appl Phys* **80**, 2994 (1996).
- 37 JW Shelton and JA Armstrong, "Measurement of the relaxation time of the Eastman 9740 bleachable dye," *IEEE J Quant Elec* **302**, 696 (1967).
- 38 EP Ippen and CV Shank, in *Ultrashort light pulses*, edited by S Shapiro (Springer-Verlag, New York, 1977), p. 83.
- 39 D.C. Hutchings and E.W. Van Stryland, "Nondegenerate two-photon absorption in zinc blende semiconductors," *J Opt Soc Am B* **9**, 2065 (1992).
- 40 R DeSalvo, M. Sheik-Bahae, A.A. Said, D.J. Hagan, and E.W. Van Stryland, "Z-scan measurements of the anisotropy of nonlinear refraction and absorption in crystals," *Opt Lett* **18** (3), 194 (1993).
- 41 JR Dixon and JM Ellis, "Optical Properties of n-Type Indium Arsenide in the Fundamental Absorption Edge Region (e)," *Phys Rev* **123**, 1560 (1961).
- 42 KW Berryman and CW Rella, "Nonlinear absorption in indium arsenide," *Phys Rev B* **55** (11), 7148 (1997).
- 43 F. Matossi and F. Stern, "Temperature Dependence of Optical Absorption in p-Type Indium Arsenide," *Phys Rev* **111**, 472 (1958).
- 44 P Mukherjee, M. Sheik-Bahae, and H.S. Kwok, "New method of measuring relaxation times in semiconductors," *Appl Phys Lett* **46**, 770 (1985).

- 45 P Mukherjee, M. Sheik-Bahae, and H.S. Kwok, in *Energy beam-solid interactions and transient thermal processing - MRS Symposia*, edited by DK Biegelson, GA Rozgonyi, and CV Shank (Materials Research Society, Boston, 1985), Vol. 35, p. 97.
- 46 CV Shank and DH Auston, "Parametric coupling in an optically excited plasma in Ge," *Phys Rev Lett* **34**, 479 (1975).

Chapter 8 - Conclusions

8.1 Summary of thesis

In this thesis the nonlinear optical properties of InAs have been studied using a novel ultrashort femtosecond pulse duration infrared laser source. The motivation for the work was to understand the fluence-limiting action arising from two-photon absorption and refraction. The aims of the work were to determine the key parameters associated with the process, namely:

- two-photon absorption coefficient β
- free carrier absorption cross-section σ_a
- nonlinear refractive cross-section σ_r
- carrier recombination lifetime τ

A variety of experiments and theoretical analyses were applied to two-photon absorption, the accompanying nonlinear refraction and subsequent relaxation and recombination of the photo-generated carriers.

The infrared pulses were produced by a regeneratively amplified Ti:Sapphire laser pumping an optical parametric amplifier (OPA) followed by a difference frequency mixing (DFM) crystal. The system had numerous advantages over alternative sources of ultrafast infrared radiation previously used for studying nonlinear processes in narrow band-gap semiconductors.

Proper determination of optical parameters required thorough characterisation of the OPA-DFM system. Output was observed over a wavelength tuning range from 4 to 7 μm with good stability and a Gaussian spatial distribution. The wavelength spectra showed broad Gaussian distributions consistent with dispersion of femtosecond duration pulses. Sub-200

fs pulse lengths were measured with a two-photon detector based autocorrelator. The time-bandwidth product, $\Delta\tau\Delta\nu$, was around twice the transform limit indicating chirp was present and increasing at longer wavelengths.

The wavelength dependence of the two-photon absorption coefficient was measured and compared with several forms of perturbation theory. Sufficient intensity was present in the OPA beam to observe significant nonlinear optical transmission with no need for focusing. This eliminated one of the main uncertainties in calculating the intensity of the beam. The ultra-short duration pulses gave high intensities but with low integrated pulse energy. This effectively minimised any potential free carrier absorption.

Further study of two-photon absorption at high input intensities was achieved through open aperture z-scans. No additional absorption was observed from free carriers. Increased transmission at very high intensities was believed to arise from beam spreading and saturation effects.

Closed aperture z-scans were used to measure refractive contributions at three different wavelengths. A dominant negative, defocusing component was observed that was consistent with the combined free-carrier effects of the plasma contribution, band filling and bandgap renormalisation. A weaker component was also seen that was negative at 4 μm but positive at 5.5 μm . This was in agreement with predictions of an ultrafast, n_2 arising from the real part of the third order susceptibility $\chi^{(3)}$.

A two-photon pump-probe arrangement was used to study the temporal evolution of the photo-generated carriers and their recombination. An induced reduction in transmittance was observed following pump excitation that showed partial recovery over the available 1.5 ns time interval. The signal was attributed to both free carrier refraction and absorption. A resonance spike at zero delay that indicated energy was being coupled out of the probe.

This was thought to arise from the enhancement of the two-photon absorption when the pump and probe overlapped.

Refocusing the probe beam allowed the absorptive contribution to be isolated. From this it was deduced that, although the free carrier refraction was instantaneous, the absorption had a characteristic build up time of ~ 100 ps. This was indicative of the carriers undergoing intra-band relaxation with a long lifetime. The high carrier density and excess effective temperature, calculated to be over 3000 K, caused heating and saturation of the phonon distribution.

The decay of the induced absorption was compared to a model that included both Auger (impact) and Shockley-Read-Hall (defect) recombination mechanisms. The technique was limited in that a free-carrier absorption cross-section was required in order to infer carrier densities. The deduced cross-section was somewhat lower than expected but still in agreement with published data.

8.2 Conclusions

The conclusions drawn from this work are:

- Ultrashort, femtosecond pulses enable two-photon absorption to be measured in isolation from other effects such as free-carrier absorption and recombination. Proper determination of the two-photon coefficient then provides a solid foundation from which other parameters can be selectively introduced and quantified by varying the experimental conditions.
- The magnitude and wavelength scaling of the two-photon absorption coefficient measured in InAs compares well to non-parabolic, second-order perturbation theory for wavelengths from 4 to 5.5 μm . Coefficients measured at longer wavelengths

were smaller than expected which is believed to be due to uncertainty in the pulse duration and the broad, polychromatic output of the OPA.

- The free carrier absorption arising from the photo-generated carriers is markedly different for ultrashort, femtosecond pulses compared to more conventional, pico- or nanosecond pulse durations. This is believed to be due the effects of intra-band relaxation. Single femtosecond pulses experience minimal free carrier absorption, even at very high intensities. The absorption can take up to ~ 100 ps to develop through hot phonon-screened relaxation.
- Nonlinear refraction is still dominated by the free carrier effects, which are negative and defocusing. Refractive cross-sections compare well with theoretical predictions for free-carrier effects. Relatively modest carrier densities ($\sim 10^{17}$ cm⁻³) can create large refractive changes. This limits the maximum beam intensities and hence peak carrier densities achievable in the semiconductor through strong beam spreading within the sample.
- The free carrier lifetime is described well by a combination of Auger and Shockley-Read-Hall recombination mechanisms. The Auger recombination is the dominant process at higher carrier densities but then transitions to a constant SRH lifetime at lower densities.

8.3 Further work

The OPA-DFM is a versatile system capable of producing multiple sources of light tuneable across a wide wavelength range. Similar nonlinear optical measurements could be performed on alternative wide and narrow-gap materials using the DFM or signal and idler outputs from the OPA section. InP, for example, has a band gap of 1.35 eV at room temperature corresponding to 920 nm. In addition the high peak intensities achievable at

long wavelengths provide a good source for the study of multi-photon absorption coefficients. Three-photon absorption was observed in InAs by tuning the system out to $\sim 9 \mu\text{m}$, however the pulse length could not be measured so a coefficient was not determined.

The femtosecond pulses from the OPA were good for providing an initial rapid impulse to generate a free carrier distribution through a thick sample. However probing with a delayed portion of the same beam meant that timescales were limited to a maximum of 1.5 ns because of the travel on a translation stage. Longer timescales would give more accurate data for Shockley-Read-Hall lifetimes and may be better done with a pump-CW probe arrangement. Carbon monoxide ($5.1 \mu\text{m}$) or CO_2 lasers ($9.2 - 10.8 \mu\text{m}$) provide suitable wavelengths for measuring free-carrier absorption. A large detector with high sensitivity is desirable to ensure that only absorptive transients are measured.

A technique for more precise deduction of carrier densities during the pump-probe would be to use a band-gap resonant probe wavelength [1]. Absorption saturation and an increase in probe transmission are observed due to a dynamic Burstein-Moss shift. The Fermi distributions and occupational probabilities of the carrier can be directly inferred from magnitude of the absorption change [2]. An infrared HeNe laser ($3.39 \mu\text{m}$) would be convenient as a probe with adjustment of the InAs band gap achievable through cryogenic cooling. The disadvantage of this technique is that, by definition, the initial absorption of the probe is high so thin samples must be used. Surface and interface recombination effects can become significant in epilayers grown on substrates [3].

A novel semiconductor phenomena introduced in Chapter 7 is the generation of spin gratings and currents. Carriers with a particular spin can be preferentially injected accordingly to the polarisation of the light and selection rules between the bands. It has been shown recently that simultaneous, coherent one- and two-photon absorption can create pure-spin currents through interference according to the carrier momentum [4]. This

has been observed in wide-gap materials however the OPA-DFM could provide a good source for observing this effect in narrow-gap materials where the two-photon absorption is much stronger.

8.4 References

- 1 KL Vodopyanov, H Graener, CC Phillips, and TJ Tate, "Picosecond carrier dynamics and studies of Auger recombination processes in indium arsenide at room temperature," *Phys Rev B* **46**, 13194 (1992).
- 2 PC Findlay, CR Pidgeon, H Pellemans, R Kotitschke, BN Murdin, T Ashley, AD Johnson, AM White, and CT Elliott, "Auger recombination dynamics of $\text{In}_x\text{Ga}_{1-x}\text{Sb}$," *Semiconductor Science and Technology* **14**, 1026 (1999).
- 3 KL Vodopyanov, "Extrinsic recombination processes in proton radiated InAs/GaAs heterostructures grown by molecular beam epitaxy," *J Appl Phys* **73**, 627 (1993).
- 4 JE Sipe, RDR Bhat, A Najmaie, F Nastos, Y Kerachian, HM van Driel, A.L. Smirl, MJ Stevens, and XY Pan, "Optically injected spin currents in semiconductors," International Quantum Electronics Conference (IQEC/CLEO), San Francisco, Session IThK4 (2004).